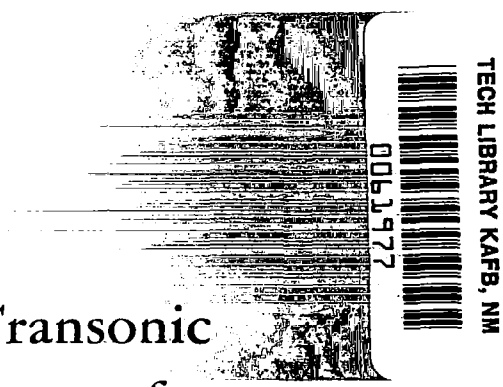

NASA Contractor Report 3446

Finite Element Analysis of Transonic Flows in Cascades - Importance of Computational Grids in Improving Accuracy and Convergence

Akin Ecer and Hasan U. Akay

GRANT NSG-3294
JULY 1981

NASA

NASA Contractor Report 3446

Finite Element Analysis of Transonic Flows in Cascades - Importance of Computational Grids in Improving Accuracy and Convergence

Akin Ecer and Hasan U. Akay
Purdue University at Indianapolis
Indianapolis, Indiana

Prepared for
Lewis Research Center
under Grant NSG-3294

NASA
National Aeronautics
and Space Administration

Scientific and Technical
Information Branch

1981

TABLE OF CONTENTS

FINITE ELEMENT ANALYSIS OF TRANSONIC FLOWS IN CASCADES - IMPORTANCE OF COMPUTATIONAL GRIDS IN IMPROVING ACCURACY AND CONVERGENCE

Akin Ecer* and Hasan U. Akay**
Purdue University at Indianapolis

SUMMARY

The finite element method is applied for the solution of transonic potential flows through a cascade of airfoils. Convergence characteristics of the solution scheme are discussed. Accuracy of the obtained numerical solutions is studied for various flow regions in the transonic flow configuration. The design of an efficient finite element computational grid is discussed in improving accuracy and convergence.

This study shows that the solution of nonlinear equations corresponds to the numerical integration of a pseudo-time system in the solution of steady, inviscid potential equations. The choice of the artificial viscosity parameter, which is necessary for obtaining convergence in the supersonic pocket, and the relaxation parameter, which controls both the convergence characteristics and the accuracy of the obtained solution, are investigated. Proper choice of these parameters as a function of the computational grid is presented. The accuracy of the obtained solutions around the leading and trailing edges of the airfoil, in the subsonic and supersonic flow regions, and around the shock are discussed, and appropriate grid refinement techniques are suggested. An efficient numerical integration scheme for the solution of transonic flow equations is also presented.

The numerical results include several basic test cases to demonstrate the degree of grid refinement required for accuracy and convergence. Also, included in the report are results for complicated flow configurations with choked flow conditions and cascades with high staggers and high solidities.

---

* Professor of Mechanical Engineering
** Research Associate

INTRODUCTION

Analysis of transonic flows through a cascade of airfoils requires accurate modeling of the flow boundaries as well as the details of the subsonic and supersonic flow regions and the shock. The following basic properties must be considered in the analysis of this problem:

- Equations change their characteristics in subsonic and supersonic flow regions which have irregular shapes and may be separated by a discontinuity,
- Leading and trailing edges of the airfoils are sources of near singularities in the flow,
- Cascades usually have irregular geometries.

The efficiency of the computational techniques in treating such irregular geometric configurations is directly related to the applicability of irregular computational grids. When such grids are designed properly, sufficiently accurate approximations of such irregular flow configurations can be obtained.

Numerical solutions of steady, inviscid transonic flow problems have been treated using the finite difference method by several researchers during the last decade (refs. 24,25,28,29). More recent studies have been in the direction of improving the efficiency and accuracy of these solutions (refs. 8,10,16,19,20,21,23,26,31,32). During these investigations, the importance of a computational grid in the calculation of transonic flows was observed. The modification of computational grids has been explored as one of the main tools for improving efficiency and accuracy (refs. 21, 26,31).

Application of the finite element method for the analysis of inviscid transonic flow problems has also been considered by several investigators during the last five years, e.g., (refs. 1-4,6,7,9,12,15,17). The importance of the computational grid in obtaining an accurate solution with finite element method was reported by the present authors in reference 15. One of the main advantages of the finite element method has been its ability to accommodate irregular grids. A less utilized advantage is the capability of adapting the computational grid to the solution either automatically or by interactive means. This property becomes quite important in solving transonic flows in cascades and in choosing the most suitable computational grid for a particular flow problem.

The objectives of the present study are to develop efficient computational techniques for the solution of transonic flows in cascades, and to investigate the important features of computational grids for this problem.

The existing literature on the development of a computational grid for improving accuracy and convergence of numerical solutions has dealt basically with elliptic systems. Accuracy considerations are generally based on refining regions with steep gradients. For improving convergence characteristics of nonlinear elliptic equations, multigrid methods have been developed recently to smooth the residuals with high frequency content in relaxation procedures (ref. 5).

Due to the hyperbolic nature of the equations in the supersonic pocket, the development of an efficient computational grid for analyzing transonic flow through a cascade of airfoils cannot be based only on the above considerations. In the computations it is observed that the convergence problem is far more critical in the supersonic pocket than it is in the surrounding subsonic flow region. Also, convergence and accuracy are generally most critical around the shock.

In this report, the basic considerations in the design of a finite element grid for obtaining accurate and efficient solutions to the transonic flow problem for cascades are presented. Effects of the grid on subsonic and supersonic flow regions and the shock are investigated separately. For an accurate and efficient solution, a computational procedure should be based on consideration of each of these problems and their interaction.

In the following chapter, the finite element analysis of the transonic flow problem for a cascade of airfoils is summarized. In particular, the treatment of periodic boundary conditions and the Kutta condition for sharp trailing edges are discussed. A combined shock fitting and shock capturing scheme is presented. It is also shown that the solution of the set of nonlinear equations for steady transonic flows requires a numerical integration in time of a pseudo-time dependent system of equations. A constant coefficient integration scheme is developed to improve the computational efficiency of this numerical integration scheme.

In the next chapter, convergence characteristics to a steady state are discussed. For the subsonic region, it is shown that the scheme basically requires the solution of an elliptic equation with a relaxation procedure. For the supersonic flow region, the convergence is both a function of the relaxation parameter ω and the artificial viscosity parameter α_e which is introduced by upwinding the element density. It is emphasized that while convergence improves with increasing values of α_e, the accuracy of the solutions is very sensitive to the amount of artificial viscosity. The relationship between the computational grid and the distribution of artificial viscosity is found to be very important and is discussed in detail. This convergence study is also applicable to finite difference and finite volume methods based on the upwinding of local density.

In the next chapter, basic concepts in the development of computational grids for the solution of transonic flow problems are related to the accuracy of the numerical solutions. For obtaining accurate solutions in

subsonic flow regions, grid refinement of regions with high pressure gradients is important. In the supersonic pockets, where pressure gradients are generally small, the accuracy problem is mostly related to the application of an artificial viscosity. Simple yet efficient finite element grids can be employed for the solution of this problem if the artificial viscosity is correctly applied. It is shown that accuracy around the shock is also very sensitive to the application of the artificial viscosity. Finally, the sensitivity of the flow at the trailing edge is discussed for cases where a shock is close to the trailing edge.

The last chapter includes several case studies illustrating the generality of the developed computational scheme and the effect of computational grids in terms of accuracy and convergence. The test cases include a) transonic flow around an isolated cylinder, b) a cascade of NACA 0012 airfoils, with a stagger angle of 45^{o} and gap to chord ratio of 3.6, c) a cascade of NACA 0012 airfoils, with a stagger angle of 45^{o} and gap to chord ratio of 1.0, (choked flow), d) a cascade of 8% circular-arc airfoil, with a stagger angle of 45^{o} and gap to chord ratio of 1.0, and e) a cascade of José Sanz stator blades.

The work presented in this report summarized the applicability of the finite element method for the solution of transonic flow in cascades. The ability to interactively modify the finite element grid in order to improve the accuracy in specific flow regions proves to be one of the main advantages of the method. It is demonstrated in this report that a designer can analyze transonic flows in cascades:

- by starting with a rough finite element grid and refining the critical regions if necessary,
- by controlling the artificial viscosity distribution over the grid and through the iterations,
- by using a combined shock fitting and shock capturing scheme to check the accuracy of the shock region,
- by checking the accuracy of the solution from the comparison of results obtained using different grids.

By using the above procedure, one can always ensure the correctness of the obtained results. It should also be noted that, as the problems get more complex, the need for such a programmed approach becomes more important.

FINITE ELEMENT FORMULATION OF TRANSONIC FLOWS

Governing Equations

We consider the solution of the full potential equation for steady, inviscid and irrotational flows expressed in the conservative form

$$(\rho\phi_{,x})_{,x} + (\rho\phi_{,y})_{,y} = 0 \quad \text{in } \Omega \qquad (1)$$

where ϕ is the velocity potential, Ω is the solution domain, and ρ is the mass density of the fluid. The general boundary conditions of equation (1) are

$$\phi = \phi_o \quad \text{on } S_1 \qquad (2)$$

and

$$\rho\phi_{,n} = f \quad \text{on } S_2 \quad , \qquad (3)$$

where ϕ_o and f are some specified quantities on the boundary $S = S_1 + S_2$, and n is the outward normal on S_2.

By combining the isentropic equation of state with the Bernoulli equation, one obtains the relation

$$\rho = \text{const } (K^2 - q^2)^{\frac{1}{\gamma-1}} \qquad (4)$$

for the mass density, where γ is the ratio of specific heats,

$$K^2 = \frac{2a^2}{\gamma-1} + q^2, \qquad (5)$$

and

$$q^2 = \phi_{,x}^2 + \phi_{,y}^2 \quad . \qquad (6)$$

In the above, K is the maximum attainable speed which is constant throughout the flow, a is the local speed of sound, and q is the local flow speed.

For the cascade geometries shown in figure 1, if the inlet speed of sound a_{in} is normalized then equation (5) becomes

$$K^2 = \frac{2}{\gamma-1} + M_{in}^2 \tag{7}$$

where $M_{in} = q_{in}/a_{in}$ is the inlet Mach number.

Cascade Geometry

Either of the solution domains shown in figure 1 can be used to model two-dimensional cascades. In each case, a set of periodic boundaries together with the blade surfaces, the inlet and exit boundaries, the stagger angle α_s and the pitch h define the cascade geometry. Since the domain in figure 1b is multiply connected, a splitting boundary such as the slit line E-F shown in the figure is required in order to allow the velocity potential to be discontinuous across E-F. This assures that ϕ will be single valued.

The configuration shown in figure 1b is found to be more advantageous for highly staggered cascades, Firstly, it lends itself easily to the generation of less distorted grids, especially at the rounded leading and training edges. Secondly, since the periodic boundaries are furthest from the blade surfaces, the effects of approximations introduced in satisfying the periodicity conditions in this case are minimal.

The boundary conditions for configuration of figure 1a have been discussed in reference 15. Only the case b will be discussed here. Assuming that the farfield inlet and exit flow conditions are uniform and M_{in}, β_{in}, β_{ex} are known, the boundary conditions become

$$\text{i)} \quad f = f_{in} = -\rho_{in} q_{in} \text{Cos}\beta_{in} \quad \text{on A-B} \tag{8}$$

$$\text{ii)} \quad f = f_{ex} = -f_{in} \quad \text{on C-D} \tag{9}$$

$$\text{iii)} \quad f = 0 \text{ on the airfoil surface} \tag{10}$$

$$\text{iv)} \quad \phi^+ - \phi^- = \lambda \quad \text{on E-F} \tag{11}$$

where λ is the circulation which may be determined from the farfield conditions as

$$\lambda = q_{in}(h_x \text{Cos}\beta_{in} + h_y \text{Sin}\beta_{in}) - q_{ex}(h_x \text{Cos}\beta_{ex} + h_y \text{Sin}\beta_{ex}) \tag{12}$$

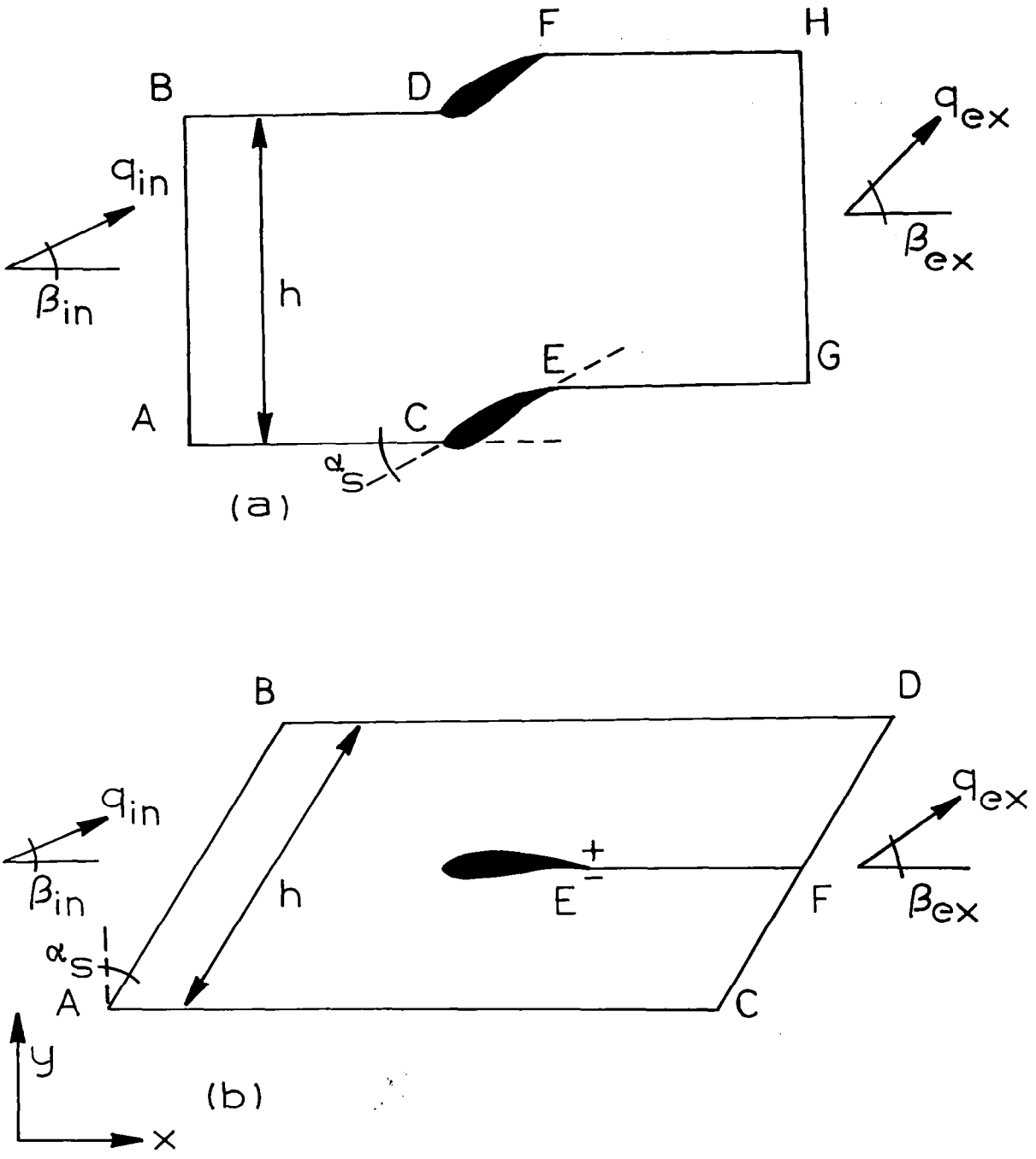

Figure 1. Solution domains for the cascade problem

where

$$h_x = h\mathrm{Sin}\alpha_s \quad , \quad h_y = h\mathrm{Cos}\alpha_s, \tag{13}$$

and q_{ex} is computed iteratively from the continuity equation

$$f_{in} + f_{ex} = 0.$$

The periodicity condition is:

$$\text{v)} \quad \phi(x+h_x, y+h_y)$$

$$= \phi_1(x,y) + q_{in}(h_x \mathrm{Cos}\beta_{in} + h_y \mathrm{Sin}\beta_{in}) \quad \text{on B-D} \tag{15}$$

where $\phi_1(x,y)$ is the unknown distribution of ϕ on A-C. Finally,

$$\text{vi)} \quad \phi = 0 \quad \text{on A} \quad . \tag{16}$$

In the above, equation (9) is due to conservation of mass, (15) is due to perodicity, and (16) is needed to avoid the arbitrariness of the potential function ϕ.

In some cases the exit flow angle β_{ex} is not known a priori; therefore, the circulation λ is also an unknown. To determine λ in this case, the Kutta condition

$$q^2\big|_{E^+} = q^2\big|_{E^-} \tag{17}$$

must be satisfied at the sharp trailing edge of the airfoil. A convenient way of satisfying equation (17) and determining λ in an iterative fashion is discussed on page 18.

Finite Element Formulation

For a finite element formulation of equation (1) - (3) we use the Bateman's variational functional (ref. 13)

$$\pi = \int_\Omega p \, d\Omega + \int_{S_2} f\phi \, dS \tag{18}$$

where for isentropic and perfect gases

$$p = \frac{\gamma-1}{2\gamma} \text{ const } \rho^\gamma \quad . \tag{19}$$

is the pressure.

It can be verified that Ritz type finite elements obtained through the consistent use of Bateman's functional are equivalent to applying a Galerkin formulation to equation (1) (ref. 1).

To introduce the finite element approximations, we express equation (18) for an element e and sum the contributions of all elements in the domain. The stationary values of the resulting expression yield the following variational statement

$$\delta\pi = \sum_e \left[-\int_{\Omega_e} \rho_e \left(\phi_{,x}\delta\phi_{,x} + \phi_{,y}\delta\phi_{,y}\right)d\Omega \right.$$

$$\left. + \int_{S_{2e}} f_e \, \delta\phi ds\right] = 0. \tag{20}$$

We then choose bilinear shape functions $N_i^e(x,y)$ so that within each element the interpolation

$$\phi^e(x,y) = N_i^e(x,y)\phi_i^e = \underline{N}^T\underline{\phi}^e \quad ,(i=1,\ldots,m) \tag{21}$$

holds, where ϕ_i^e are the nodal values of velocity potentials and m is the number of element nodal points. Substituting equation (21) into (20), we obtain the following system of equations

$$\underline{K} \ \underline{\phi} = \underline{f} \tag{22}$$

where

$$\underline{K} = \sum_e \int_{\Omega_e} \rho_e (\underline{N}_{,x}\underline{N}_{,x}^T + \underline{N}_{,y}\underline{N}_{,y}^T)d\Omega \tag{23a}$$

$$\underline{f} = \sum_e \int_{S_{2e}} f_e \underline{N} dS \tag{23b}$$

$$\underline{\phi} = \sum_e \underline{\phi}^e \quad . \tag{23c}$$

Four-node isoparametric quadrilateral elements shown in figure 2 with the bilinear shape functions (ref. 35)

$$N_i^e = \frac{1}{4}\left(1 + \xi\xi_i\right)\left(1 + \eta\eta_i\right) \tag{24}$$

are employed for this investigation, where ξ,η are the natural coordinates and ξ_i,η_i denote the nodal point coordinates of the parent square element in

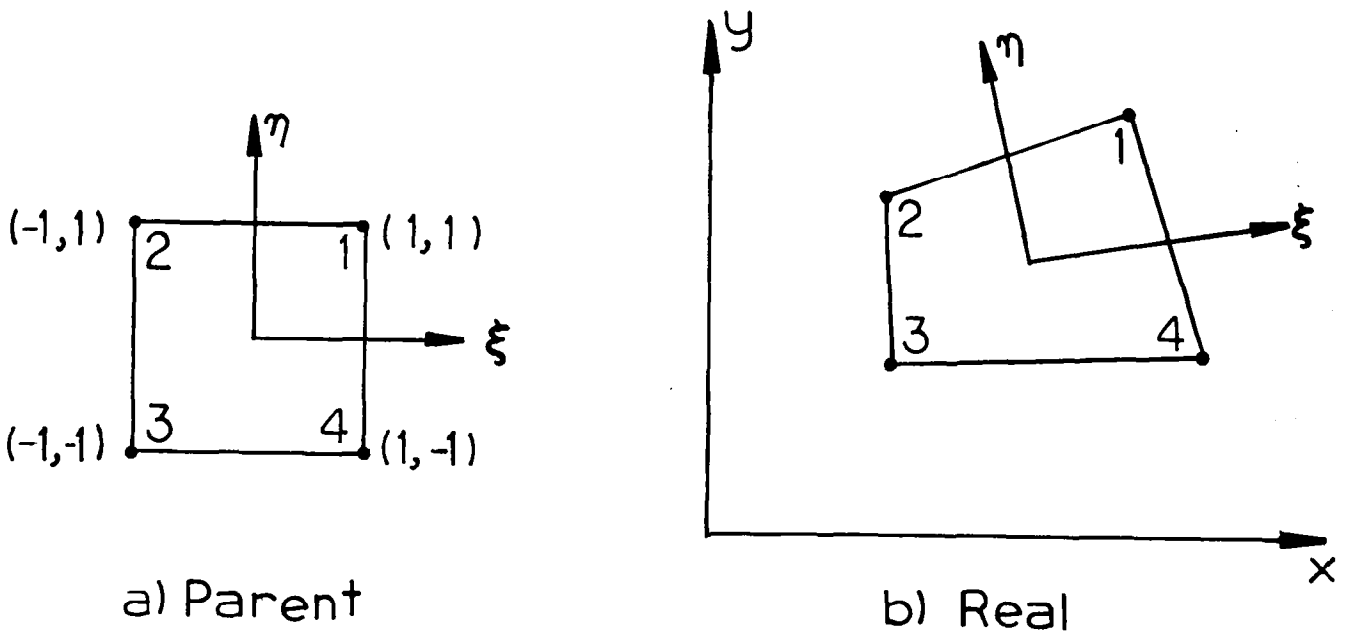

Figure 2. Four-node isoparametric element

figure 2a. With the same shape functions, transformations in the form

$$x^e = N_i^e x_i \ , \ y^e = N_i^e y_i \tag{25}$$

are used in mapping the parent element to a general quadrilateral shown in figure 2b, where x_i and y_i are the global Cartesian coordinates of the nodal points for the transformed element.

A selective Gaussian integration scheme is employed for evaluating the element matrices in equation (23a). The density ρ_e is evaluated only at the centroid of the elements, while a two-point Gaussian quadrature per direction is utilized for the area integration of the shape functions and their global derivatives. Since the local density in an element is nearly constant in the flow direction, no sacrifice in accuracy is made. This leads to significant savings in computations because the area integrations of global derivatives need be performed only once throughout the entire nonlinear iterations.

Pseudo-Unsteady Formulation

To obtain a steady-state solution to the nonlinear equation (1), a pseudo-time formulation is considered in the following form:

$$\frac{\Delta t}{\omega}(\rho\phi_{,xt})_{,x} + \frac{\Delta t}{\omega}(\rho\phi_{,yt})_{,y} + (\rho\phi_{,x})_{,x} + (\rho\phi_{,y})_{,y} = 0 \tag{26}$$

where Δt is the pseudo-time increment and ω is a relaxation factor or a damping coefficient. The weak form of the above equation is:

$$\delta\pi = \int_\Omega [\frac{\Delta t}{\omega}(\rho\phi_{,xt})_{,x} + \frac{\Delta t}{\omega}(\rho\phi_{,yt})_{,y}$$

$$+ (\rho\phi_{,x})_{,x} + (\rho\phi_{,y})_{,y}]\delta\phi(x,y,t)d\Omega = 0 \tag{27}$$

for $0 \leqslant t \leqslant \infty$. Integration of equation (27) by parts yields:

$$\delta\pi = -\int_\Omega \rho(\frac{\Delta t}{\omega}\phi_{,xt}\delta\phi_{,x} + \frac{\Delta t}{\omega}\phi_{,yt}\delta\phi_{,y} + \phi_{,x}\delta\phi_{,x}$$

$$+ \phi_{,y}\delta\phi_{,y})d\Omega + \int_{S_2} f\delta\phi \ ds = 0 \tag{28}$$

where $f = \rho\phi_{,n}$ is the mass flux specified on the boundary S_2.

Finite element discretization of equation (27) yields the following pseudo-unsteady system of nonlinear equations:

$$\Delta t \underline{C}\,\dot{\underline{\phi}} + \underline{K}\,\underline{\phi} = \underline{f} \tag{29}$$

where

$$\underline{C} = \frac{\underline{K}}{\omega} \tag{30}$$

is the damping matrix of the above time dependent problem. Here ω is a relaxation parameter controlling the stability of the numerical integrations. Using backward - differencing in time, the following step-by-step numerical integration scheme for equation (29) is obtained

$$\underline{K}^{n+1}\tilde{\underline{\phi}}^{n+1} = \underline{f}^{n+1} \tag{31}$$

with

$$\underline{\phi}^{n+1} = \omega\tilde{\underline{\phi}}^{n+1} + (1-\omega)\underline{\phi}^{n} \tag{32}$$

where n is the pseudo-time step.

Equation (31) is nonlinear and a "good" estimate of the coefficient matrix is necessary at each time step to assure the stability of the numerical integrations. It has been shown in reference 15 that an appropriate procedure for evaluating $\underline{K}^{n+1}$ and consequently $\underline{C}^{n+1}$ at a time step n is to use

$$\rho_e^{n+1} \approx \rho_e^{n} \tag{33}$$

when the local flow is subsonic, and use

$$\rho_e^{n+1} \approx \rho_e^{n} - \alpha_e \Delta s_e \rho_{e,s}^{n} \tag{34}$$

when it is supersonic. In the above equation s is the streamline direction, Δs_e is the element size in the direction of s, and α_e is known as the coefficient of artificial viscosity.

The extrapolation scheme of equation (33) takes into account the elliptic nature of the equations in the subsonic region whereas equation (34) takes into account the hyperbolic nature of the equations in the

supersonic region. For sufficiently streamlined elements and uniform grids, equation (34) can further be expressed as follows

$$\rho_e^{n+1} \approx \alpha_e \rho_{eu}^n + (1-\alpha_e)\rho_e^n \tag{35}$$

where ρ_{eu}^n is the mass density of the nearest element at the upstream side of e. This corresponds to the well known "upwinding" technique used in finite differences (ref. 19). In the following section, the amount of artificial viscosity α_e and the relaxation factor ω to be used will be determined according to the stability considerations of the numerical integrations.

Obtaining an accurate and efficient solution of the potential flow equations in the transonic regime has been a major concern during the recent years. A popular approach has been to extend the finite difference procedures originally developed for the solution of subsonic flows by adding artificial viscosity in the supersonic region. In reference 19, various types of iterative procedures for solving the same equations are reviewed. ADI, SOR and multi-grid methods as well as higher order relaxation schemes have been applied to improve the convergence properties of transonic flow equations (refs. 8,19,20,21,23,26,31,32). The finite element method, on the other hand, has also been applied to the solution of elliptic problems by many investigators for several years. The extension of this method to transonic flows has been accomplished basically by following the same procedure, i.e., by adding artificial viscosity to the original system of equations (ref. 15).

The Numerical Integration Technique for Pseudo-Time Problem

The numerical integration scheme based on a direct solution of the system defined in equation (31) has been employed with success for the solution of transonic flow problems in reference 15. However, since the left-hand-side of equation (31) is nonlinear, a full decomposition of the coefficient matrix $\underline{K}$ is needed at each step which makes the scheme computationally somewhat inefficient. For efficiency considerations the time integrations in equation (31) are modified as follows:

$$\underline{K}^0 \tilde{\underline{\phi}}^{n+1} = \underline{f}^{n+1} + (\underline{K}^0 - \underline{K}^{n+1})\underline{\phi}^n \tag{36}$$

with

$$\underline{\phi}^{n+1} = \omega\tilde{\underline{\phi}}^{n+1} + (1-\omega)\underline{\phi}^n \tag{37}$$

where

$$\underline{K}^0 = \underline{K}(\rho_\infty) \quad \text{and} \quad \rho_\infty = \rho_{in} \tag{38}$$

are constant for all time steps and $\underline{K}^{n+1}$ is evaluated using ρ^{n+1} as given in equations (33) and (34). Hence, the decomposition of $\underline{K}^0$ is needed only for the first time step and the subsequent solutions can be obtained with relatively inexpensive forward and backward substitutions. We shall refer to the scheme in equation (31) as the variable coefficient scheme (VSC) and the one defined by equation (36) as the constant coefficient scheme (CCS).

Modeling of Shocks

Considerations for convergence and accuracy in the shock region rely strongly on the modeling of the shock. Either shock capturing or shock fitting techniques can be employed to model the shock. Shock capturing techniques have recently become more popular due to the generality of locating the shock and the simplicity of the modeling. However, to attain convergence and stability around the shock, the choice of the computational grid and the artificial viscosity parameter requires considerable effort with either shock capturing or shock fitting methods. The basic considerations in analyzing the stability and the convergence of the numerical scheme in the supersonic flow do not remain valid since the problem involves a shock discontinuity during the transition from supersonic to subsonic flow. To localize the smearing that occurs while modeling the sharp changes at the shock, the computational grid often needs refinement. Moreover, to stabilize the high frequency oscillations in the vicinity of the shock, artificial viscosity is sometimes added even to portions of the subsonic flow immediately following the shock (ref. 26). The main disadvantage of this approach, hence, is the need for judicious modeling in this area. On the other hand, if one attempts to use the shock fitting procedure directly, convergence difficulties are reduced considerably. However, one is faced with the basic problem of locating the shock accurately.

In the present formulation, the potential function ϕ is continuous across the element interfaces but the derived quantities ρ,p and a are discontinuous. Supersonic elements are treated by adding artificial viscosity as discussed previously. While the flow is changing from supersonic to subsonic, the continuity of the mass flux in the form

$$\tilde{\rho}^{+}\phi^{+}_{,n} = \rho^{-}\phi^{-}_{,n} \tag{39}$$

is satisfied as a natural consequence of the variational formulation, where + and - denote the upstream and downstream sides of the interface, and $\tilde{\rho}$ is the modified density defined by equation (34). Hence, providing that the interfaces are sufficiently aligned with the shock lines, the shocks are allowed to appear between the elements, and the continuity of the actual

mass flux

$$\rho^{+}\phi^{+}_{,n} = \rho^{-}\phi^{-}_{,n} \tag{40}$$

is satisfied in the limit, as the artificial viscosity parameter approaches to zero. For finite values of α_e equation (40) can be imposed as an additional constraint to the variational form, as will be discussed on page 17. However, the effect of violating equation (40) is found to be insignificant for small values of α_e.

Since, across the shock, the influence from downstream to upstream is still present, the above is basically a shock capturing scheme. The scheme requires grid refinement at the shock in order to localize the smearing effects due to downstream influence. Moreover, high frequency oscillations appearing in the shock vicinity require relatively more artificial viscosity in this region to damp out such oscillations. The resulting solution at the shock is extremely sensitive to the way these difficulties are handled, consequently, no unique solution is readily available. To remedy this situation, we propose to use a shock fitting technique for checking the uniqueness of the obtained results.

In the shock fitting procedure, the shock is also assumed to occur at the element interfaces. However, after a shock is detected as a change from supersonic to subsonic flow between two adjoining elements, these elements are uncoupled, and appropriate boundary conditions are imposed on both sides of the shock (ref. 15). Although this technique is computationally straight-forward to implement, as in all other shock fitting techniques, it relies strongly on the prior determination of the shock position. For this reason a combined version of shock capturing and shock fitting techniques is employed.

a) Shock Capturing

In the case of shock capturing, no modifications are made in the basic form of finite element equations. Although shocks can still occur as discontinuities between elements, smearing is present due to the coupling between the subsonic and supersonic elements neighboring the shock. An additional constraint equation is introduced along the shock, since the conservation is no longer guaranteed at the shock interface because of upwinding. The variational functional in equation (18) is modified as follows:

$$\pi^{*} = \sum_{e} \pi_e + \lambda \sum_{f} \int_{S_f} (\rho_e^{+}\phi^{+}_{,n} - \rho_e^{-}\phi^{-}_{,n})^2 ds \tag{41}$$

where λ is a penalty constant, S_f is the common edge of the elements on the shock and the symbols (+) and (-) denote each side of the shock. The implementation of this concept is simply achieved by checking the adjacent

elements in subsonic and supersonic flow regions. The element equations are then modified with the inclusion of the line integral in equation (41). Details of such interface elements are given in reference 2.

b) Shock Fitting

In the shock fitting procedure, the shock is again assumed to occur at the element interfaces. However, when a shock is detected as a change from supersonic to subsonic flow between two adjoining elements, these elements are uncoupled as shown in figure 3. This results in a physical separation of subsonic and supersonic regions of flow on the computational grid.

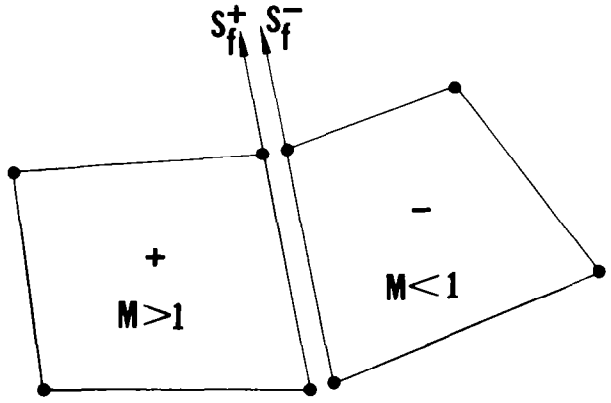

Figure 3. Shock fitting model

A natural boundary condition is imposed on the shock line of the supersonic element in the following form:

$$f_e^{n+1} = f_e^n - \alpha_e \Delta s_e f_{e,s}^n \tag{42}$$

where

$$f_e^n = (\rho_e^+ \phi_{,n}^+)^n \tag{43}$$

The value of ϕ_i at the shock points are in turn placed as forced boundary conditions

$$\phi_i^- = \phi_i^+ \tag{44}$$

at the corresponding nodes of the subsonic element along S_f^-. Conservation is once more satisfied through the use of the penalty function technique, but this time only for the downstream element, by modifying the functional as follows:

$$\pi_e^* = \pi_e + \lambda \int_{S_f} (\rho_e^+ \phi_{,n}^+ - \rho_e^- \phi_{,n}^-)^2 \, ds. \tag{45}$$

In equation (45) no variations are taken with respect to (+) terms since they are assumed to be known from the upstream conditions. No additional node points are created. This requires the modification of the element equations along the shocks. In this way, fundamentally different characteristics of subsonic and supersonic flows are separately modeled.

Since, as it will be shown that the scheme is uniformly convergent in a wider range of initial conditions for higher artificial viscosities, shock capturing solutions are first obtained by selecting a large artificial viscosity parameter α_e. Following this, a series of shock capturing solutions are obtained by gradually decreasing α_e until convergence difficulties are detected. Using the previously converged shock capturing solutions as an initial guess, an attempt at shock fitting is subsequently made to check the shock position. If the initial shock position is correct and the artificial viscosity content is optimum, the influence from downstream to upstream at the shock is minimal in the shock capturing. Hence, both techniques yield essentially the same solution beyond which no further decrease in the artificial viscosity is possible.

If the initial position of shock is incorrect, the shock moves to a different position after fitting, generally towards the downstream direction. The developed fitting scheme differs from the classical fitting procedures for which the position of the shock remains fixed. In the present case, however, when the conditions in equations (42) and (44) are applied on a particular flow configuration, a new shock position is free to develop after each iteration. The computer code automatically detects the new shock position and applies fitting once more. In that case the shock capturing is again tried by lowering the artificial viscosity, and the above process is repeated until a unique solution is obtained.

A novel feature of the present formulation is the ease with which a combined version of both techniques is utilized. At any point

during the iterations, the solution procedure can be switched from one scheme to another to improve efficiency and accuracy without altering the computational grid. It should also be mentioned that the adaptation of the grid to the direction of an oblique shock which has been successfully applied by using shock fitting techniques can also be implemented in the developed procedure.

Computational Grid, Periodic Boundaries and Kutta Condition

A typical computational grid shown in figure 4 is employed here in modeling highly staggered cascades. The broken lines on the grid denote the farfield inlet and exit boundaries of the solution domain shown in figure 1b. The extensions at the inlet and exit boundaries are used to maintain a rectangular outer domain instead of a parellelogram for efficiency and ease in the grid generation. Uniform farfield flow conditions are imposed in these extended regions. The use of rectangle-like elements in the grid has the advantage of providing grid lines which are aligned better with the direction of the flow as well as the direction of the shock lines. Moreover, with this grid severe element distortions can readily be avoided at the rounded leading and trailing edges.

Along the periodic boundaries, every node need not have a matching node on the opposite periodic side. The matching periodic nodes are identified with solid circles in figure 4 for which the periodicity constraint given by equation (15) is imposed. Equation (15) is satisfied by assigning the same equation number to each pair of the periodically located nodes and modifying the right-hand side of the element equations on the boundary line B-D in figure 1b, with the potential difference $q_{in}(h_x \cos\beta_{in} + h_y \sin\beta_{in})$. The nodal values of the intermediate periodic nodes are computed by interpolations from the values of the nearest pair of nodes. The final periodicity is then attained iteratively. This scheme allows a flexibility in placing the periodic nodes, which leads to the generation of more efficient grids with refinements only in the regions of interest.

A symmetric frontal solver (ref. 22) is employed in solving the system of equations. In this solution procedure, only those equations that are currently required for the elimination of a specific nodal point variable need by assembled and saved in the high-speed storage. As opposed to banded solvers, the effectiveness of the scheme does not depend on the nodal point numbering sequence. Hence, the periodic boundary conditions can be imposed conveniently by assigning the same equation numbers to each pair of periodically located nodes. This may be accomplished without renumbering the grid points, and also with no loss of computational efficiency.

If the exit flow conditions are not known a priori, the Kutta condition at the trailing edge is iteratively satisfied through the following procedure. The circulation around the airfoil is determined from a previous

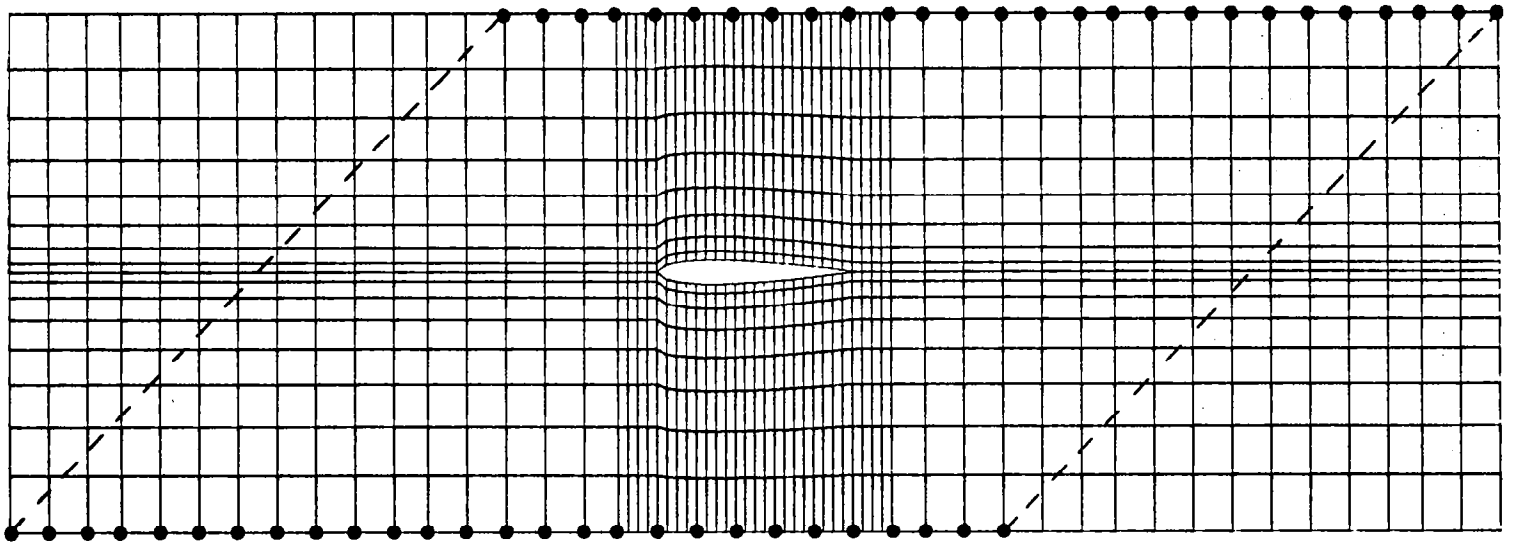

Figure 4. Finite element computational grid

iteration, using the computed velocity potential values of the two uncoupled nodes at the sharp trailing edge, as follows:

$$\lambda = (\phi^{+} - \phi^{-})\big|_{E} \tag{46}$$

where + and - denote the two sides of the slit which extends from the trailing edge to the exit boundary. This value of circulation is then imposed all along the slit as a constant discontinuity in velocity potential for the new iteration. The procedure is repeated until an overall convergence is reached and the Kutta condition

$$q^{2}\big|^{+} = q^{2}\big|^{-} \tag{47}$$

at the trailing edge is satisfied.

CONVERGENCE CHARACTERISTICS OF THE EQUATIONS

Convergence of Variable Coefficient Scheme (VCS)

The computational procedure outlined thus far involves appropriate choice of α_e in equation (34) and ω in equation (37) in obtaining accurate and convergent results. To investigate the convergence characteristics of the equation, to a steady state solution, a simple one-dimensional model will be used, and since the convergence limits obtained from a single element model provides an upper bound to the general system, only one element will be considered. Hence, for an element e and for $\gamma = 2$, equation (31) takes the form

$$\{K^2 - (q_e^n)^2 + \alpha_e \Delta x_e [(q_e^n)^2]_{,x}\} \underline{N}_{,x} \underline{N}^T_{,x} \tilde{\underline{\phi}}_e^{n+1} = 0 \tag{48}$$

If one assumes that the estimate to the nth solution is close to the steady state solution $\underline{\phi}_e$ or q_e in element e so that

$$\tilde{\underline{\phi}}_e^n = \underline{\phi}_e + \Delta\tilde{\underline{\phi}}_e^n \quad , \quad ||\underline{\phi}_e|| >> ||\Delta\tilde{\underline{\phi}}_e^n|| \tag{49}$$

$$\tilde{q}_e^n = q_e + \Delta\tilde{q}_e^n \quad , \quad |q_e| >> |\Delta\tilde{q}_e^n| \tag{50}$$

where $||\ .\ ||$ denotes a suitable vector norm and $|\ .\ |$ denotes an absolute value, then equation (48) becomes

$$[K^2 - q_e^2 + \alpha_e \Delta x_e (q_e^2)_{,x}] \underline{N}_{,x} \underline{N}^T_{,x} \Delta\tilde{\underline{\phi}}_e^{n+1}$$

$$= [2q_e \Delta q_e^n - 2\alpha_e \Delta x_e (q_e \Delta q_e^n)_{,x}] \underline{N}_{,x} \underline{N}^T_{,x} \underline{\phi}_e \ . \tag{51}$$

Recognizing that

$$\underline{N}^T_{,x} \Delta\tilde{\underline{\phi}}_e^{n+1} = \Delta\tilde{q}_e^{n+1} \quad \text{and} \quad \underline{N}^T_{,x} \underline{\phi}_e = q_e \quad , \text{ etc.}, \tag{52}$$

equation (51) can be rewritten as follows:

$$[K^2 - q_e^2 + \alpha_e \Delta x_e (q_e^2)_{,x}] \underline{N}_{,x} \Delta\tilde{q}_e^{n+1}$$

$$= [2q_e^2 - \alpha_e \Delta x_e (q_e^2)_{,x}] \underline{N}_{,x} \Delta q_e^n - 2\alpha_e \Delta x_e q_e^2 \underline{N}_{,x} \Delta q^n_{e,x} \tag{53}$$

By using equation (26) it may further be shown that

$$\frac{\Delta t}{\omega}\ \frac{\Delta q_e^{n+1} - \Delta q_e^{n}}{\Delta t}\ \underline{N}_{,x} = \frac{2q_e^2 - 2a_e^2 - 2\alpha_e \Delta x_e (q_e^2)_{,x}}{2a_e^2 + \alpha_e \Delta x_e (q_e^2)_{,x}}\ \Delta q_e^n \underline{N}_{,x}$$

$$- \frac{2\alpha_e \Delta x_e q_e^2}{2a_e^2 + \alpha_e \Delta x_e (q_e^2)_{,x}}\ \Delta q_{e,x}^n \underline{N}_{,x} \tag{54}$$

where

$$a_e^2 = (K^2 - q_e^2)/2 \ . \tag{55}$$

The above difference relationship implies that the error $\Delta q_e^n(x,t)$ satisfies the following differential equation:

$$\Delta q_{e,t}^n + c\Delta q_{e,x}^n = b\Delta q_e^n \tag{56}$$

where for small amounts of artificial viscosities

$$c = \alpha_e\ \Delta x_e\ M_e^2\ \frac{\omega}{\Delta t}\ , \tag{57}$$

$$b = (M_e^2 - 1)\frac{\omega}{\Delta t}\ , \tag{58}$$

and

$$M_e = q_e/a_e$$

is the local Mach number. This model error equation will be employed to describe the basic characteristics of the pseudo-time integration procedure in the different flow regions.

a) Convergence in Subsonic Flow, c = 0:

In the case of subsonic flows, with no added artificial viscosity, the solution of this problem requires accurate and efficient integration of the reduced system

$$\Delta q_{e,t}^n = b\Delta q_e^n \ , \quad b < 0 \tag{59}$$

When the local flow is subsonic, i.e., when $M < 1$, even with zero artificial viscosity α_e, the scheme converges to a steady state provided that $\omega > 0$. The solution of equation (56) in this case is

$$\Delta q_e^{n+1} = \Delta q_e^n \exp[b\Delta t] \tag{60}$$

which represents the response of a first order damped system. The rate of convergence depends on both the relaxation factor ω and the local Mach number. In addition, to assure the stability of the numerical integration procedure in time, the bounds for ω become

$$0 < \omega < 2/(1 - M_e^2) \tag{61}$$

Equation (61) shows that for compressible flows, the over-relaxation can be higher as a function of local compressibility compared to incompressible flows. Multi-grid methods or the use of over-relaxation schemes mainly aim at increasing the convergence of the iterations for small values of b, which is typical of elliptic systems.

b) Convergence in Supersonic Flow, $c \neq 0$:

When the local flow is supersonic and no artificial viscosity is used (i.e., $\alpha_e = 0$) the solution of equation (56) becomes divergent as implied by equation (60). However, when a positive artificial viscosity is introduced, the characteristics of the system change and it becomes a hyperbolic system. The solution of equation (56) for $\alpha_e > 0$ can be written as

$$\Delta q_e^{n+1} = \Delta q_e^n \, (x - c\Delta t) \exp\,[b\Delta t] \tag{62}$$

This solution indicates that since the errors in this case cannot be damped, they are convected in the flow direction with a wave speed c which is linearly proportional to the amount of added artificial viscosity α_e and the relaxation factor ω. While propogating however, the errors are magnified since $b > 0$. The rate of magnification depends on the values α_e and ω as defined in equation (58).

By changing the behavior of the equations into a convective form with the addition of artificial viscosity, convergence to a steady state is guaranteed in equation (62) for a fixed point in the supersonic pocket. At a particular time step during the iterations, typical variation of errors in the supersonic pocket is as shown in figure 5. Errors at any time step have increasing magnitudes in the flow direction and are largest around the shock. As the flow reaches a steady state at the subsonic upstream, Δq_e, at the subsonic point converges to zero. The convergence at an element depends on the variation of Δq_e at the supersonic element until all the

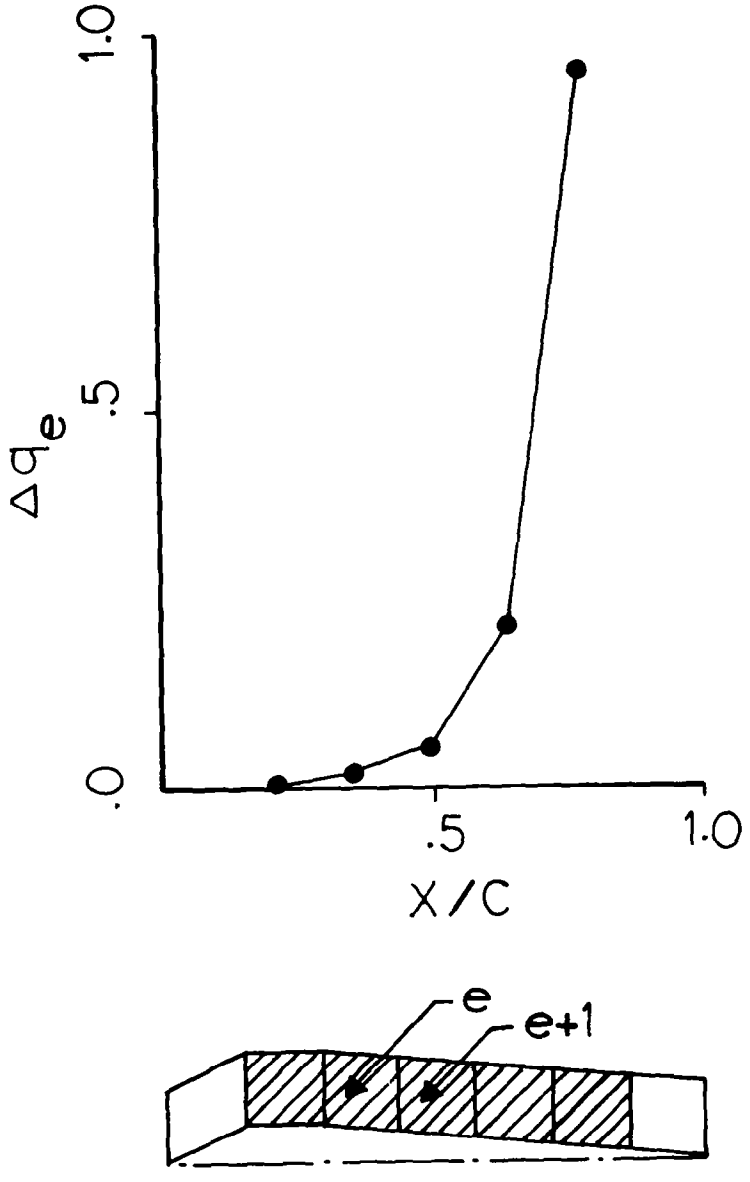

Figure 5. Instantaneous distribution of errors in the supersonic pocket

errors are convected through. It will be shown subsequently that this will depend on how far downstream the element is located and on the number of elements placed in the supersonic pocket up to that point.

The above analysis of the convection of the errors in the supersonic pocket is general for an "artificial compressibility" scheme, whether it is based on a finite difference, finite volume or a finite element method. The present study provides a rigorous analysis of the problem. The solution scheme for transonic flows should be suited to account for the propogation of the error in the flow direction. In the application of the present scheme, it was observed that the convection of the errors is the determining factor in the convergence rate of the solutions. To illustrate this, a sample case is tested for a cascade problem (NACA 0012 airfoils, with 0^{o} stagger angle, $h/C = 3.6$, $\beta_{in} = 0$, $M_{in} = 0.8$). The variation of errors for each time step are plotted in figure 6 for all of the supersonic elements on the airfoil surface, following the numerical integration scheme in equation (31) for different values of α_e and ω. In these figures m_e denotes the element location at the supersonic pocket; $m_e = 1$ being the first supersonic element past the sonic line. As can be seen, when the flow is subsonic for an element, solutions exhibit uniform convergence described by equation (60). As soon as the element becomes supersonic, an artificial viscosity is added and the errors are convected with a wave speed linearly proportional to the artificial viscosity from equation (57). Also from the same equation, the change in the relaxation parameter, ω, increases both the damping factor, which is negative in this case, and the wave speed. Therefore, the errors are magnified as they are convected along the flow direction until they reach the shock. The convergence of the solution is complete when all errors generated by the upstream elements have been convected. This makes the shock region critical for convergence and determines the stability characteristics of the scheme.

Convergence of Constant Coefficient Scheme (CCS)

Following the same procedure presented in this chapter, we consider a one-dimensional version of equation (36). For a single element e and $\gamma = 2$, equation (36) takes the form

$$\{K^2 - q_\infty^2\}\, \underline{N}_{,x} \underline{N}_{,x}^{T} \tilde{\phi}_e^{n+1} =$$

$$\{q_\infty^2 + (q_e^n)^2 - \alpha_e \Delta x_e [(q_e^n)^2]_{,x}\}\, \underline{N}_{,x} \underline{N}_{,x}^{T} \phi_e^n = 0. \qquad (63)$$

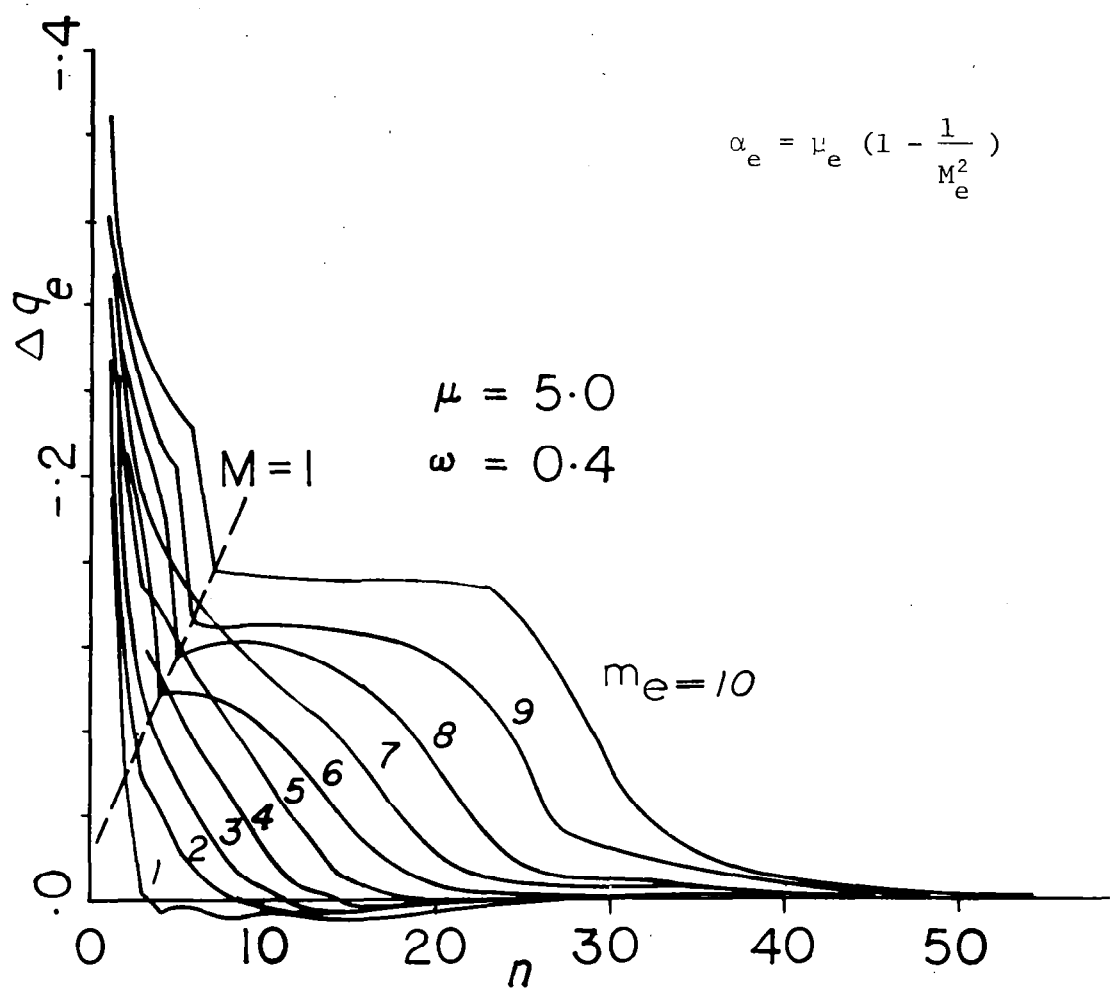

Figure 6. Convergence to the steady state in the supersonic pocket

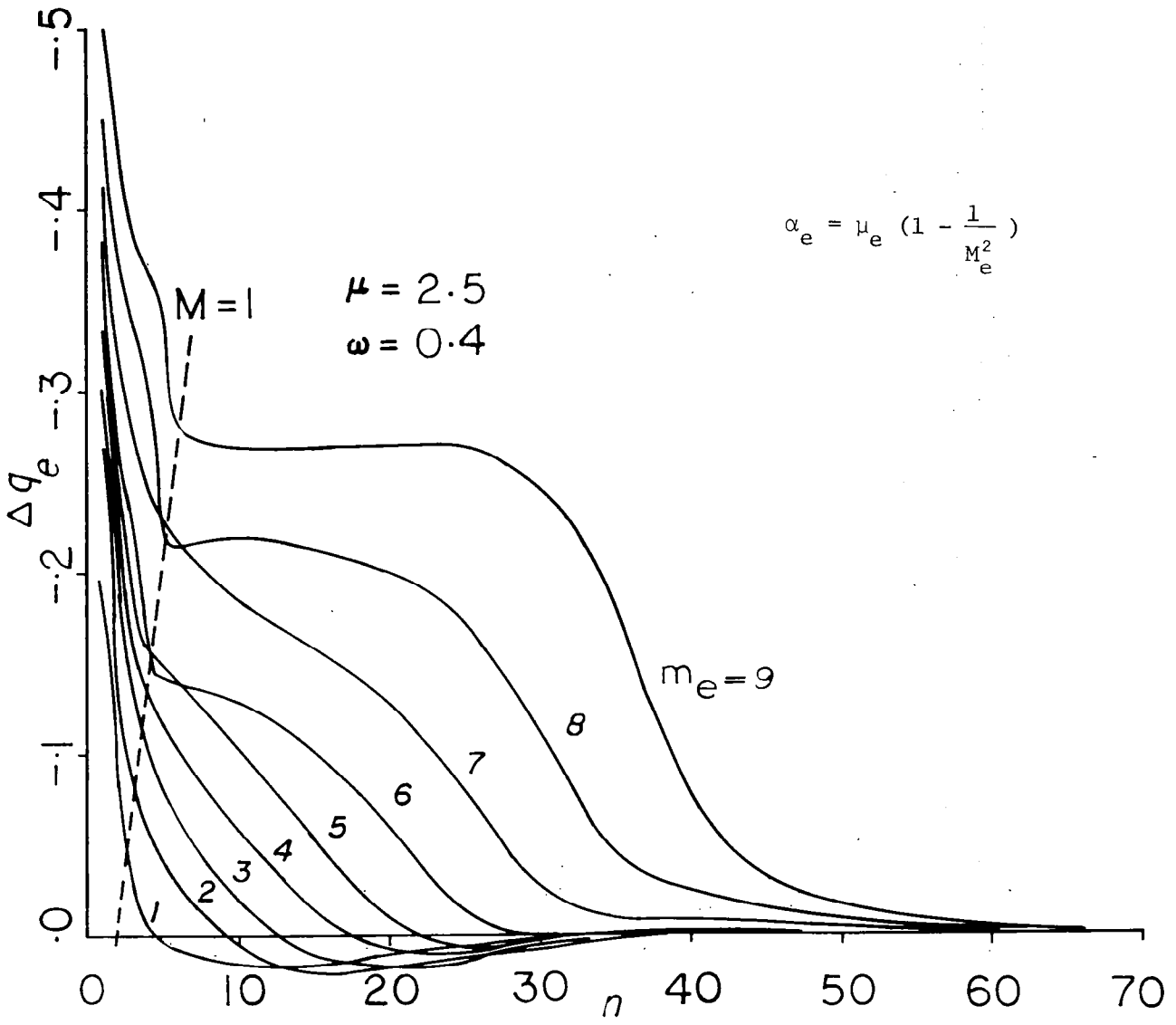

Figure 6. Convergence to the steady state in the supersonic pocket (Continued)

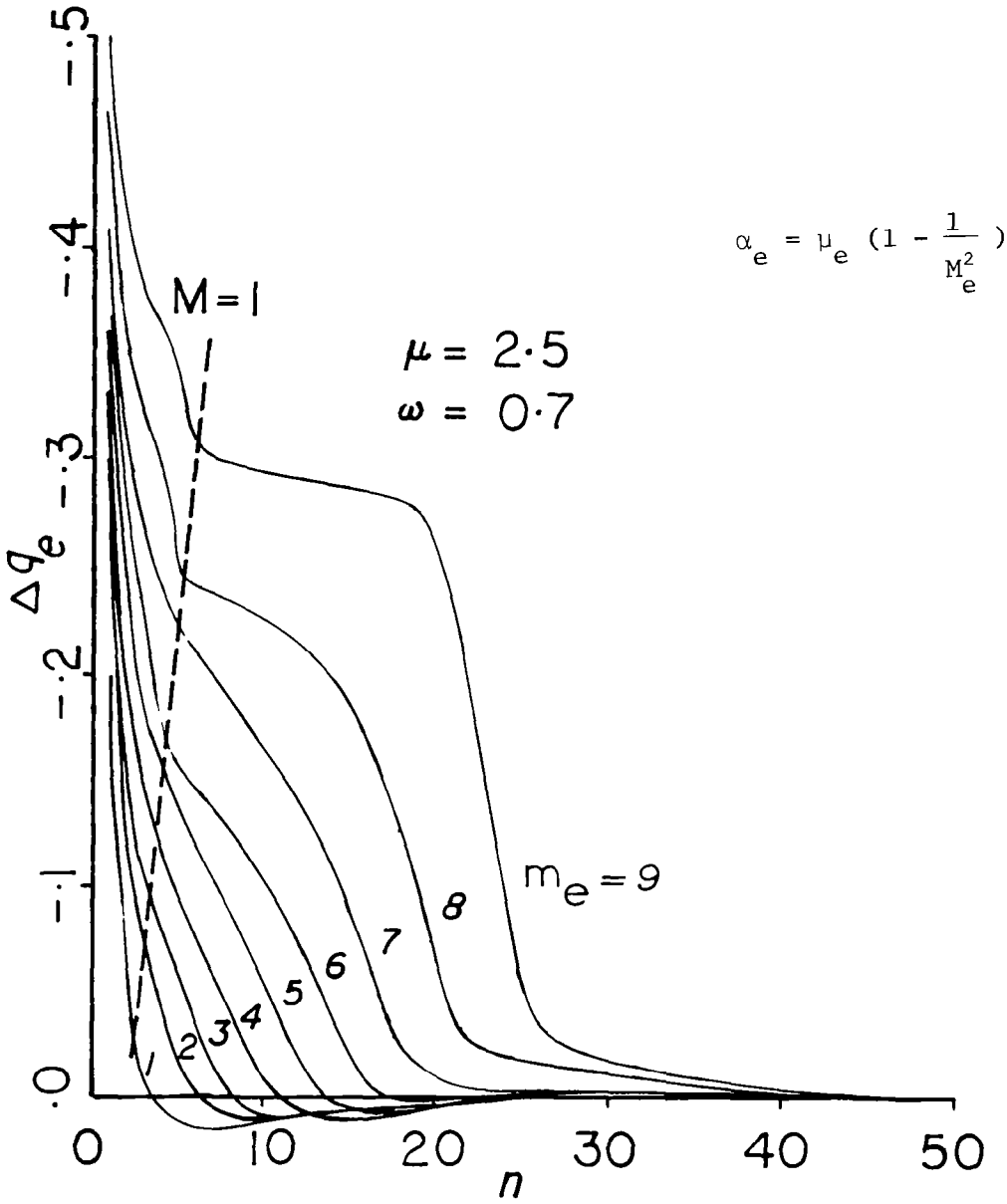

Figure 6. Convergence to the steady state in the supersonic pocket (Continued)

If the estimate to the nth solution is close to the steady state solution $\underline{\phi}_e$ in element e, i.e., if

$$\underline{\tilde{\phi}}_e^n = \underline{\phi}_e + \Delta\underline{\tilde{\phi}}_e^n \quad \text{with} \quad ||\underline{\phi}_e|| >> ||\Delta\underline{\tilde{\phi}}_e^n|| \tag{64}$$

and

$$\tilde{q}_e^n = q_e + \Delta\tilde{q}_e^n \quad \text{with} \quad |q_e| >> |\Delta\tilde{q}_n^e| \quad , \tag{65}$$

then equation (63) becomes

$$\begin{aligned}
&[K^2 - q_\infty^2]\underline{N}_{,x}\underline{N}_{,x}^T\Delta\underline{\tilde{\phi}}_e^{n+1} \\
&= [-2q_\infty^2 + q_e^2 - \alpha_e\Delta x_e(q_e^2)_{,x}]\underline{N}_{,x}\underline{N}_{,x}^T\Delta\underline{\phi}_e^n \\
&+ [2q_e\Delta q_e^n - 2q_\infty\Delta q_\infty^n - 2\alpha_e\Delta x_e q_e\Delta q_e^n]\underline{N}_{,x}\underline{N}_{,x}^T\underline{\phi}_e \quad .
\end{aligned} \tag{66}$$

Recognizing that

$$\underline{N}_{,x}^T\Delta\underline{\tilde{\phi}}_e^{n+1} = \Delta\tilde{q}_e^{n+1} \quad \text{and} \quad \underline{N}_{,x}^T\underline{\phi}_e = q_e \quad , \text{ etc.,} \tag{67}$$

equation (66) is simplified as follows

$$\begin{aligned}
&[K^2 - q_\infty^2]\underline{N}_{,x}\Delta\tilde{q}_e^{n+1} = \\
&= [-2q_\infty^2 + 3q_e^2 - 2\alpha_e\Delta x_e(q_e^2)_{,x}]\underline{N}_{,x}\Delta q_e^n - 2\alpha_e\Delta x_e q_e^2\underline{N}_{,x}\Delta q_{e,x}^n \quad .
\end{aligned} \tag{68}$$

Using equation (37) and the identities:

$$2a_e^2 = K^2 - q_e^2 \quad ; \quad 2a_\infty^2 = K^2 - q_\infty^2 \tag{69}$$

we obtain

$$\begin{aligned}
&\frac{\Delta t}{\omega}\, a_\infty^2\, \frac{\Delta q_e^{n+1} - \Delta q_e^n}{\Delta t}\, \underline{N}_{,x} \\
&= [q_e^2 - a_e^2 - \alpha_e\Delta x_e(q_e^2)_{,x}]\Delta q_e^n\underline{N}_{,x} - \alpha_e\Delta x_e q_e^2\Delta q_{e,x}^n\underline{N}_{,x} \quad .
\end{aligned} \tag{70}$$

The above difference relationship implies that the error again satisfies the following differential equation

$$\Delta q^n_{e,t} + c\Delta q^n_{e,x} = b\Delta q^n_e \quad , \tag{71}$$

where for small amounts of artificial viscosities

$$c = \alpha_e \Delta x_e \, M_e^2 \, \frac{a_e^2}{a_{\infty}^2} \, \frac{\omega}{\Delta t} \quad , \tag{72}$$

$$b = \frac{a_e^2}{a_{\infty}^2} \, (M_e^2 - 1) \, \frac{\omega}{\Delta t} \quad . \tag{73}$$

Comparison of the above stability analysis with the results obtained for VCS in equations (56-58) shows that in this case the coefficients b and c are both magnified with a factor of a_e^2 / a_{∞}^2. It will be shown in the following section that the choice of artificial viscosity, α_e from equations (57,58) or from (72,73) provides the same bounds for convergence. It can be concluded that both CCS and VCS exhibit similar convergence characteristics, but CCS is computationally more efficient.

Choice of the Artificial Viscosity Distribution

One of the most important factors in determining the efficiency of the solution procedure has been the choice of the artificial viscosity distribution. The finite difference schemes have traditionally employed a fixed artificial viscosity distribution for a particular grid. For each grid point, this distribution is determined only as a function of the local Mach number. Thus, while for rough grids the convergence is fast, for finer grids it slows down due to the reduction in the artificial viscosity.

The basic steps of the finite element scheme developed here are as follows: i) choose a relatively high artificial viscosity, ii) obtain convergence to a steady-state, iii) reduce the artificial viscosity, iv) repeat the same steps until a solution with sufficiently small artificial viscosity is obtained. This procedure has proven to be very reliable; one can always converge to a stable solution which is also checked for accuracy by the shock fitting technique. It is similar to the application of successive mesh refinement techniques where one is increasing the number of mesh points for reducing the artificial viscosity.

For a better understanding of the choice of the artificial viscosity distribution, equation (56) is further studied. The solution of this equation can be written in the following form:

$$\Delta q_e^n = \Delta q_e^o \, (x-ct) \, \exp(bt) \tag{74}$$

If an initial solution, Δq_e^o, is assumed in the form of a ramp function,

$$\Delta q_e^o = 0 \qquad \text{for } x < 0 \quad \text{and} \quad x > L$$

$$\Delta q_e^o = q_{\max} \, x/L \qquad 0 \leqslant x \leqslant L \tag{75}$$

where L is the length of the supersonic pocket, the condition for uniform convergence, $\Delta q^n_{e,t} < 0$, provides

$$c \geqslant \frac{bx}{1-bt} \quad . \tag{76}$$

The condition for uniform convergence requires the following lower limit for the artificial viscosity:

$$\alpha_e \geqslant \frac{m_e}{1-\omega n\left(1 - \frac{1}{M_e^2}\right)} \left(1 - \frac{1}{M_e^2}\right) , \tag{77}$$

where M_e is the element number indicating its position in the flow direction starting from the shock, and n is the number of time step ($t = n\Delta t$). As can be seen in this formulation, the most undesirable case occurs at initial time step (n = 0) for the element neighboring the shock, $m_e = N$, where the length of the supersonic pocket is $L = N\Delta x$. For both CCS and VCS schemes, if only the initial time step is considered, then, equation (77) reduces to,

$$\alpha_e \geqslant m_e \left(1 - \frac{1}{M_e^2}\right) \quad . \tag{78}$$

In references 15 and 4, a limit for the artificial viscosity was defined as,

$$\alpha_e \geqslant \frac{1}{1-r_e} \left(1 - \frac{1}{M_e^2}\right) \tag{79}$$

where r_e is the ratio of error for two neighboring elements, i.e.,

$$r_e = \frac{\Delta q_{e-1}}{\Delta q_e} < 1 \quad . \tag{80}$$

It can be shown that, for the case of a ramp function as an initial solution, equation (79) reduces to equation (78). Also, if the propagation of the errors to the neighboring elements is neglected, for $m_e = 1$, equation (78) becomes,

$$\alpha_e \geq 1 - 1/M_e^2 \tag{81}$$

which is the commonly employed expression.

The above solution of the model equation indicates several important considerations in the selection of an artificial viscosity distribution:

- Use of higher values of α_e is necessary at the initial stages of the numerical integration procedure. However, lower values of artificial viscosity are permissible at later stages as can be seen from equation (77).

- Equation (77) also suggests that the amount of artificial viscosity should also be determined on the basis of the position of an element in the supersonic pocket.

- As can be seen from equation (79), the amount of artificial viscosity necessary for uniform convergence depends on the local Mach number as discussed by several investigators, e.g. (refs. 19,21,25).

- In addition, however, the required artificial viscosity depends highly on the distribution of the errors in the initial solution which is implied by r_e in equation (79). For larger values of artificial viscosity, the scheme is uniformly convergent for a wider range of initial conditions.

- Also, as can be seen from equation (80), when a grid is refined and the element size gets smaller, r_e approaches unity and the value of artificial viscosity necessary for uniform convergence increases.

Customarily, the non-dimensional artificial viscosity coefficient α_e as defined in equation (81) is employed in the literature as the measure of the amount of artificial viscosity. However, for a comparison of accuracy of solutions obtained with different computational grids, one should use equal values of

$$\alpha_e^* = \alpha_e \, \Delta s_e \tag{82}$$

rather than α_e for both grids as a measure of the total artificial viscosity employed in equation (34) where Δs_e is the size of the element

employed in equation (34). If one compares solutions obtained from different grids by using same values of α_e, the results will be different not only due to the discretization errors but, also, due to the different quantities of artificial viscosity α_e^*. In fact, the latter becomes the main source of error in the supersonic region. For the same reason, in the case of non-uniform grids a correction is needed on α_e to maintain a uniform artificial viscosity distribution. This correction is achieved simply by using a modified artificial viscosity coefficient as follows:

$$\alpha_e' = \alpha_e \frac{\Delta s_{av}}{\overline{\Delta s}_e} \tag{83}$$

where Δs_{av} is an average element size in the supersonic pocket, and $\overline{\Delta s}_e$ is the average of the lengths of elements e and eu; eu indicating the element number at the upstream of element e. Consequently the total artificial viscosity used in each element becomes

$$\alpha_e^* = \alpha_e' \Delta s_e = \alpha_e \frac{\Delta s_{av} \Delta s_e}{\overline{\Delta s}_e} \tag{84}$$

Thus a uniform distribution of α_e^* rather than α_e is obtained for the irregular grid.

a) Von Neumann Analysis of Convergence:

For a better understanding of the convergence characteristics of the equations in the supersonic region a Von Neumann type stability analysis of the error-equation (56) is performed after expressing a difference equation in time as follows:

$$\Delta q_e^{n+1} = (1 + b\Delta t - \frac{c\Delta t}{\Delta x_e}) \Delta q_e^n + \frac{c\Delta t}{\Delta x_e} \Delta q_{eu}^n \tag{85}$$

Assuming that a supersonic region of length L is divided into equally spaced elements of size $\Delta x_e = L/N$, the Fourier components of the error at a mesh point k and a time step n can be written in the form:

$$\Delta q_e^n = V^n \exp(Ie\Theta_k) \tag{86}$$

where

$$I = \sqrt{-1} \quad , \quad \theta_k = \pi k \frac{\Delta x_e}{L} \quad , \quad k = 1,2...., N+1,$$

$$\min\theta_k = \frac{\pi \Delta x_e}{L} = \frac{\pi}{N} \quad , \quad \max\theta_k = \pi \tag{87}$$

Substitution of equation (86) into equation (85) yields the following amplification factor for the magnitude of error:

$$\frac{V^{n+1}}{V^n} = 1 + b\Delta t - \frac{c\Delta t}{\Delta x_e} + \frac{c\Delta t}{\Delta x_e}(\mathrm{Cos}\theta_k - I\mathrm{Sin}\theta_k). \tag{88}$$

The polar diagram of the amplification factor is shown in figure 7.

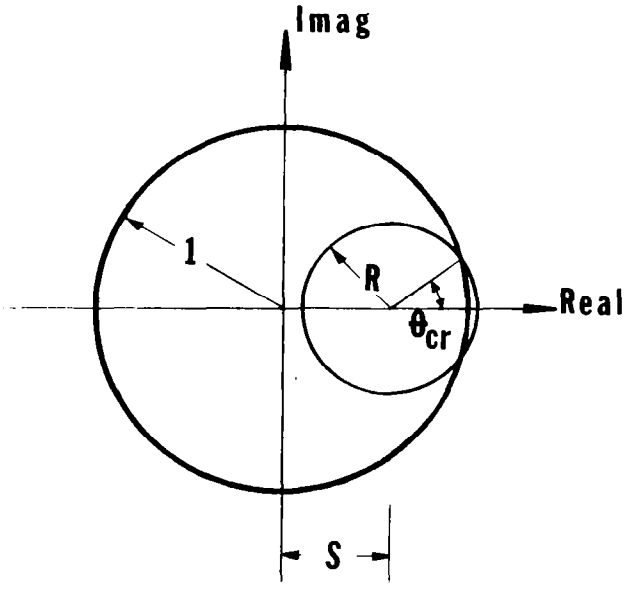

Figure 7. Polar diagram

The two necessary conditions for uniform convergence as observed from figure 7 are:

$$1) \quad R = \frac{c\Delta t}{\Delta x_e} < 1 \quad \text{or} \quad \alpha_e \omega < \frac{1}{M_e^2} \tag{89}$$

$$2) \quad S = 1 + b\Delta t - \frac{c\Delta t}{\Delta x_e} < 1 \quad \text{or,} \quad \alpha_e > 1 - \frac{1}{M_e^2} \tag{90}$$

Equation (90) provides a restriction on the relaxation parameter. At high artificial viscosities, as the propogation speed of errors are high, the relaxation parameter must be decreased for retaining stability of the numerical integrations. Since in subsonic flows

$$R + S = 1 + b\Delta t < 1 \tag{91}$$

the scheme is always convergent. For supersonic flows, however, the inequality in equation (91) is not satisfied. Therefore, the scheme is not uniformly convergent unless

$$\theta_{min} = \frac{\pi}{N} > \theta_{cr} \tag{92}$$

$$\alpha_e > \frac{N_e^2}{\pi^2} \left(\frac{M_e^4 - 1}{M_e^2} \right) \frac{1}{1 + \omega(M_e^2 - 1) - \omega\alpha_e M_e^2} \quad . \tag{93}$$

The above equation indicates that the convergence at a particular supersonic point depends on the number of elements, N_e, counted from an upstream point at which an error starts propogating. As the upstream points converge to a steady state, N_e for a particular point decreases requiring less artificial viscosity. At a certain time during the iterations the convergence characteristics change along the downstream direction based on the upstream conditions.

This analysis demonstrates again the importance of accounting for the convective nature of the errors in the design of both the solution procedures and the computational grids.

ACCURACY OF THE SOLUTIONS

Introduction

The accuracy of the transonic flow solutions depends on the correct modeling of the several flow regions with different properties. In the analysis of flow through a cascade, basic regions of interest are the supersonic pockets, the shock lines, and the leading and trailing edges of the airfoils. The application of shock capturing techniques, with added artificial viscosity for obtaining stable solutions, at the same time complicates the accuracy problem. One can introduce "wiggles" or "excessive smearing" to the solution through the artificial viscosity added to the system. It becomes quite difficult to analyze the accuracy of the obtained solution as a function of the number of node points if the amount of artificial viscosity changes with the grid refinement. The accuracy problems can be categorized in the following three main groups:

(a) Discretization errors due to high gradients in pressure distribution. These errors are important generally around the leading and trailing edges of the airfoils where the flow is subsonic and the equations are elliptic.

(b) Errors due to the artificial viscosity distribution. Since the converged solution at the supersonic pocket is obtained by a specified artificial viscosity distribution, the difference from the inviscid flow can be considered as an error. The minimization of this type of error requires proper application of the artificial viscosity distribution as a function of local flow and the computational grid.

(c) Errors in modeling shock discontinuities across which the flow equations change their characteristics.

Computational Grid for Subsonic Flow Regions

In the case of subsonic flows, equation (1) is elliptic and the finite element formulation involves the calculation of the local maxima of the variational functional in equation (18). The convergence to a steady state is guaranteed from the integration of equation (26) as shown in equation (60). The rate of convergence on the other hand can be improved by using relaxation as implied by equations (60) and (61) where relaxation factor ω is determined as a function of the local Mach number. In terms of designing an appropriate grid for subsonic flows, one has to be mainly concerned with the accuracy and the faster convergence of iterations. It has been shown during recent years that the computational grids can be important in improving the convergence of the relaxation techniques expecially, for elliptic equations (ref. 5).

From the mathematical standpoint, the finite element discretization of equation (1) requires the calculation of the pressure integral over each element area individually. The discretization errors for the entire flow becomes the sum of the discretization errors in each element. For a given number of elements, the grid has to be designed to minimize the total discretization error. It sould be noted that, because of the elliptic nature of the equations in the subsonic region, local discretization errors, due to boundary geometry generally remain local and can be improved by a gradual refinement of the mesh in the immediate problem region. The accuracy problem related to choosing computational grids has also been studied by finite element researchers for several elliptic problems, e.g., (refs. 33 and 34).

In designing a computational grid for subsonic flows, one has to refine the grid at regions of high pressure gradients, such as leading and trailing edges of an airfoil, until the results reach a desired accuracy level. Local modifications of the grid have generally localized effects on the flow configuration. When the grid is refined, the convergence follows the characteristics of the model error-equation in equation (59).

To illustrate some of the points discussed, incompressible flow for a Gostelow airfoil cascade was analyzed. The simple sheared grid shown in figure 8 was used. The results shown in figure 9 are representative of the problems encountered in the solution of subsonic flows in cascades. At the leading edge of the airfoil a near singularity occurs. In this area of high pressure gradients local discretization errors dominate the solution. This is attributed to the high distortion of elements around the leading edge as shown in figure 10a. Figure 10b illustrates the simple adjustments made on the initial grid to improve the situation. As can be seen from figure 9, the improvements made by the change in the grid remain local.

Designing Grids for Transonic Flows

The design of computational grid in transonic flows requires several considerations. The accurate representation of the subsonic leading edge becomes more important in predicting the supersonic pocket as the sonic line develops closer to the leading edge. The accuracy of the solution is most critical at this region. As discussed previously for subsonic flows, an appropriately refined grid is necessary for the modeling of high pressure gradients. Similarly, accurate modeling of the trailing edge becomes important since it affects the accuracy of the exit flow conditions.

The source of difficulties for modeling the supersonic pocket in a cascade is quite different. As it will be shown with numerical examples, the problem is more that of convergence than of accuracy. The classical concept of refining a grid for better accuracy has to be very carefully applied in this case. The choice of artificial viscosity and relaxation parameter as well as the modeling of the shock are also strongly dependent

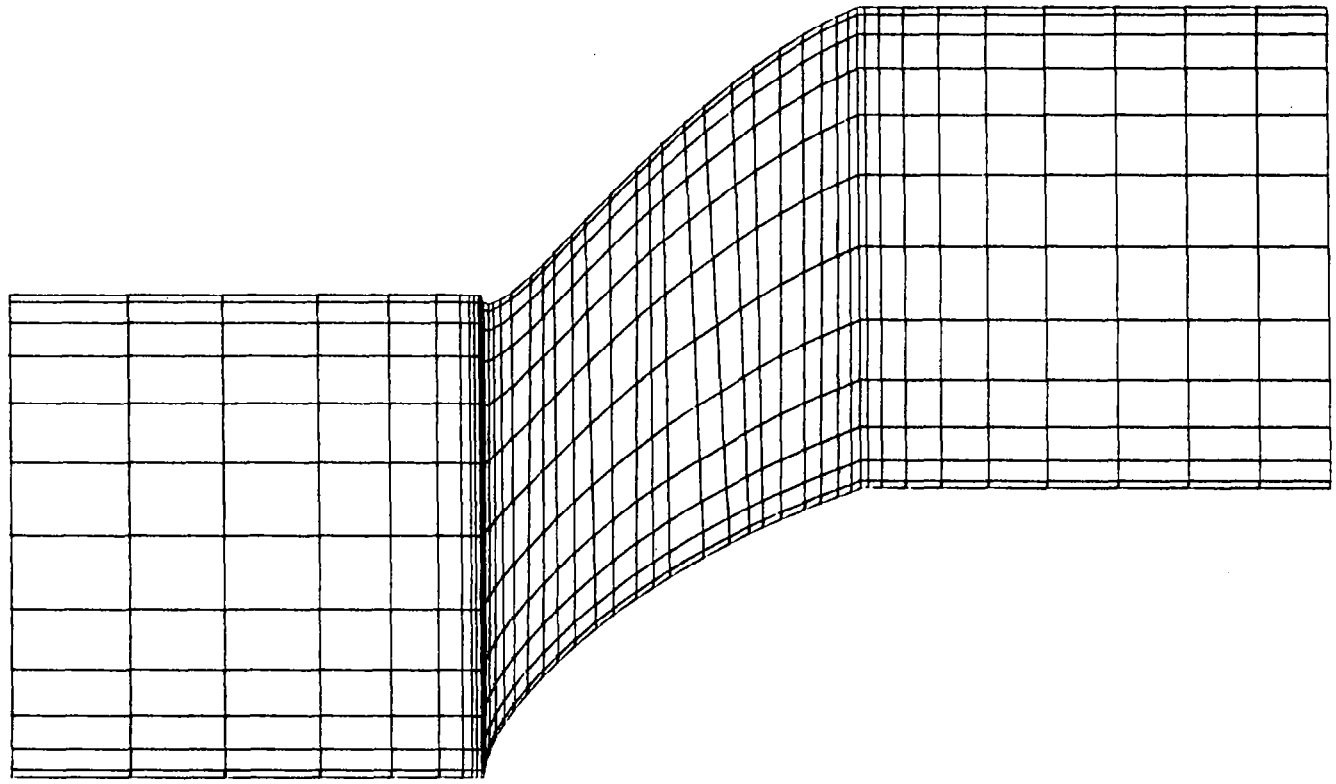

Figure 8. Computational grid for Gostelow airfoil

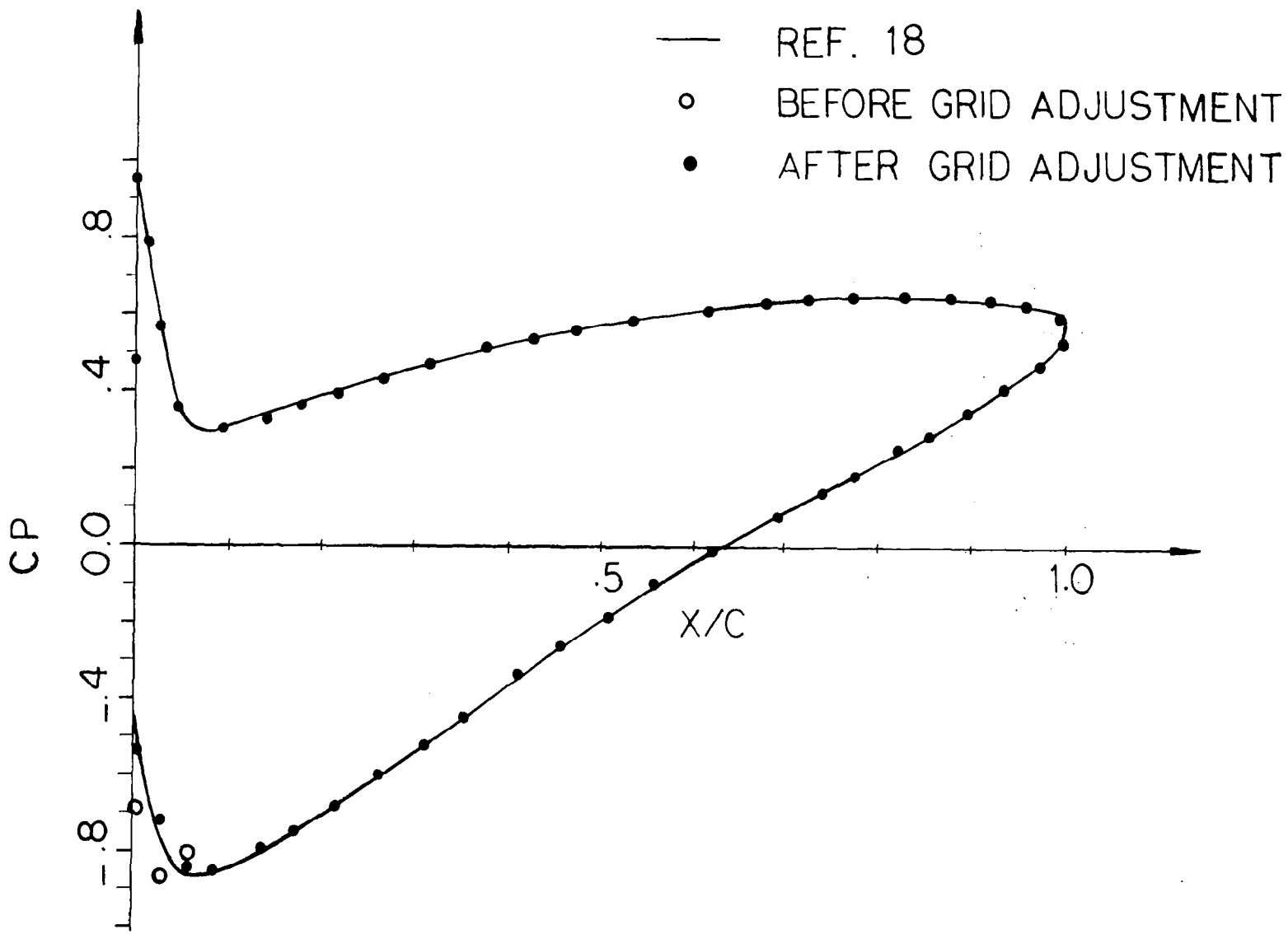

Figure 9. Comparison of results - Gostelow Airfoil

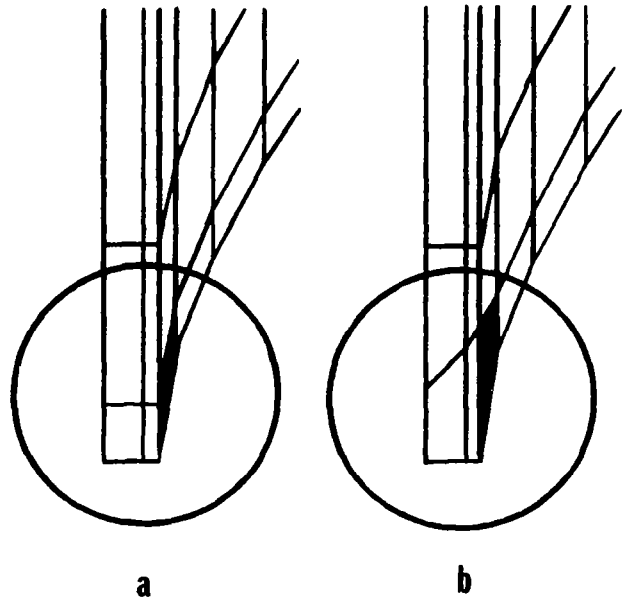

Figure 10. Grid adjustment at the leading edge

on the computational grid. When one refines a computational grid for accuracy, the efficiency of the solution requires a new set of these parameters.

To illustrate some important aspects in analyzing the transonic flows, a cascade of NACA 0012 airfoils with a pitch to chord ratio of 3.6, and the flow conditions $M_{in} = 0.80$, $\beta_{in} = 0.0^{o}$, $\beta_{ex} = 0.0^{o}$, and $\alpha_{s} = 0.0^{o}$ was considered. Four different grids shown in figure 11 were used for this nonlifting case, where, due to symmetry in the cascade geometry only one half of each grid is drawn. There are 10 elements over the airfoil in the coarse grid A, 20 elements in the intermediate grid B, and 28 elements in the fine grids C and D. Grid A and B have 12 elements between each airfoil, whereas, grids C and D have 28 elements. There are a total of 312 elements in grid A, 480 elements in grid B, and 1152 elements in grids C and D.

Figure 12 shows the variation of pressure coefficients C_{p} over the chord length C for the coarse grid A. A series of solutions presented were obtained by employing different amounts of artificial viscosity for this grid. Artificial viscosity was added only to the supersonic elements as given in equation (34). In order to account for the effect of propogation of errors to the neighboring elements, a nondimensional constant μ_{e} is employed throughout the supersonic region so that the artificial viscosity in equation (79) is calculated as

$$\alpha_{e} = \mu_{e} \left(1 - \frac{1}{M_{e}^{2}}\right) \quad . \tag{94}$$

Furthermore, for comparing the results obtained from different grids the artificial viscosity multiplier μ_{e} is scaled such that

$$\mu_{e}^{*} = \mu_{e} \frac{\Delta s_{e}}{\Delta s_{A}} \tag{95}$$

is used in measuring the artificial viscosity content for each case, where Δs_{A} is the average mesh size in the supersonic pocket of grid A.

A series of solutions were sequentially obtained by using the shock capturing technique for $\mu_{e}^{*} = 3.0$, 2.0, 1.5 and 1.0. The shock developed between the same elements in all cases although its position was not correct. An overshooting for low values of the artificial viscosity also indicates this inaccuracy in the shock location. A shock fitting was then applied to the solution at $\mu_{e}^{*} = 1.0$ and subsequently a solution at $\mu_{e}^{*} = 0.8$ was obtained. In figure 12 only the results of $\mu_{e}^{*} = 0.8$ solution is presented since they

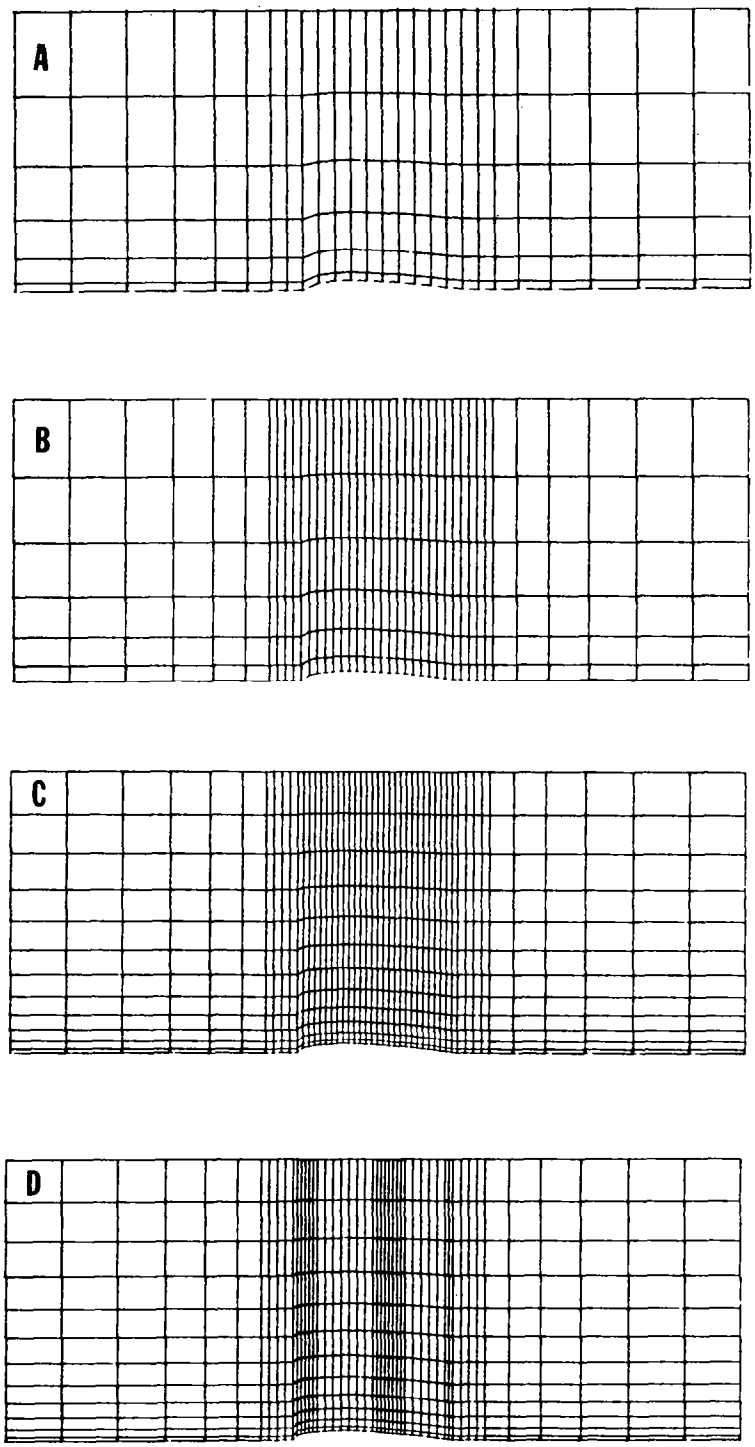

Figure 11. Computational grids for NACA 0012

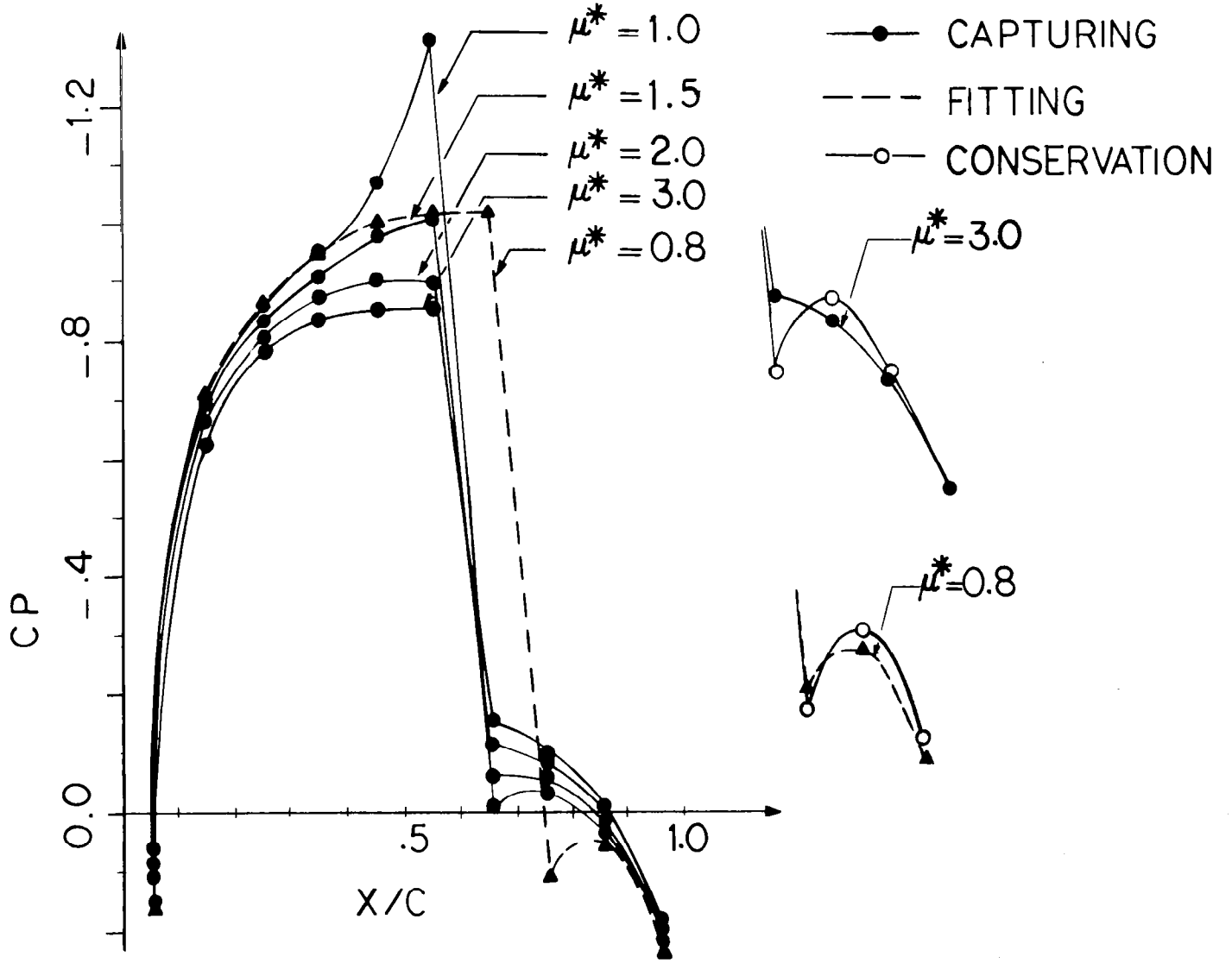

Figure 12. Comparison of results of Grid A (Coarse grid) - Capturing and Fitting

are close. The position of the shock moved downstream after the shock fitting by one element and the overshooting disappeared. When the fitting scheme was switched back to capturing, the solution did not change.

The observed behavior in these solutions verifies the convergence characteristics of the equations as discussed previously in this report. During the integration of equation (29) it was observed that the convergence was obtained in the flow direction in a sweeping manner. The importance of the path of convergence is evident in these results since the location of the shock is determined initially for a high artificial viscosity distribution. For small artificial viscosities, as in the case of $\mu_e^* = 1.0$, several solutions can be obtained depending of the shock location. The overshoot at the shock region can be explained from the inspection of equations (79-80). As r_e converges to unity, the amount of artificial viscosity required is considerable magnified. In the case of shock fitting, the uncoupling of the flow regions and the introduction of the boundary conditions in equations (42-44) eliminates the overshoot and moves the shock in the downstream direction.

Also shown in figure 12 is the effect of satisfying the mass conservation across the element interfaces at the shock as defined in equations (41) and (45). It is observed that for high values of artificial viscosity, introduction of a constraint for mass conservation modifies the singularity at the shock tail considerably. However, as the artificial viscosity converges to zero, the effect is negligible as it is also evident from equations (42) and (45).

Figure 13 shows a different set of results obtained again for grid A. After a shock capturing solution followed by a shock fitting at $\mu_e^* = 3.0$, solutions were successively obtained with different values of artificial viscosity by employing shock fitting only. Although solutions with very small values of artificial viscosity were obtained rather efficiently, the position of the shock did not change.

Solutions with finer grids B and C exhibited similar behavior in terms of convergence and will not be repeated any further. Final solutions obtained from different grids are summarized in figure 14 and compared with the finite area solution of Dulikravich and Caughey (ref. 10). It is to be noted that the finite element results presented in figure 14 are for approximately equivalent values of μ_e^* in each grid. In comparing different grids, μ_e^* rather than μ_e should be used as a measure of the artificial viscosity.

As it is observed from results in figure 14, the accuracy for the flow at the supersonic pocket is extremely high even for rough grids, although the modeling of the shock and its location needs special attention. On the

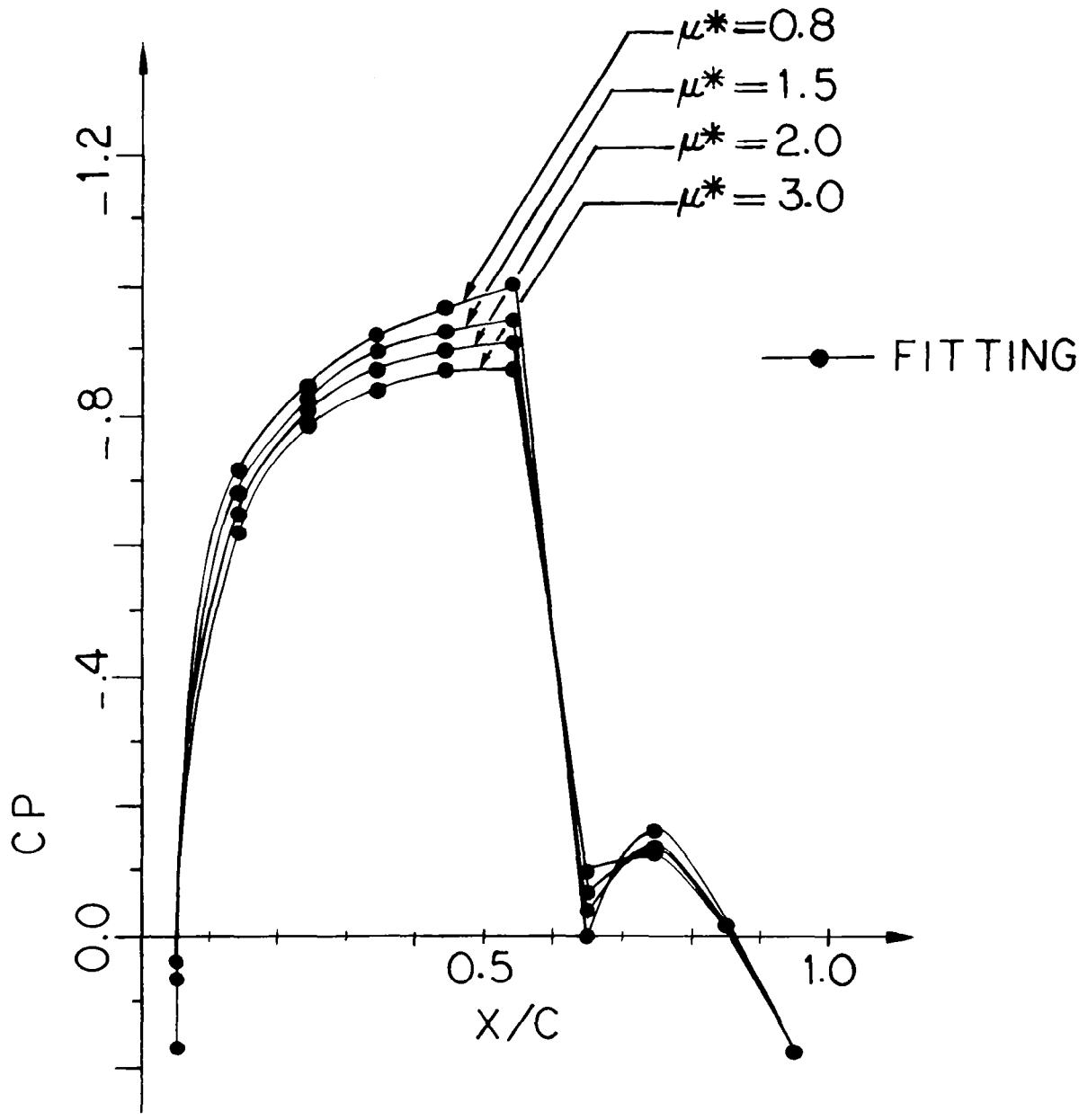

Figure 13. Comparison of results for Grid A (Coarse grid) - Fitting only

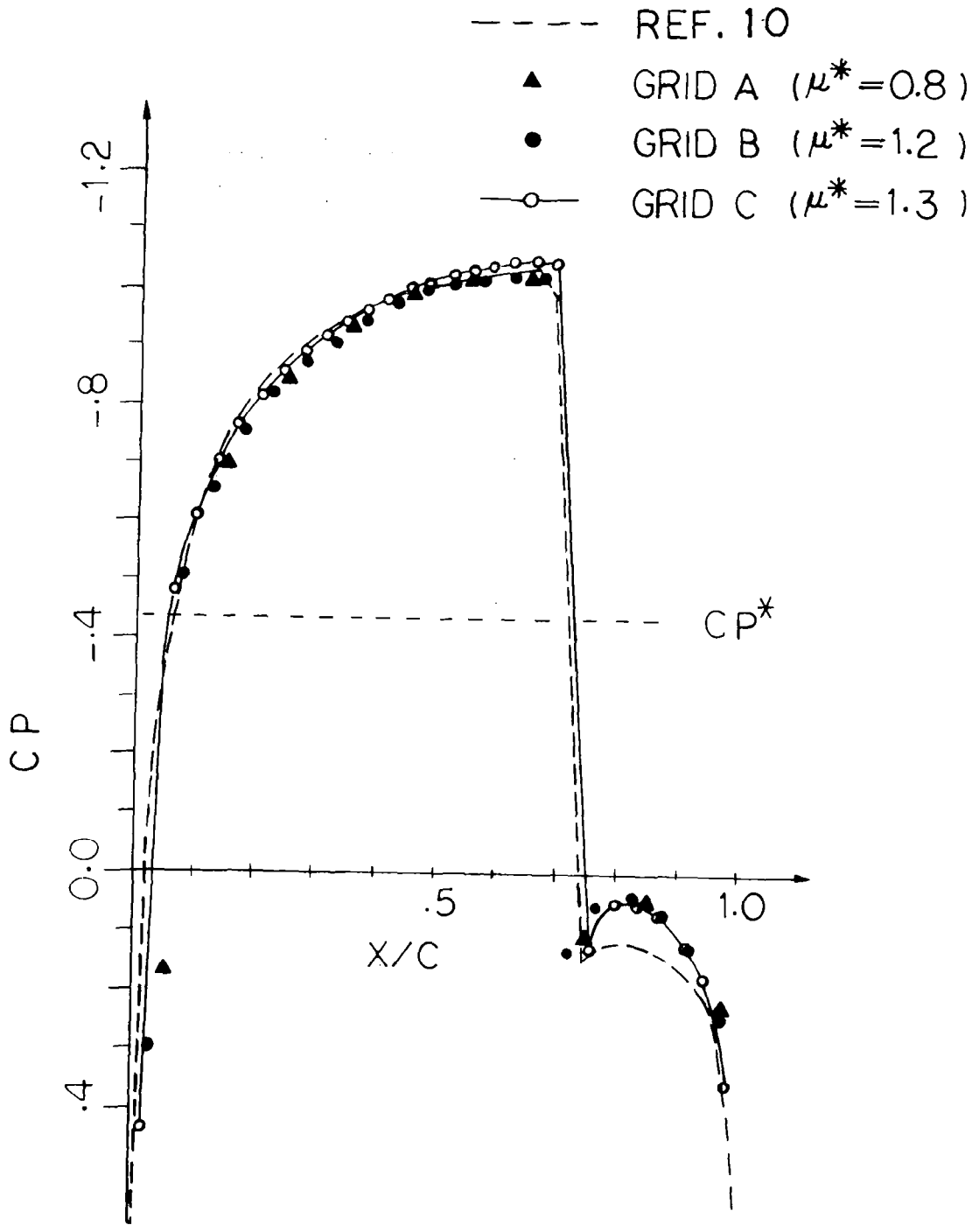

Figure 14. Comparison of final results for various grids

other hand, obtaining solutions with fine grids requires relatively extensive computational effort not only in terms of the number of degrees of freedom but also in terms of the sensitivity of the solutions to perturbations.

Results obtained from grids A and B at a relatively high artificial viscosity content are given in figure 15 for comparison. It is interesting to note that both grids yield essentially the same results.

Figure 16 shows the results obtained from a nonuniform grid. The artificial viscosity in each element was determined based on the element size correction defined in equation (83). Also, shown in figure 16 is a case in which only shock capturing was used with a slightly higher artificial viscosity. Excessive smearing near the shock is of interest in this nonuniform case.

Figure 17 shows the case of a lifting cascade with h/C = 3.6, stagger angle of $\alpha_s = 1.0^o$ and the flow conditions $M_{in} = 0.78$, $\beta_{in} = 0.0^o$, $\beta_{ex} = 1.0^o$. The results obtained using the same arrangement as in grid B are in a good agreement with the finite area results (ref. 11).

Modeling of the Supersonic Pocket and the Shock

The accuracy of the solution in the supersonic pocket is determined in terms of two basic parameters: the artificial viscosity distribution and the modeling of the shock. The importance of introducing correct distribution of artificial viscosities for irregular grids was discussed in reference 15. It was shown that the incorrect artificial viscosity distribution may produce local overshoots or smearing in the solutions. In all the previous test cases, it was also observed that the sensitivity of the solution increased near the shock. For a 45^o staggered cascade of NACA 0012 airfoils with h/C = 3.6, and the flow conditions $M_{in} = 0.80$, $\beta_{in} = 0.0^o$, $\beta_{ex} = 0.0^o$ (Test Case II , page 76) a numerical study was designed to show this behavior by shock capturing technique. The artificial viscosity parameter is defined, following equation (78), in the form:

$$\alpha_e = \bar{\mu}_e m_e \left(1 - \frac{1}{M_e^2}\right) \tag{96}$$

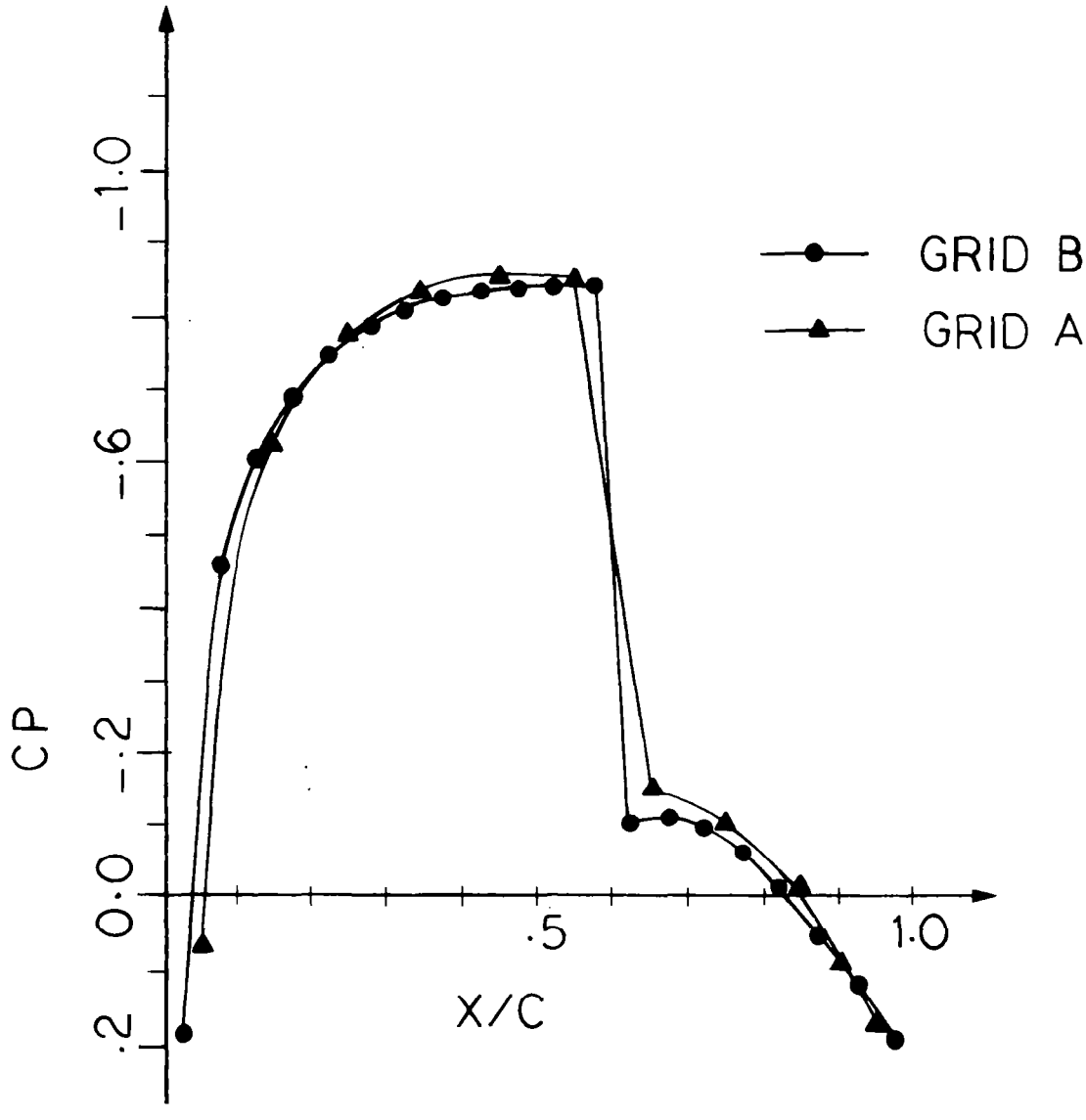

Figure 15. Results of grids A and B at $\mu_e^* = 3.0$

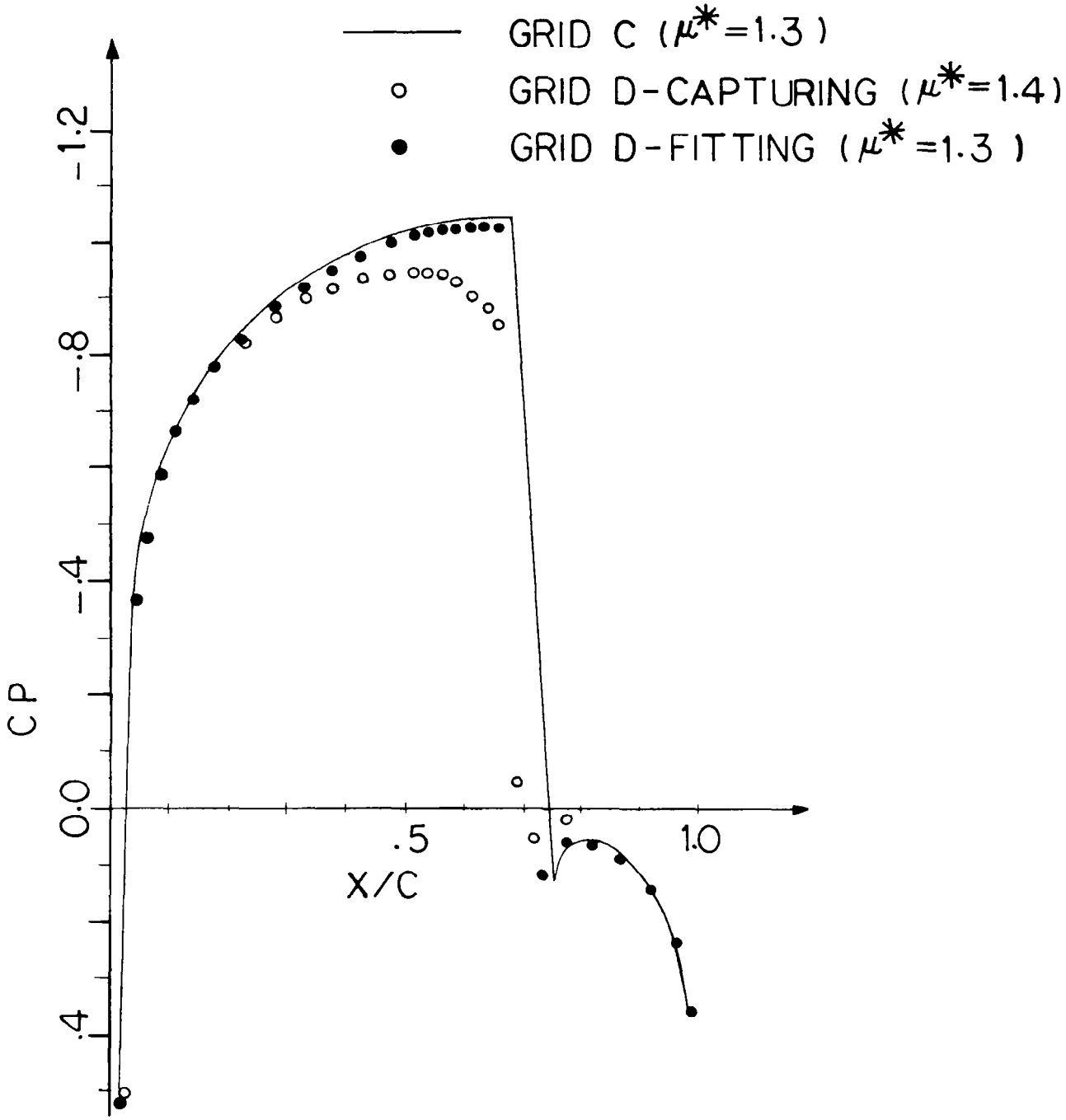

Figure 16. Results for Grid D (Non-uniform grid)

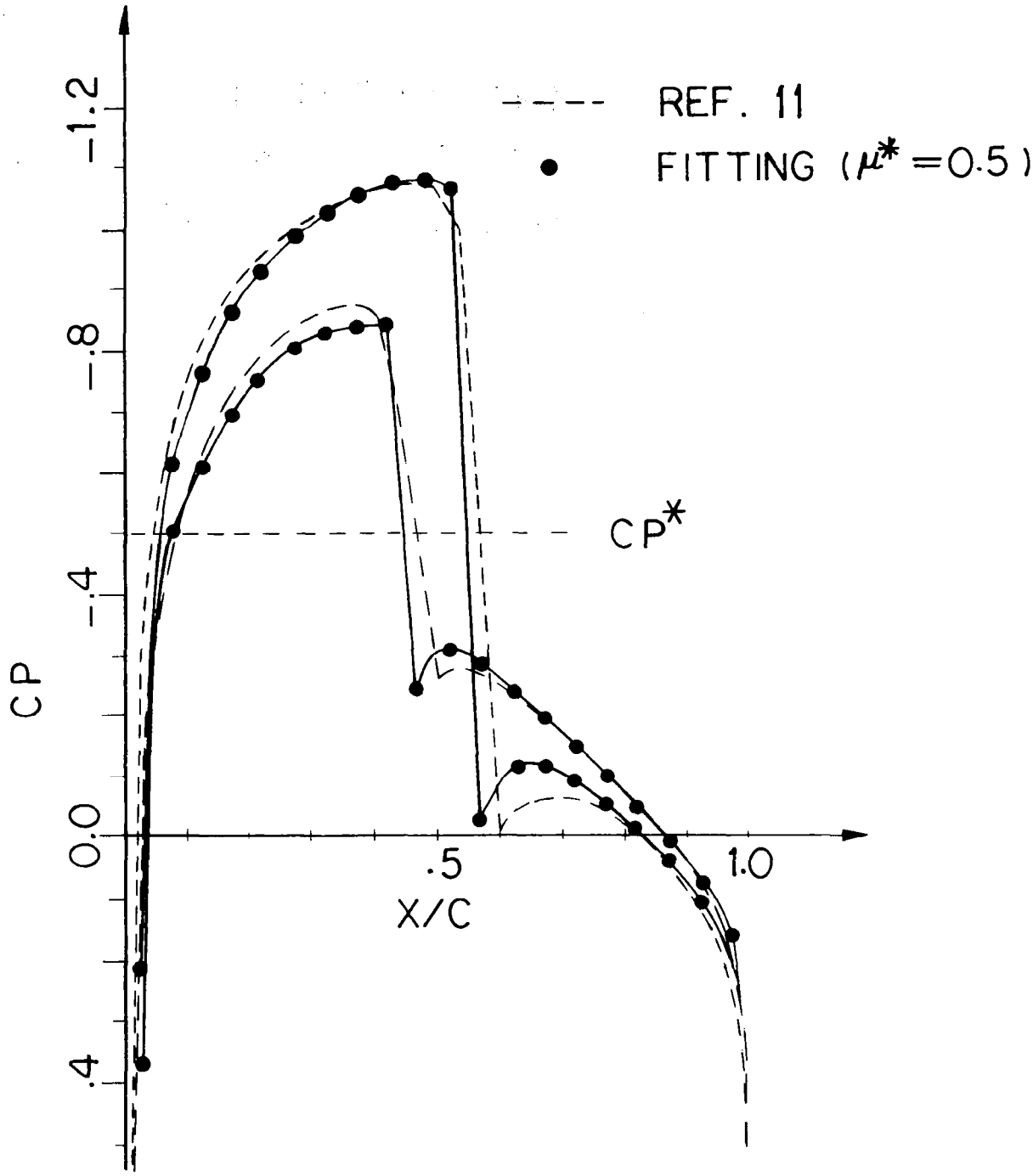

Figure 17. NACA 0012 lifting case - Grid B

Comparing equations (94) and (96) it is seen that

$$\mu_e = \bar{\mu}_e m_e \tag{97}$$

which is a function of the element position in the supersonic pocket, rather than a constant as previously employed. In this case $\bar{\mu}_e$ is a constant, and the three sets of results in figure 18 include $\bar{\mu}_e$ = 0.3, 0.4, and 0.6. All of these results are stable and the deviations from each other are higher at points closer to the shock. The existence of near solutions for different artificial viscosities in shock capturing schemes is apparent, especially around the shock region.

The results shown in figure 18 illustrate the typical accuracy problem observed in the modeling of the supersonic pockets. It is apparent that in all cases the smearing across the shocks are negligible. The two elements on each side of the shock (one with and another without the upwinding of density) provide an accurate modeling of the shock without smearing. On the other hand, the artificial viscosity introduced in the supersonic pocket provides smearing for the entire supersonic pocket. Thus, the strength of the shock is modified due to the artificial dissipation along the entire supersonic pocket. These results suggest that one should be concerned with the modeling of the entire supersonic pocket rather than just the shock for obtaining accurate results. Figures 14 and 18, also suggest that even with rough finite element grids, shocks can be modeled accurately with either capturing or fitting schemes.

One final point to be considered is the use of the artificial viscosity in the subsonic regions past the shock. This is generally referred in the literature as the "cut-off" Mach number, ($M_c < 1$) (ref. 26). The artificial viscosity parameter, α_e, then, is defined with the following expression:

$$\alpha_e = \mu_e \text{ Max } [0,\ 1 - \frac{M_c^2}{M_e^2}] \quad . \tag{98}$$

Depending on the strength of the shock, this usually amounts to introducing additional artificial viscosity at the shock region. Generally it improves the convergence characteristics of the solution. On the other hand, it may produce excessive smearing of the shock region. The comparison of two solutions obtained with $M_c = 1$ and $M_c = 0.95$ values are shown in figure 19 for a sample problem (Test Case IIIc, page 82). These results illustrate the sensitivity of the solutions to the introduction of artificial viscosity at the shock region. Considerable smearing occurs in the shock region which distorts the pressure distribution.

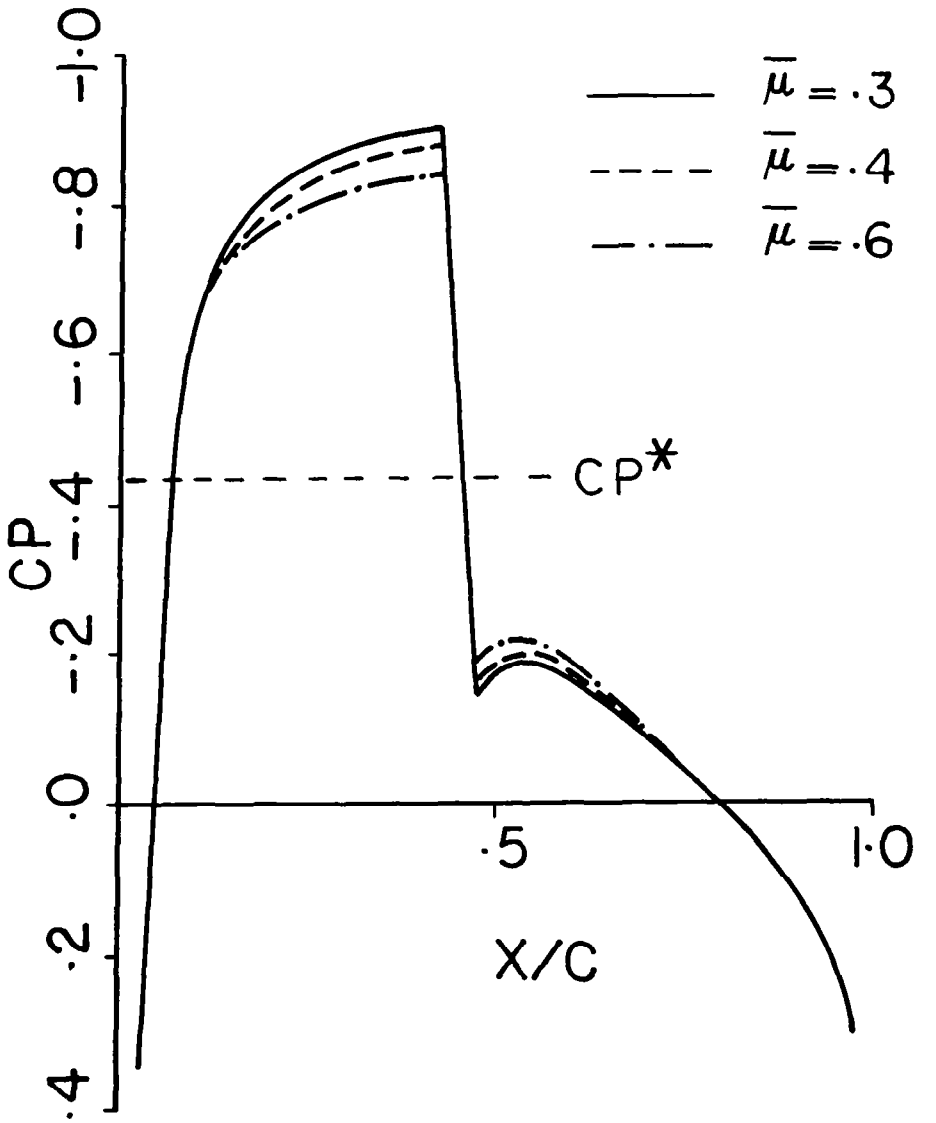

Figure 18. Sensitivity of the flow to the artificial viscosity distribution

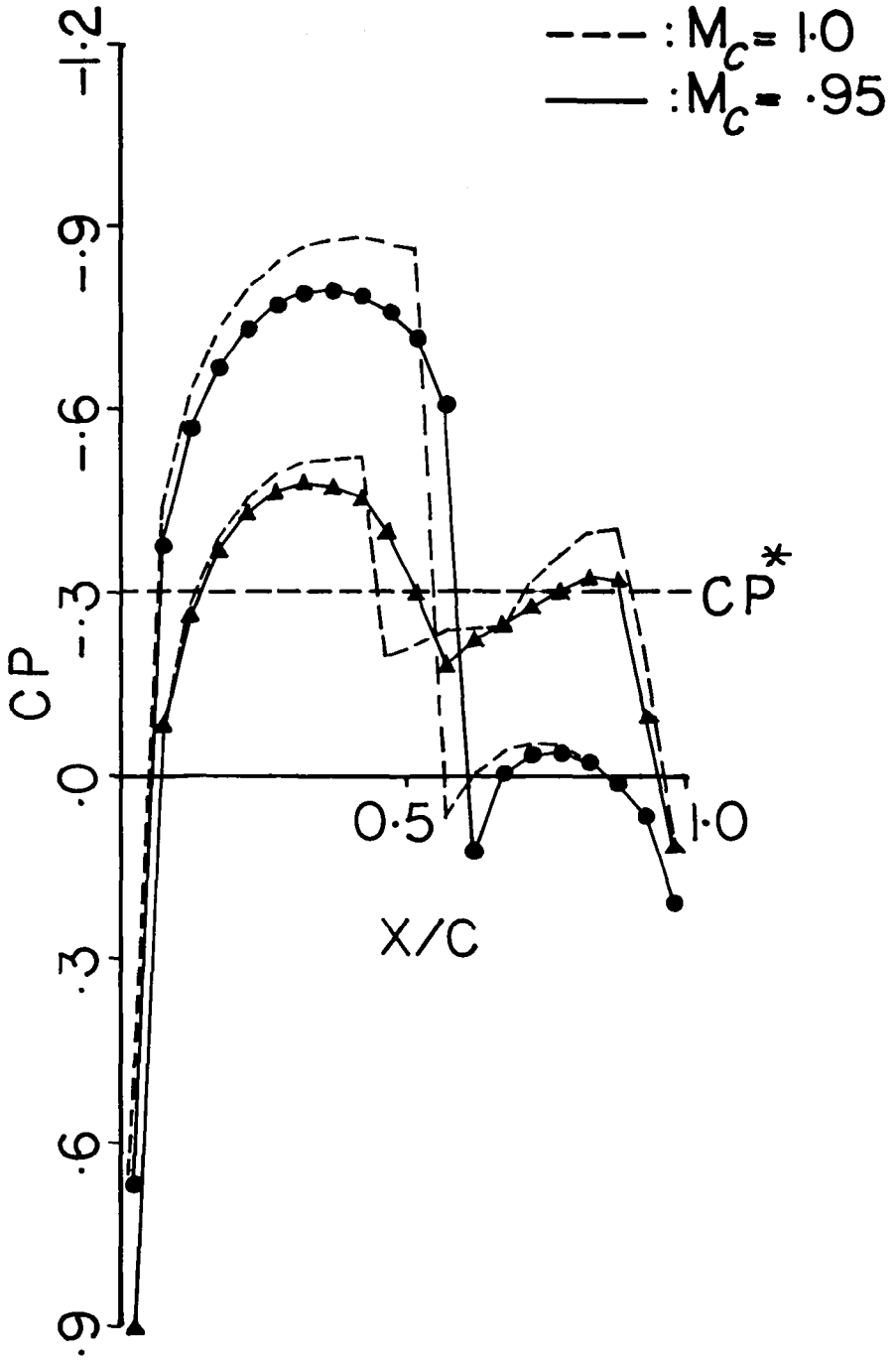

Figure 19. The effect of cut-off Mach number

It can be concluded that the convergence rate should be controlled by varying the overall viscosity distribution in the supersonic pocket rather than introducing additional artificial viscosity around the shock region. The local smearing produced by the above described technique provides confusing results. It should again be noted that the shock fitting technique proved to be valuable in testing the accuracy of the solution in the shock region.

Modeling of the Trailing and Leading Edges

A common feature of the flow equations in these regions is that they are generally elliptic. However, if the supersonic pocket comes closer to either the trailing or the leading edge, one has to consider the accuracy problem there in more detail. For the case of a near singularity in subsonic flows, the method of solution is well defined. One usually designs a radial grid, with degree of refinement varying as a function of the distance from the point of singularity. In the case of elliptic problems, the effect of this singularity decays in the radial direction. For the test cases of NACA 0012 airfoils with blunt leading edges, no particular accuracy problems around the leading edges were observed. In order to obtain sufficient accuracy at the leading edge, only that particular area had to be refined. For the test cases, a coarse model of the leading edge was sufficient to provide an accurate representation of the supersonic pocket.

In the case of the trailing edge of NACA 0012 airfoil, however, the sharpness of the trailing edge further complicates the problem. Inaccurate modeling of the trailing edge strongly affects the magnitude of the produced circulation and changes the overall flow configuration. This behavior was especially found to be important for cascades with high stagger angles. Figures (20) and (21) illustrate the sensitivity of the solution to the changes in the Kutta condition. When the exit flow angles were changed slightly from that predicted by the Kutta condition, for a sample problem (Test Case IIIb, page 82), considerably different sets of solutions were obtained. These examples indicate the necessity of accurately predicting the trailing edge conditions for calculating the transonic flows in highly staggered cascaded.

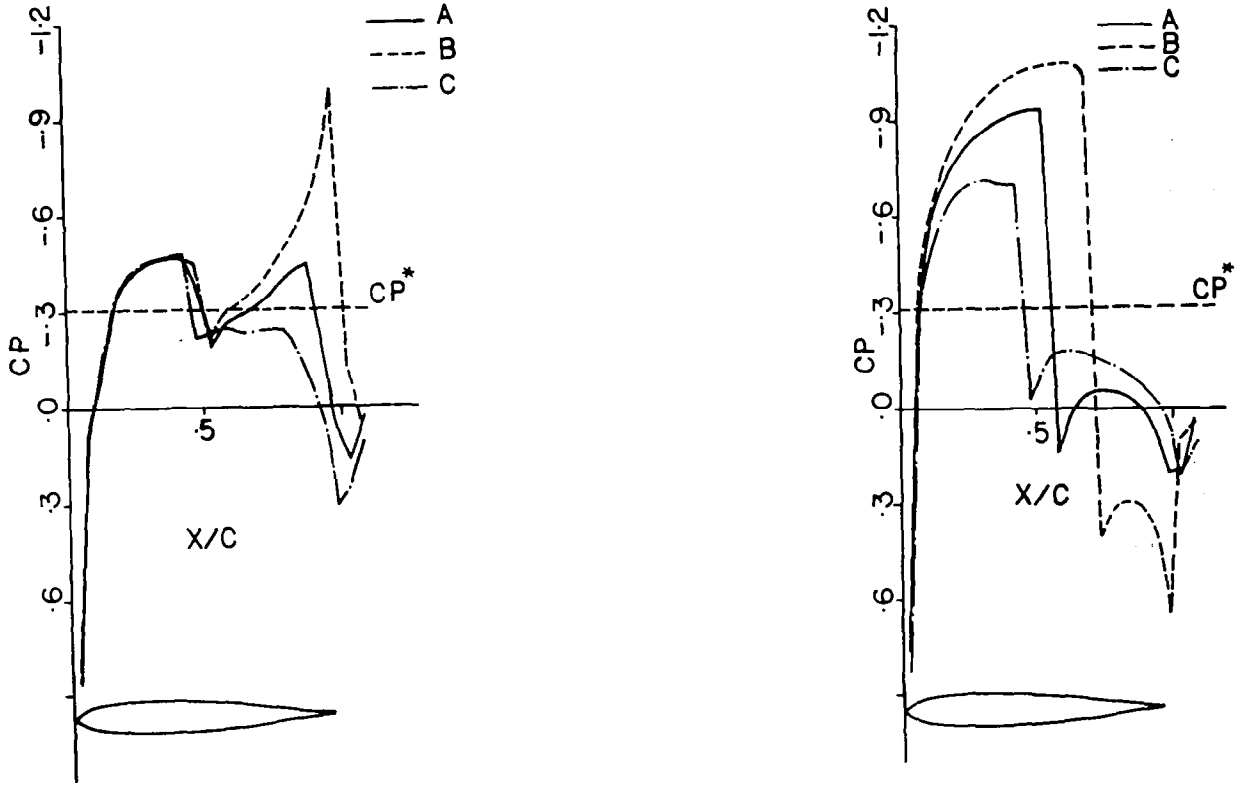

a) upper surface

b) lower surface

Figure 20. Sensitivity of the flow to changes in the exit angle
(A:β_{ex} = 4.7° - Kutta condition, B:β_{ex} = 4.3°, C:β_{ex} = 5.0°)

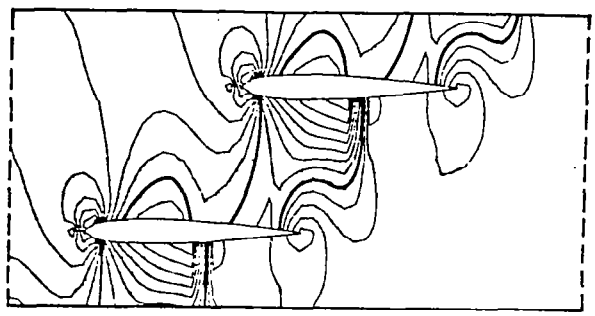

a) $\beta_{ex} = 4.7^{o}$ (Kutta condition)

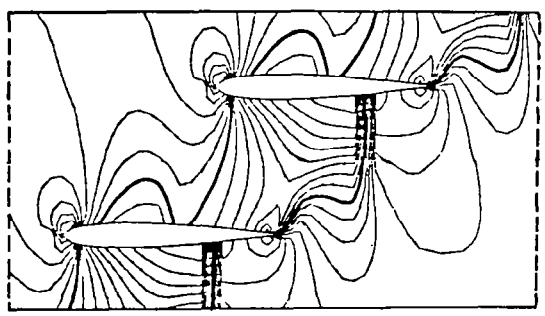

b) $\beta_{ex} = 4.3^{o}$

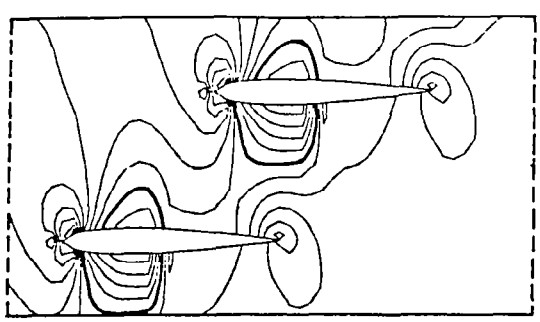

c) $\beta_{ex} = 5.0^{o}$

Figure 21. Iso-Mach lines for Test Case III with varying exit angles ($M_{in} = 0.85$, $\beta_{in} = 0^{o}$)

CASE STUDIES

To illustrate the general applicability of the developed computational procedure and to study the importance of the computational grids for improving accuracy and convergence, several sample cases were tested. The first test case, for transonic flows around a cylinder, shows the sensitivity of flow solutions to computational grids. The second test case illustrates the sensitivity of the transonic flow in the cascade in terms of position of the shock and the trailing edge conditions. The third and fourth cases are the studies of choked and near-choked flow conditions in cascades with high solidity. The final test case is for a highly cambered airfoil for which flow angles change considerably.

Test Case I - Isolated Circular Cylinder

In order to test the applicability of the developed scheme to external flow problems, transonic flow around an isolated cylinder is analyzed for the following farfield conditions of

a) Case Ia: $M_{in} = 0.51$

b) Case Ib: $M_{in} = 0.45$

and compared with results of others (refs. 6 and 19). This problem was chosen to investigate both the importance of the computational grid in blunt bodies, and the effect of imposing farfield boundary conditions at finite distances from the body. It has been observed that the problem is particularly sensitive to the choice of finite grids and the type of applied boundary conditions at finite distances.

Three different radial grids A, B, and C, employed for this purpose are shown, respectively, in figures 22-24. Due to symmetry of the flow, only half of the solution domain is modeled in each case. The farfield boundaries extend radially to an outer radius at $R_o = 10R$ from the center of the cylinder in each case where R is the radius of the cylinder. It is determined that the extension of the grid beyond 10R does not affect the results, but as will be shown subsequently, smaller regions do change the results considerable.

a) Case Ia: $M_\infty = 0.51$. -Two types of boundary conditions are imposed at the farfield boundaries to simulate the uniform flow field for this case.

(i) Type 1 - Velocity potentials are specified:

$$\phi = q_\infty x \tag{99}$$

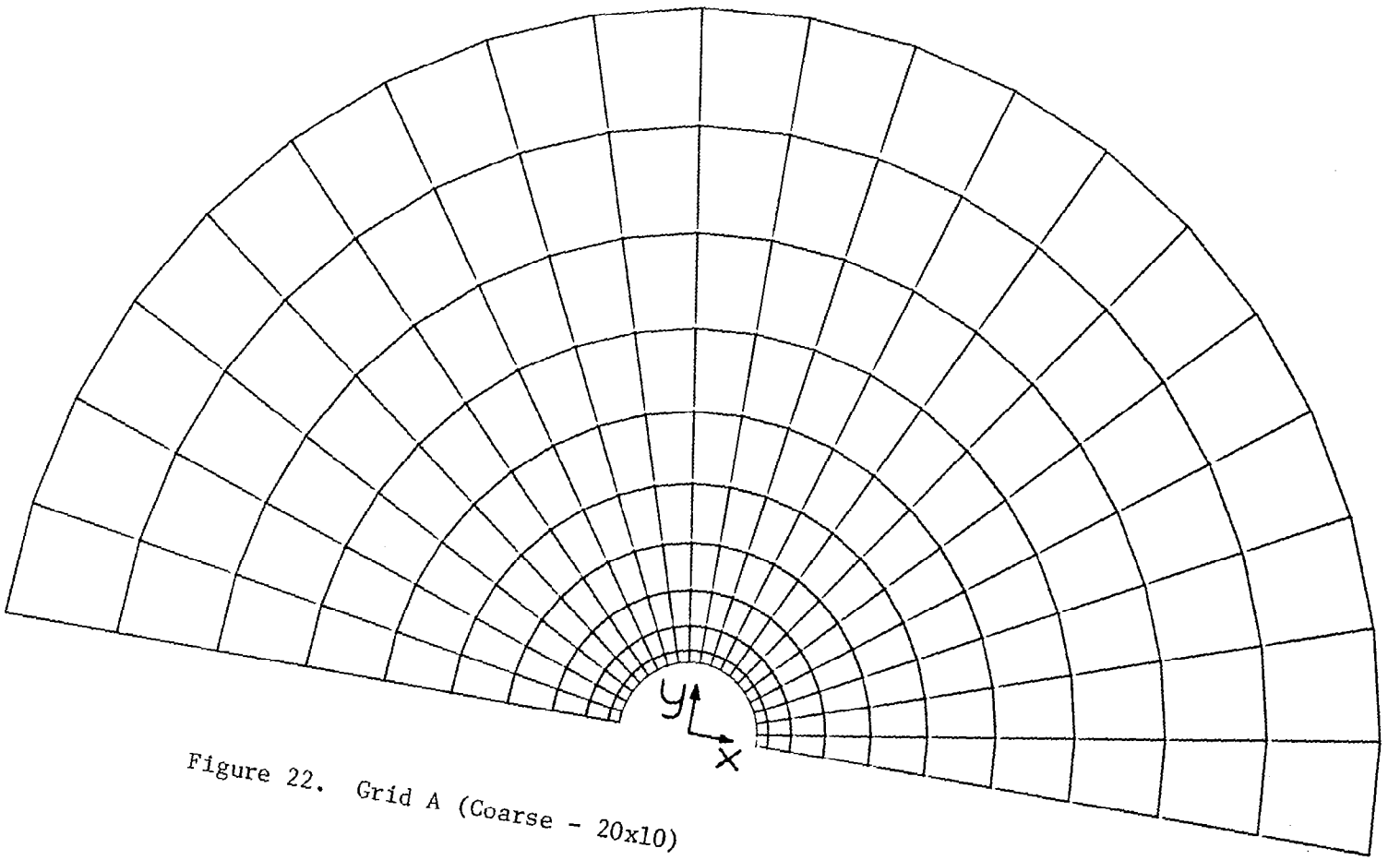

Figure 22. Grid A (Coarse - 20x10)

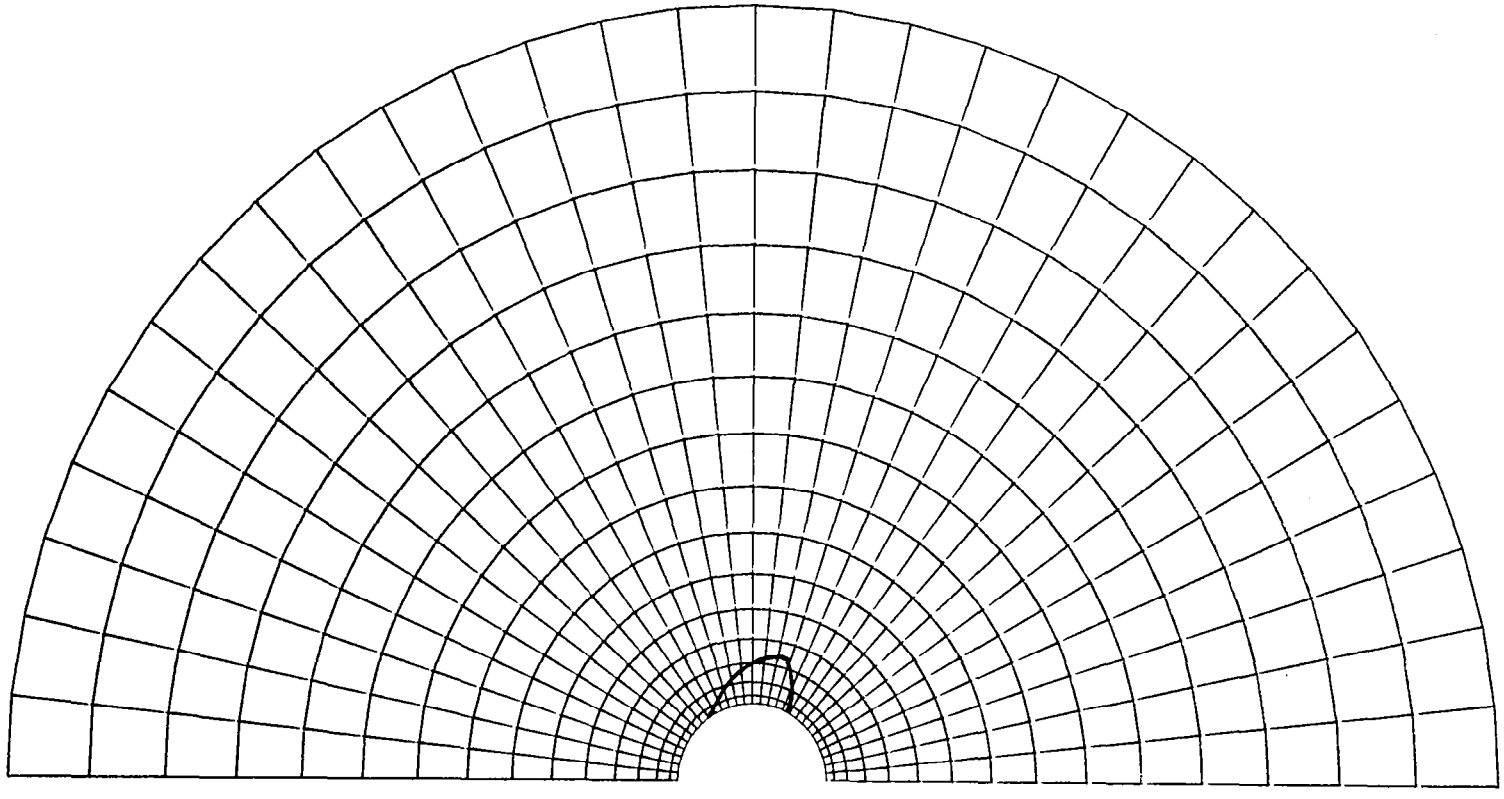

Figure 23. Grid B (Intermediate - 30x15)
(with the sonic line superimposed for M_∞ = 0.51 case)

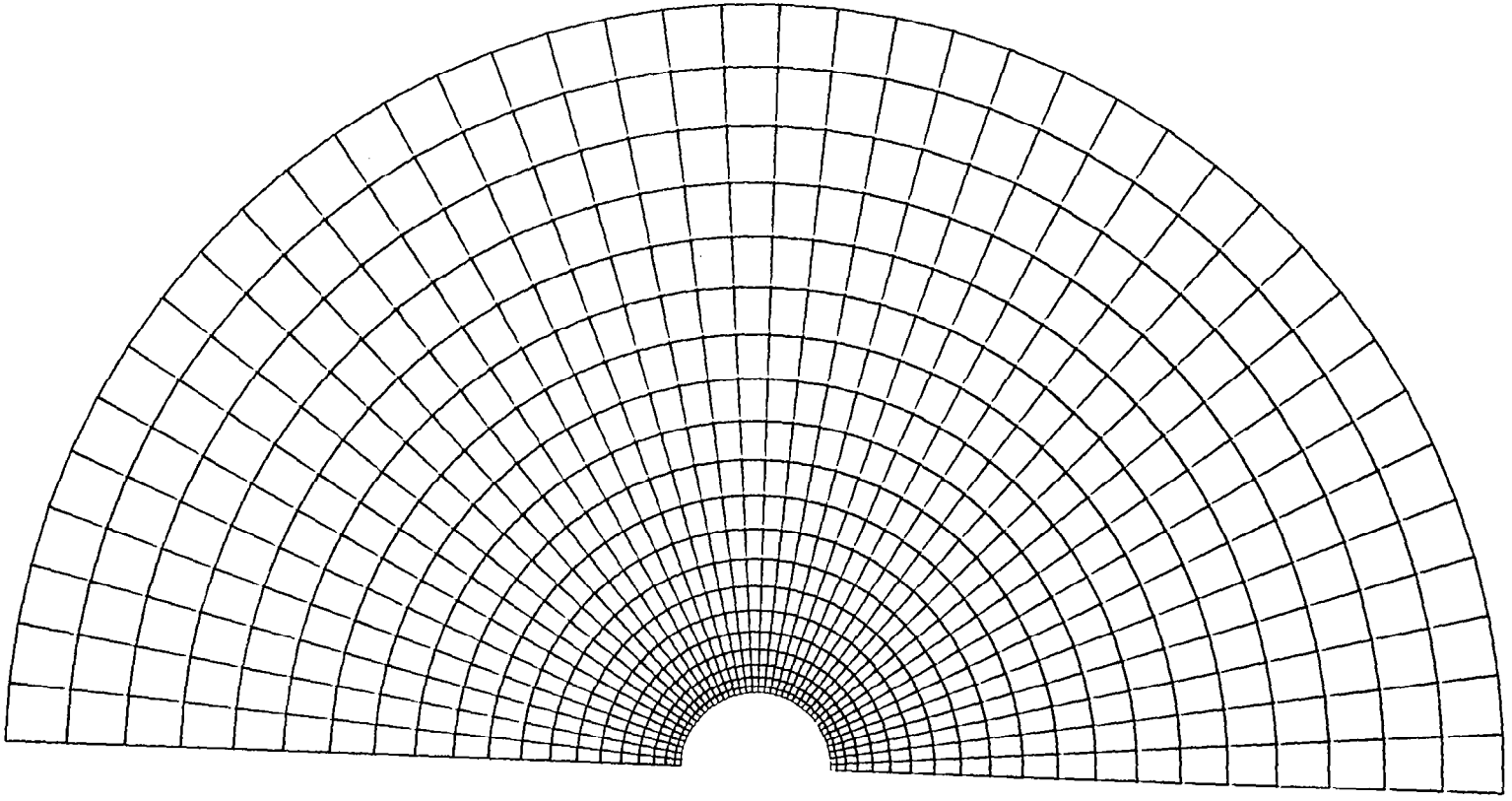

Figure 24. Grid C (Fine - 40x20)

(ii) Type 2 - Fluxes are specified:

$$f = \rho_\infty \underline{q}_\infty \cdot \underline{n} \qquad (100)$$

The surface distribution of the pressure coefficients obtained using all three grids are as given in figures 25 and 26. Results of the intermediate and fine grids are in close agreement whereas the coarse grid results deviate significantly from the other two at the shock. Flux boundary conditions yield slightly stronger shocks and the shock positions are one element further downstream of what was predicted by the velocity potential boundary conditions.

In order to determine the effects of replacing an unbounded domain by a large bounded domain, the above analyses were repeated by taking the far-field boundaries of grid B also at 5R and 14R radial distances from the center. The grids thus obtained are shown respectively in figures 27 and 28. As it is seen from the obtained results in figure 29, the solutions of 10R and 14R grids are in agreement for the velocity potential boundary condition whereas the 5R grid predicts considerable weaker shocks. The comparison of the results for flux boundary conditions in figure 30 indicates an opposite trend and the shock in the 5R grid is stronger.

The above results for the cylinder were obtained by employing the shock capturing scheme. Shock fitting applied to the radial grids shown in figures 22 and 24 failed. This is attributed to the misalignment of the element interfaces with the shock line because, for the shock fitting to be successful, the element interfaces must be reasonably aligned with the predicted shock directions. The degree of misalignment of element interfaces can be determined by computing the direction of the shock line on the surface of the cylinder using isentropic shock-jump relations. For instance, from the computed quantities on two sides of the shock for the grid shown in figure 23 with velocity potential boundary conditions, the shock direction at the surface of the cylinder is predicted to be 85^o with respect to the x-axis (positive counter-clockwise) whereas the interface of the element at that location makes an angle of 60^o with the x-axis. For this reason the radial grid B is modified so that the element interfaces in the supersonic pocket are more in line with the shock direction as shown in figure 31. With the new results in this case, the shock direction is computed to be 92^o while the element interfaces make an angle of 86^o which indicates a better alignment. The comparison of shock fitting and shock capturing results for this case is presented in figure 32. As it is observed, both the shock fitting and the shock capturing results of the modified grid are in good agreement, indicating the accuracy of the solutions. Moreover, slight smearing present at the upstream shock region of the capturing solution in the radial grid disappears with the modification of the grid. For visualization of the supersonic pocket geometry with the computational grid, the sonic line is superimposed both for the regular and the modified grids as shown respectively in figures 23 and 31. Also, iso-Mach and iso-potential lines of this problem are shown in figures 33 and 34. Mach contours in figure 33 are plotted with increments of $\Delta M = 0.1$.

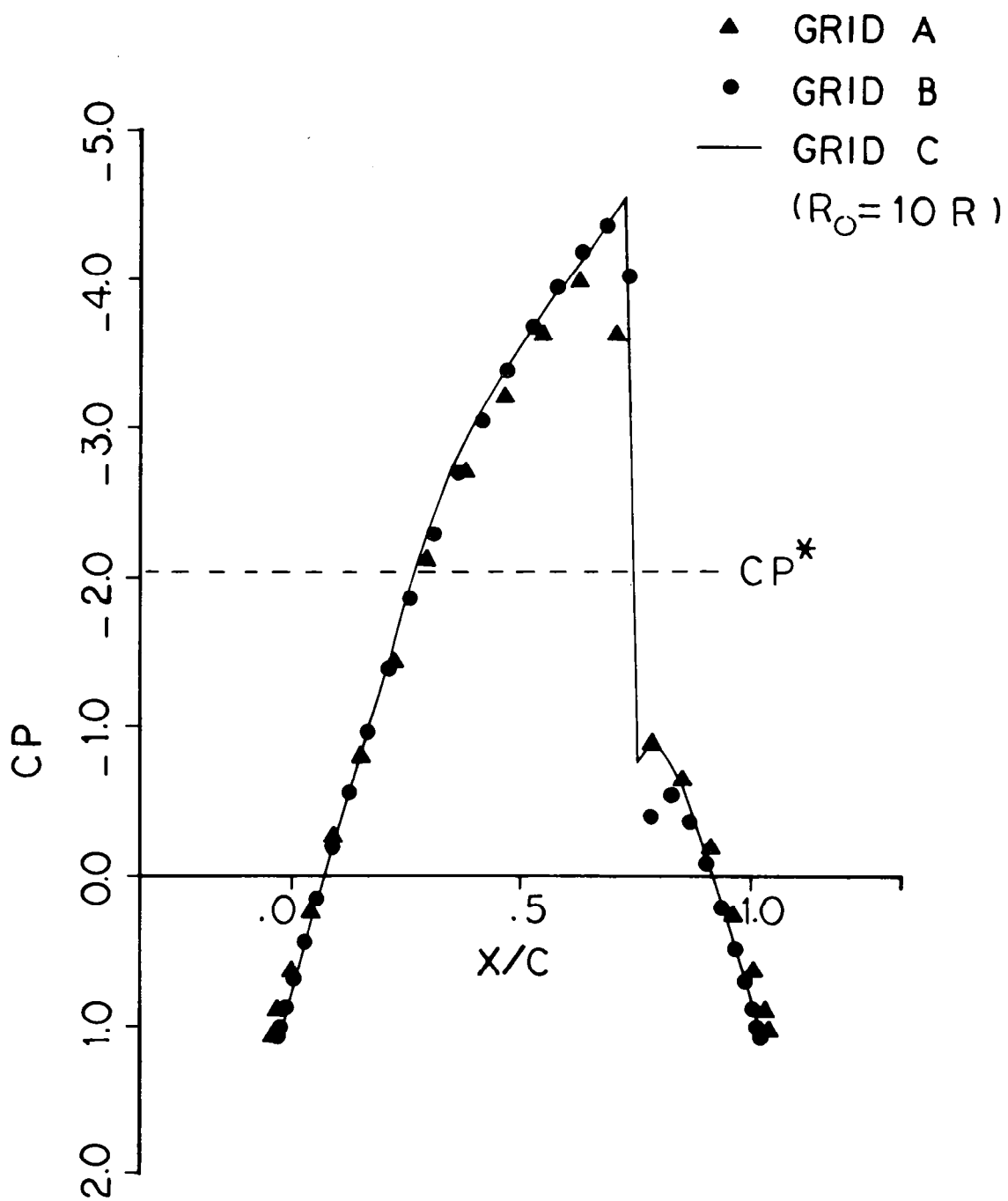

Figure 25. Effect of grid refinement for cylinder (M_∞ = 0.51, ϕ specified)

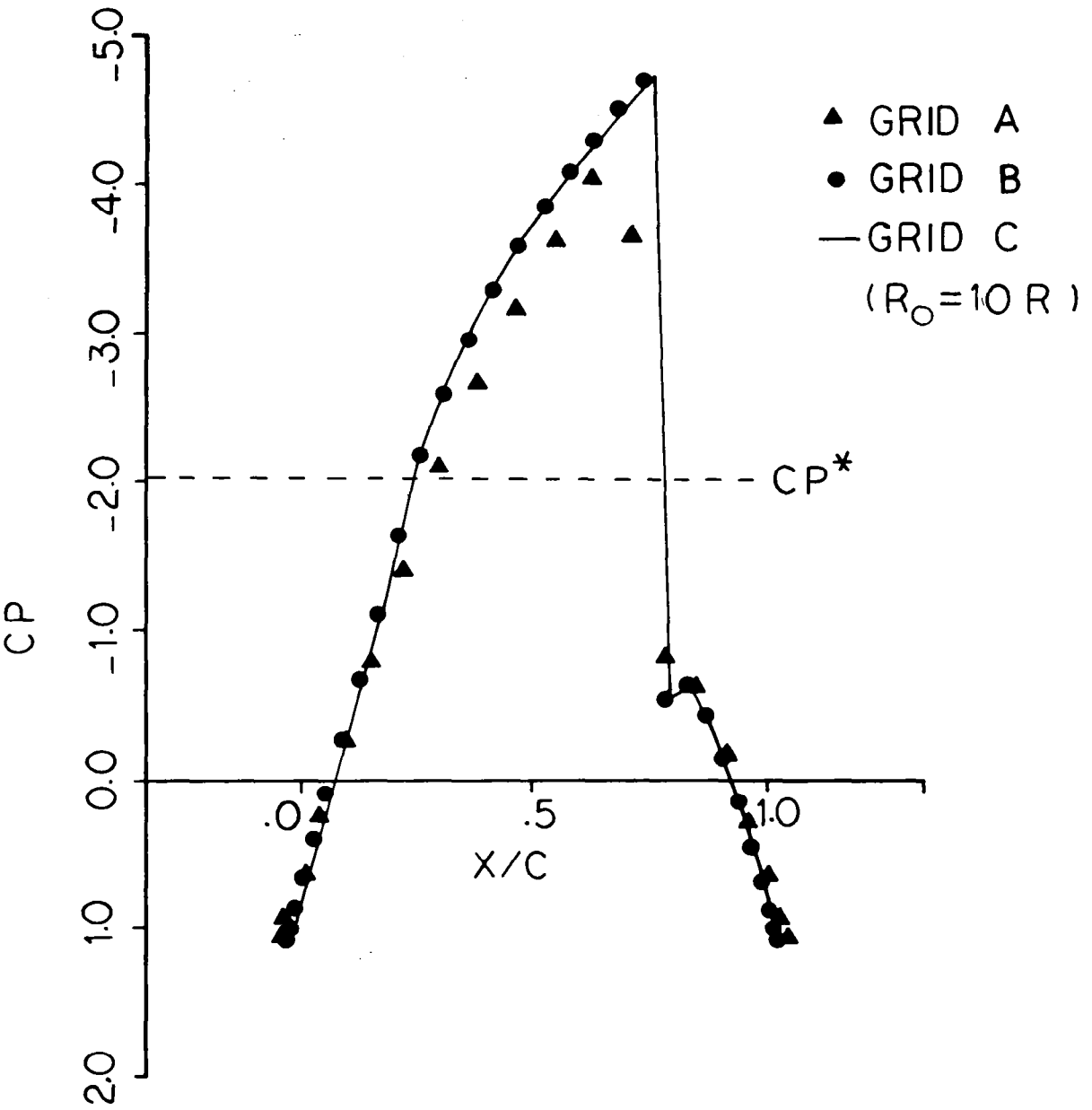

Figure 26. Effect of grid refinements (M_∞ = 0.51, flux specified)

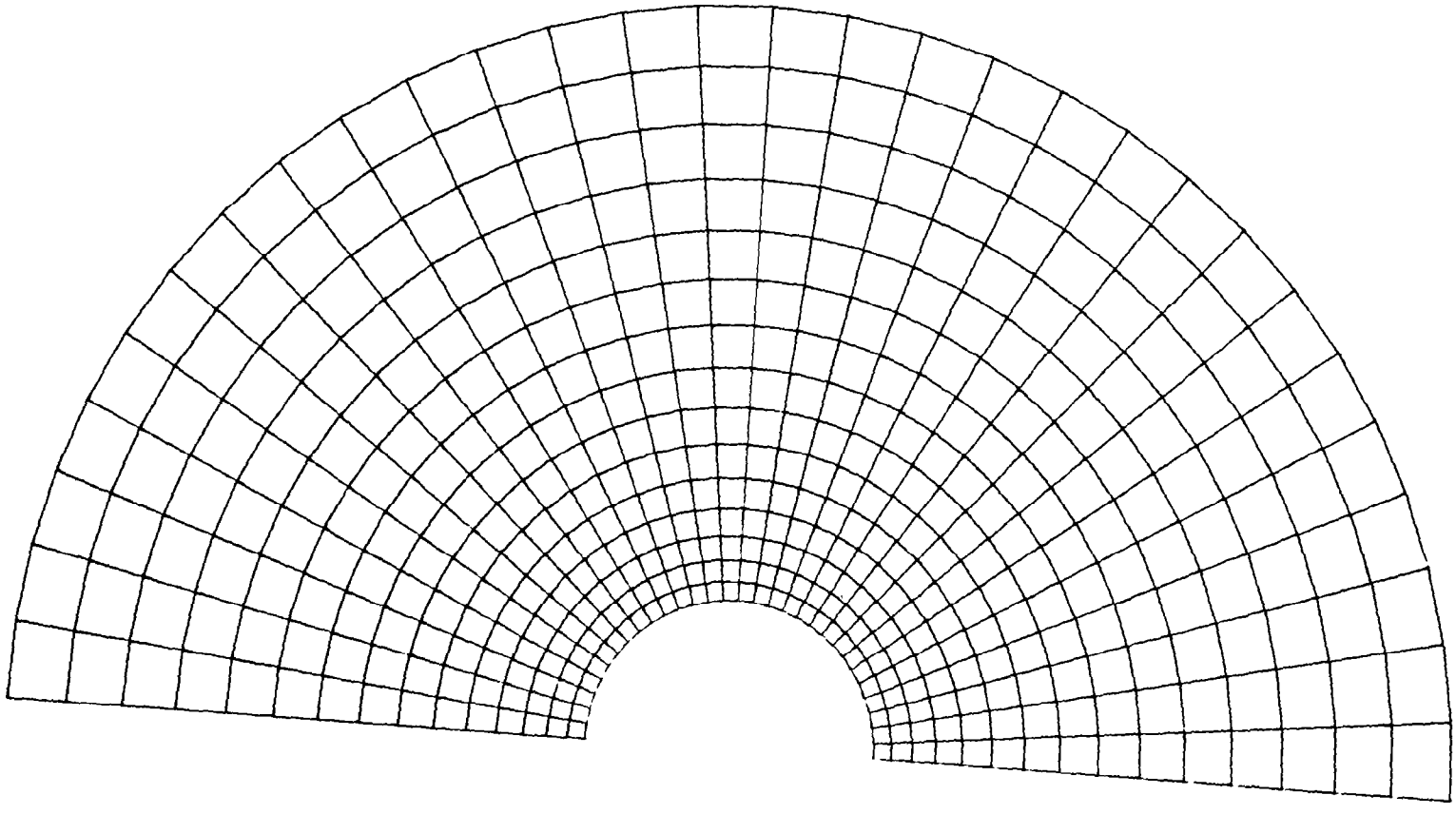

Figure 27. Grid B with 5R outer radius (30x15)

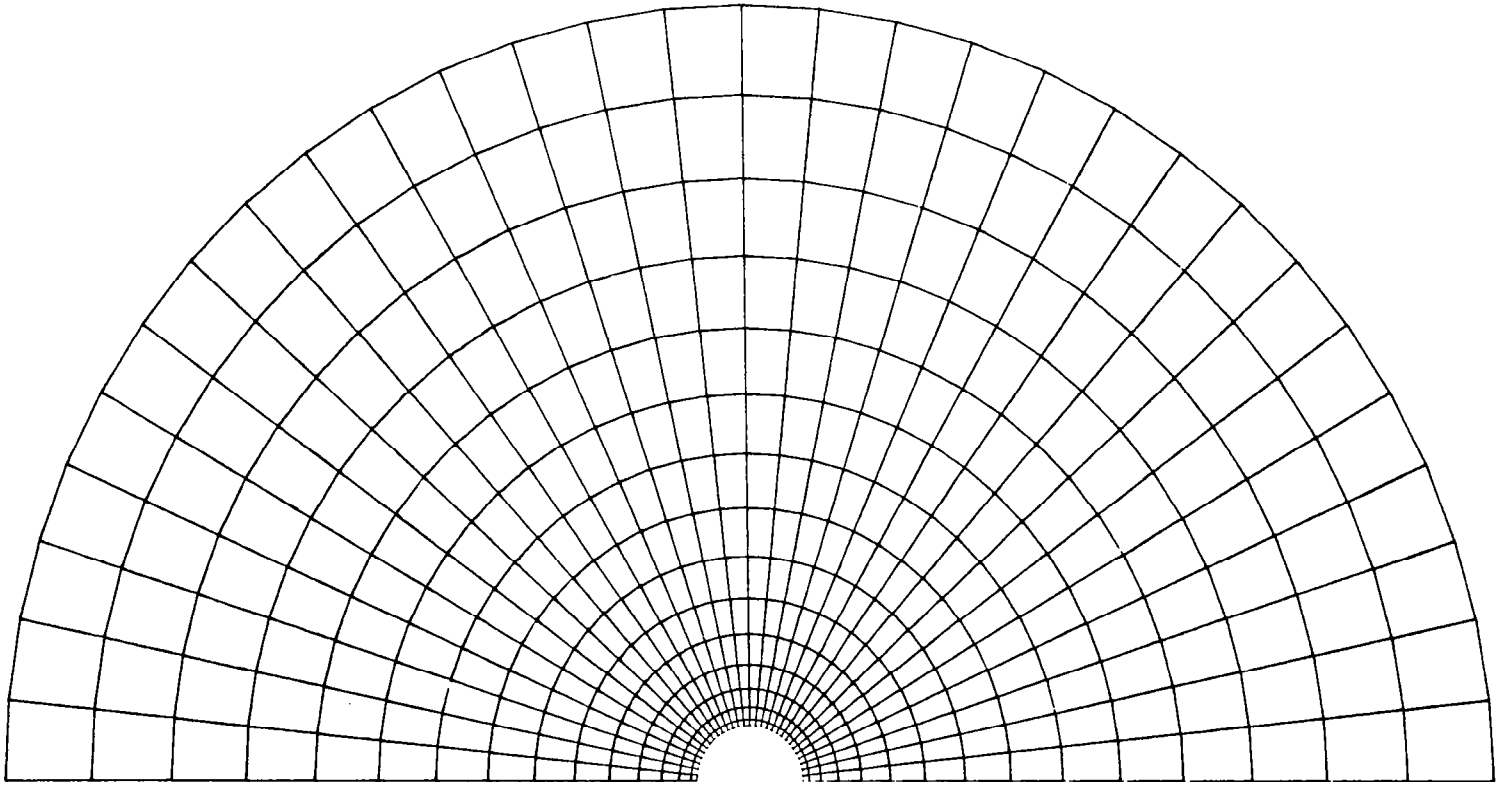

Figure 28. Grid B with 14R outer radius (30x15)

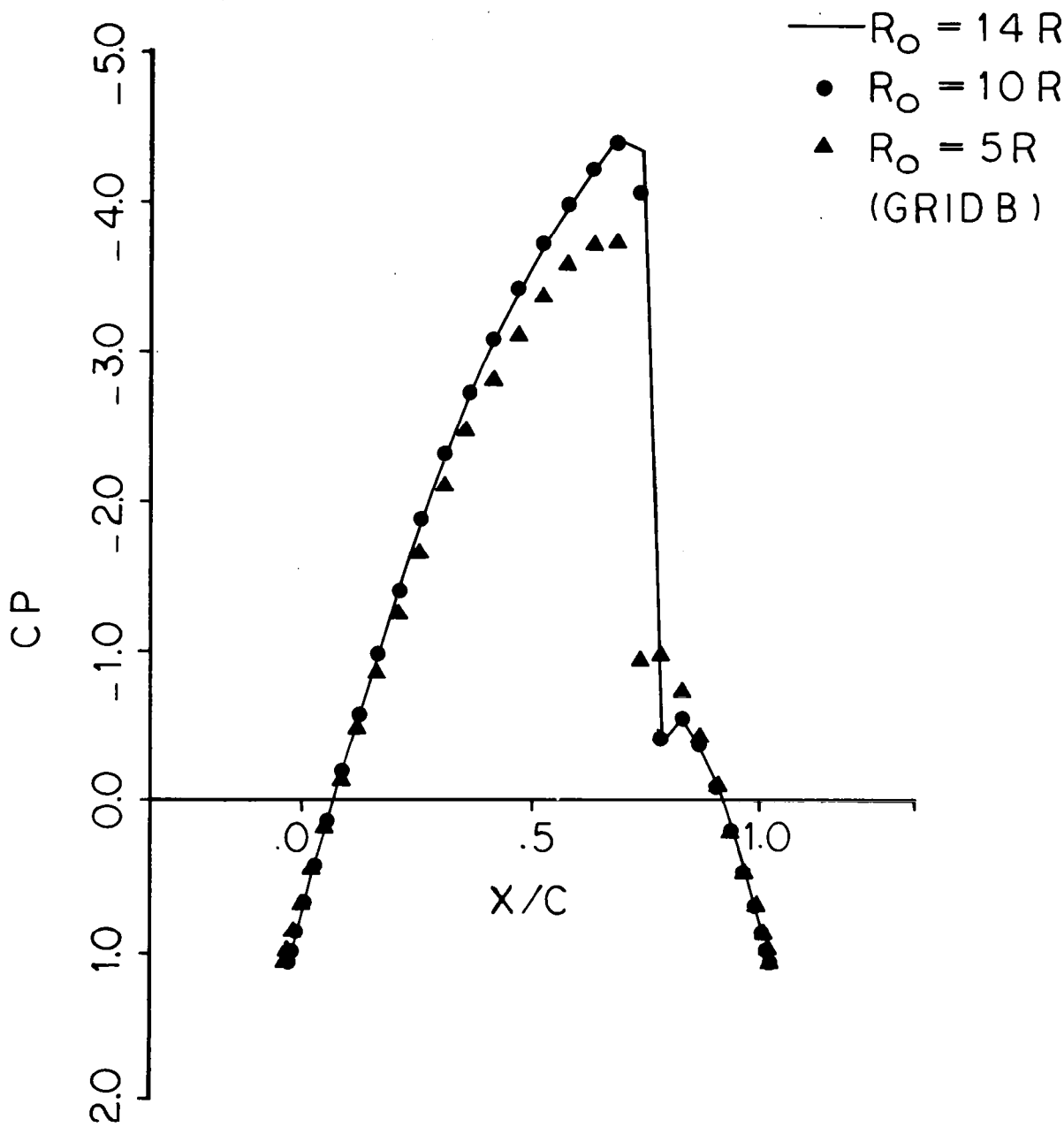

Figure 29. Effect of finite boundaries
(M_∞ = 0.51, ϕ specified)

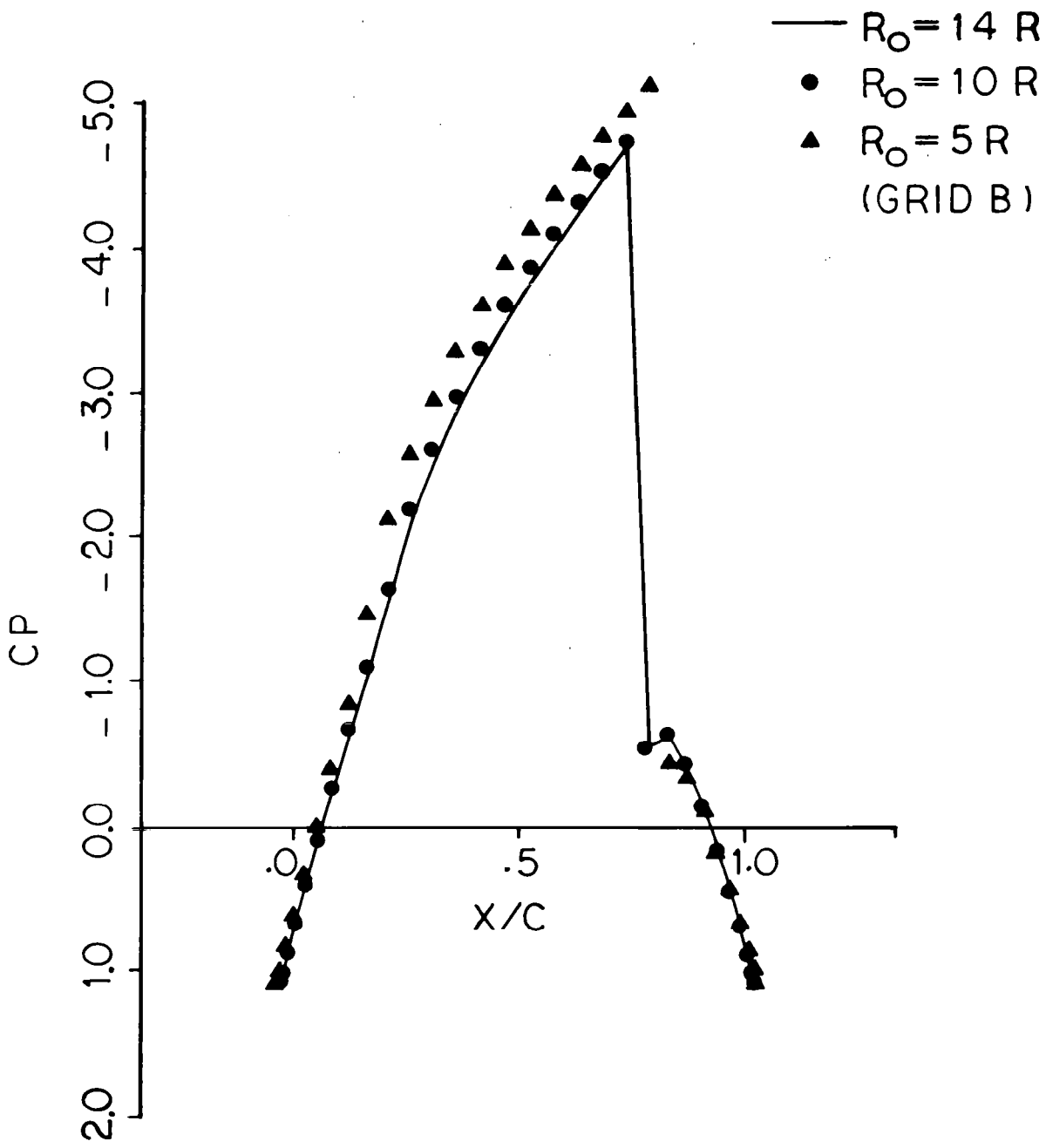

Figure 30. Effect of finite boundaries (M_∞ = 0.51, flux specified)

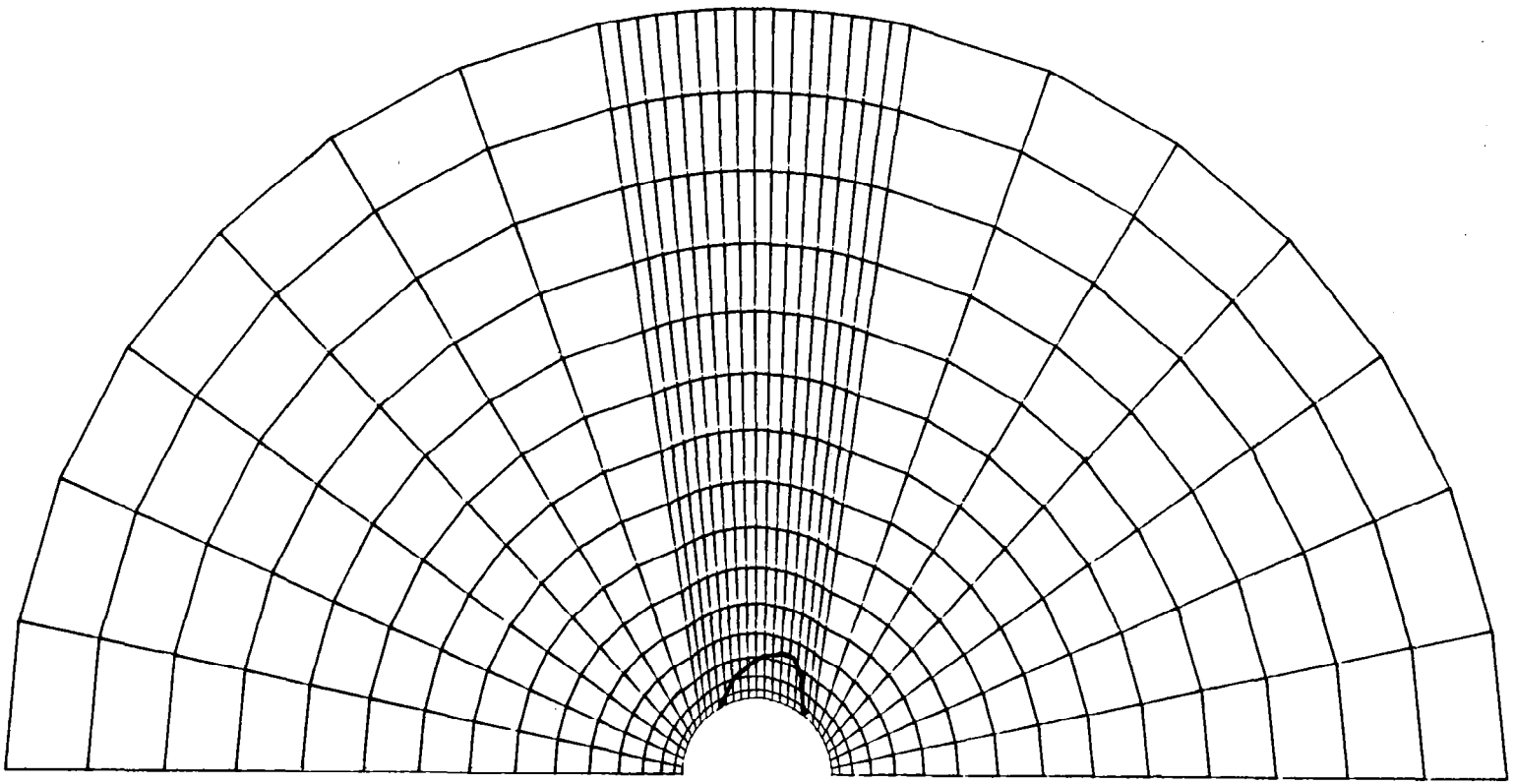

Figure 31. Grid B modified at the supersonic region (with the sonic line superimposed for $M_\infty = 0.51$ case)

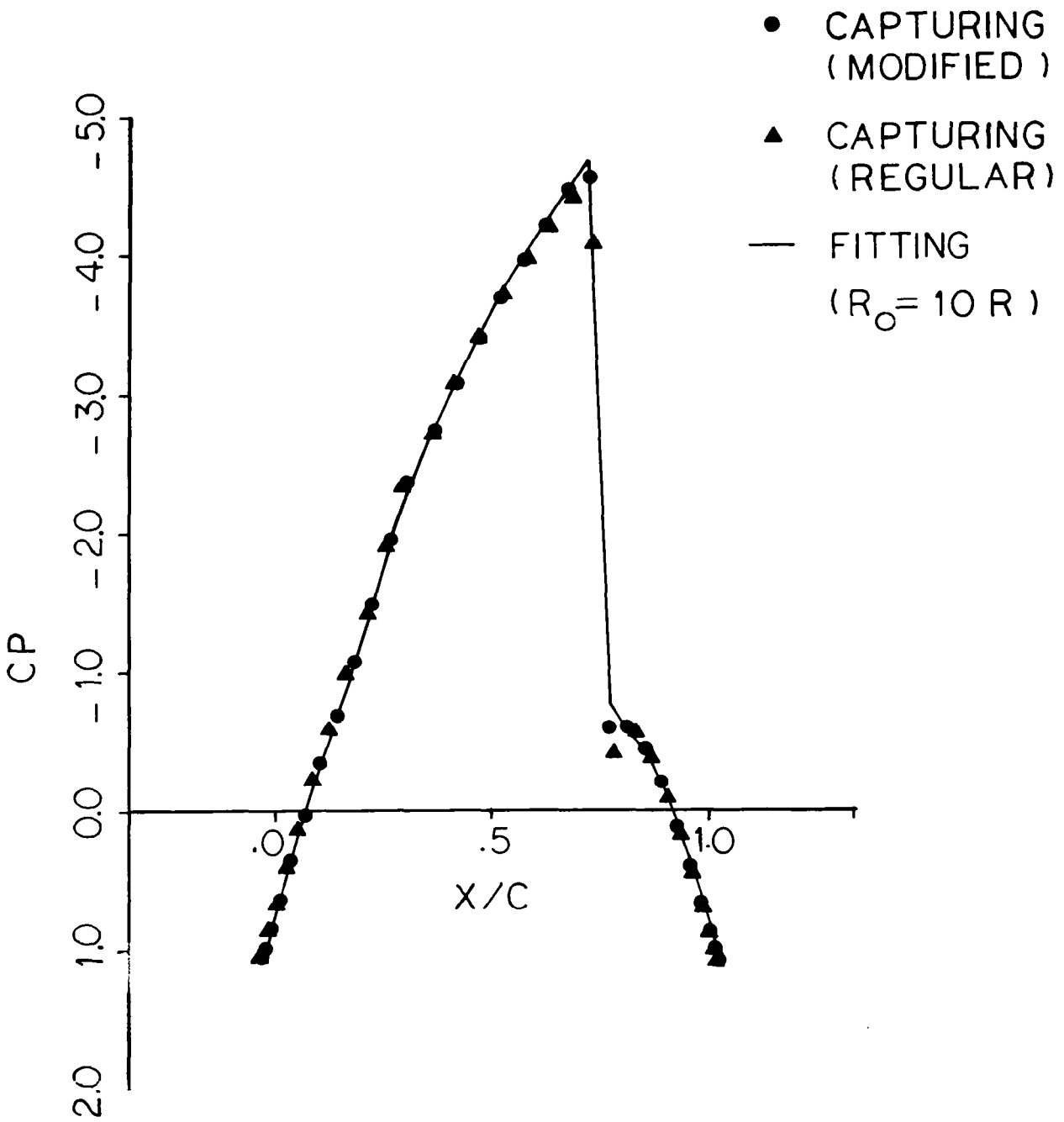

Figure 32. Comparison of shock fitting and shock capturing solutions (M_∞ = 0.51, ϕ specified)

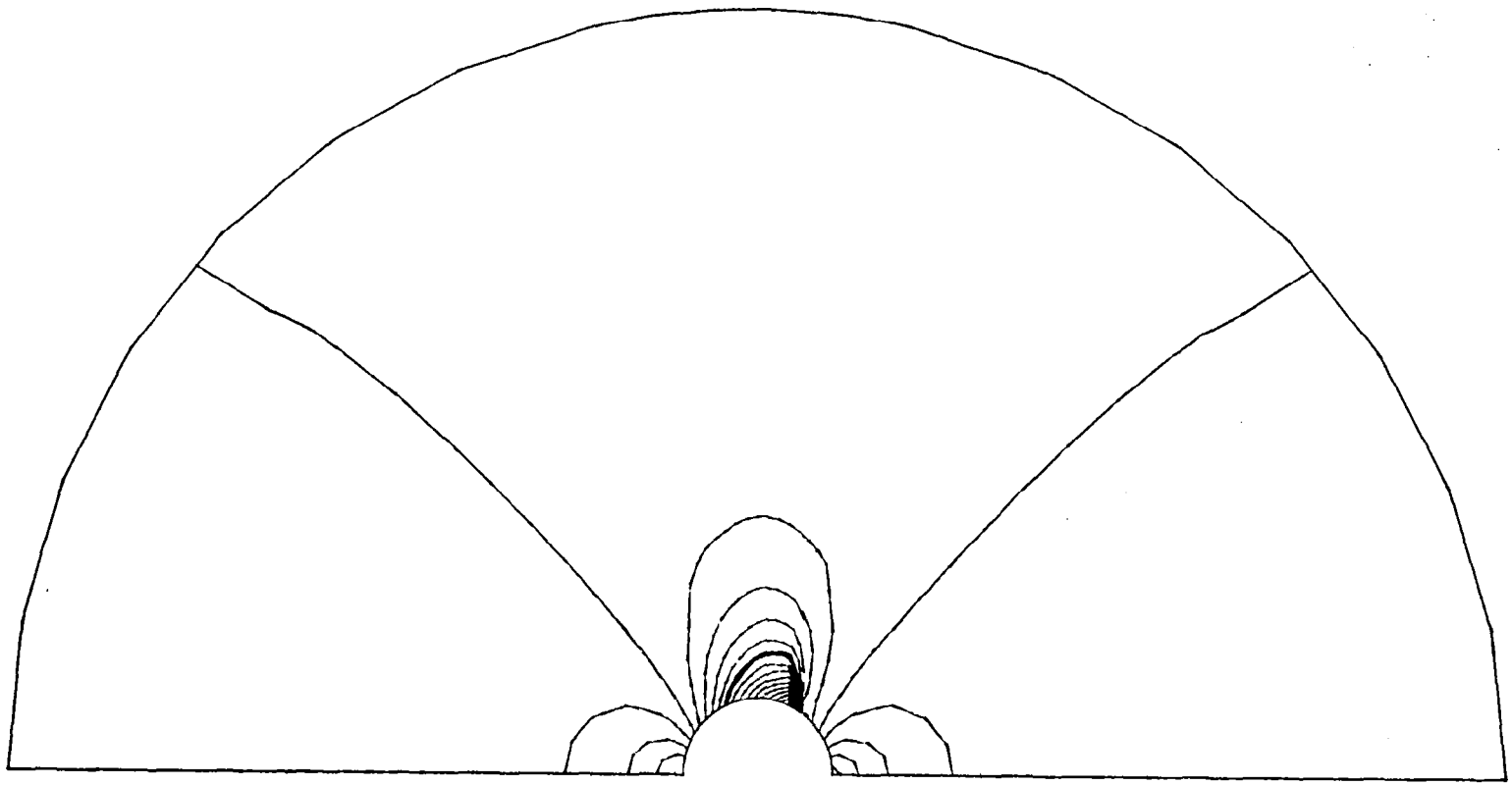

Figure 33. Iso-Mach lines for the modified grid
(M_∞ = 0.51, ϕ specified)

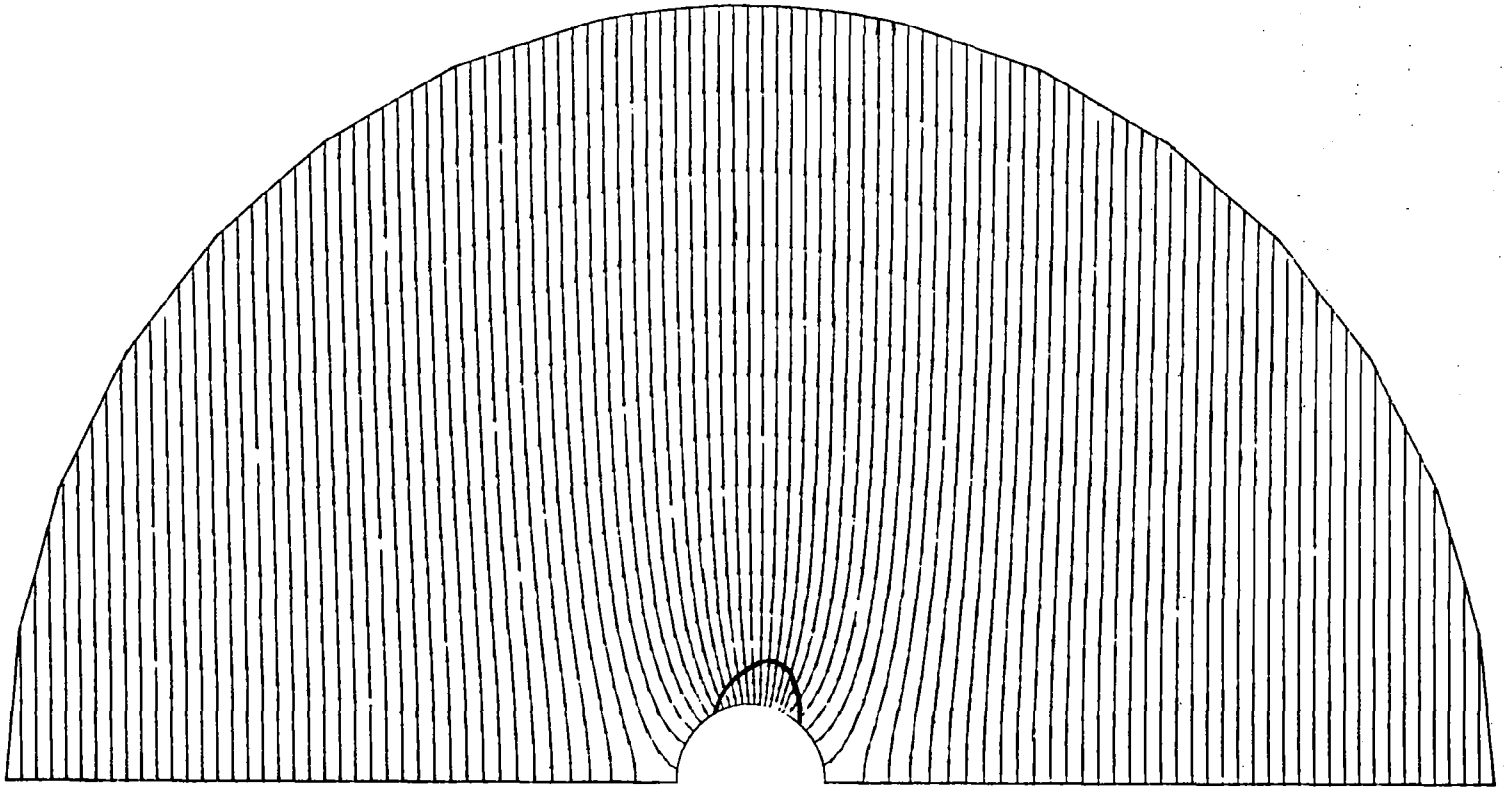

Figure 34. Iso-Potential lines for the modified grid
(M_∞ = 0.51, ϕ specified)

It may be observed from figure 34 that the modified grid is better aligned with the constant potential lines in the supersonic pocket.

The final results obtained for this $M_\infty = 0.51$ farfield condition are summarized in figure 35. Shown in the same figure is the result reported by Hafez, et.al., (ref. 19) who employed a finite difference-artificial compressibility method. For the same problem they have used 60x30 uniform radial grid of 5R outer radius and specified velocity potentials at the farfield boundaries using a farfield formula.

As may be seen, the finite element results obtained for the various boundary conditions, including the result obtained with the addition of a source term to the uniform flow expression in equation (99), are all in close agreement. However, there is a considerable difference between the present results and the result reported in Reference 19.

The application of an additional source term

$$\phi_a = q_\infty \times R^2/R_o^2 \tag{101}$$

obtained from the incompressible potential solution for the farfield did not seem to affect the results of 10R and 14R grids to any noticeable degree but increased the strength of the shock considerably in the 5R grid.

b) Case Ib: $M_\infty = 0.45$. -The effect of grid refinement on the results is summarized in figure 36 for this flow condition. Flux boundary conditions and 10R radial grids were used in each case. As can be seen, both intermediate and fine grids predict essentially the same solution whereas the coarse grid again does not have the required accuracy due to poor resolution near the shock.

Shown in figure 37 are the surface distribution of pressure coefficients obtained using 5R, 10R and 14R intermediate size grids. Also shown in the same figure for comparison is the solution reported by Bristeau, et al., (ref. 6) who employed a conjugate gradient solution algorithm in conjunction with finite elements having a grid of 3456 triangular elements and 1813 nodal points. They have used flux boundary conditions on a large bounded polygonal domain; however, the size of the outer boundary was not indicated. As it may be seen, the present 5R grid solution agrees well with the solution of reference 6.

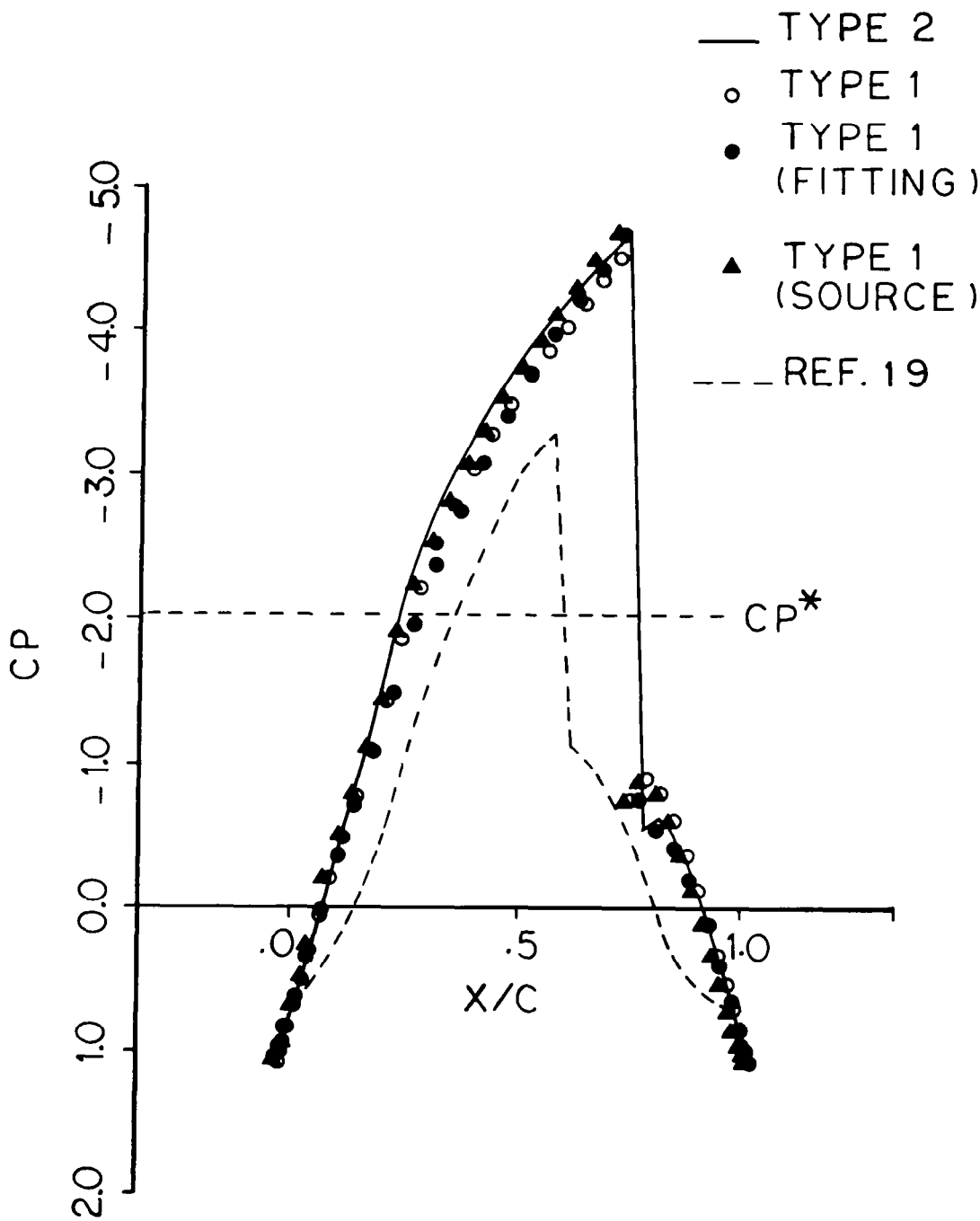

Figure 35. Comparison of final results for $M_\infty = 0.51$ condition ($R_o = 10R$)

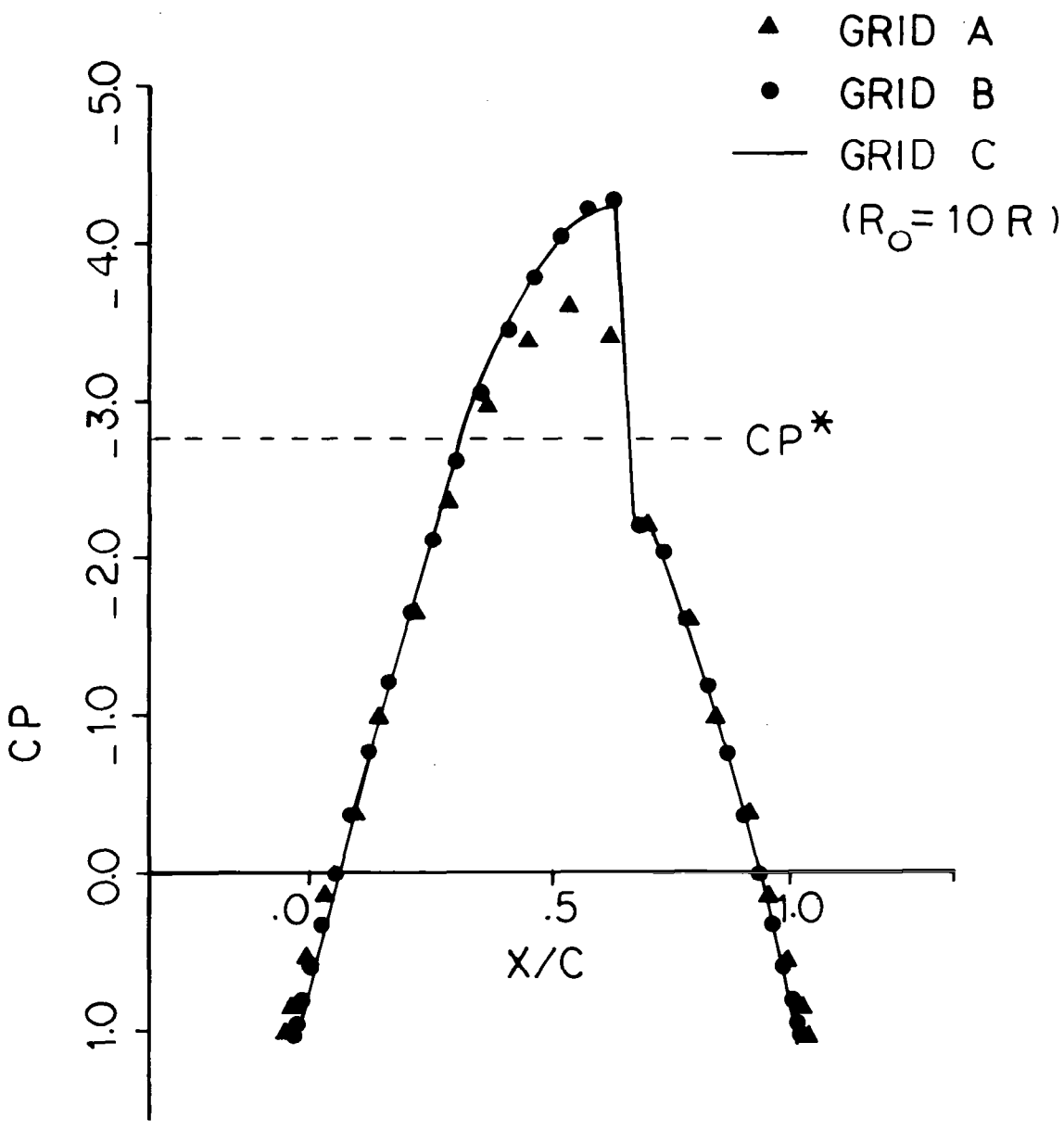

Figure 36. Effect of grid refinements (M_∞ = 0.45, flux specified)

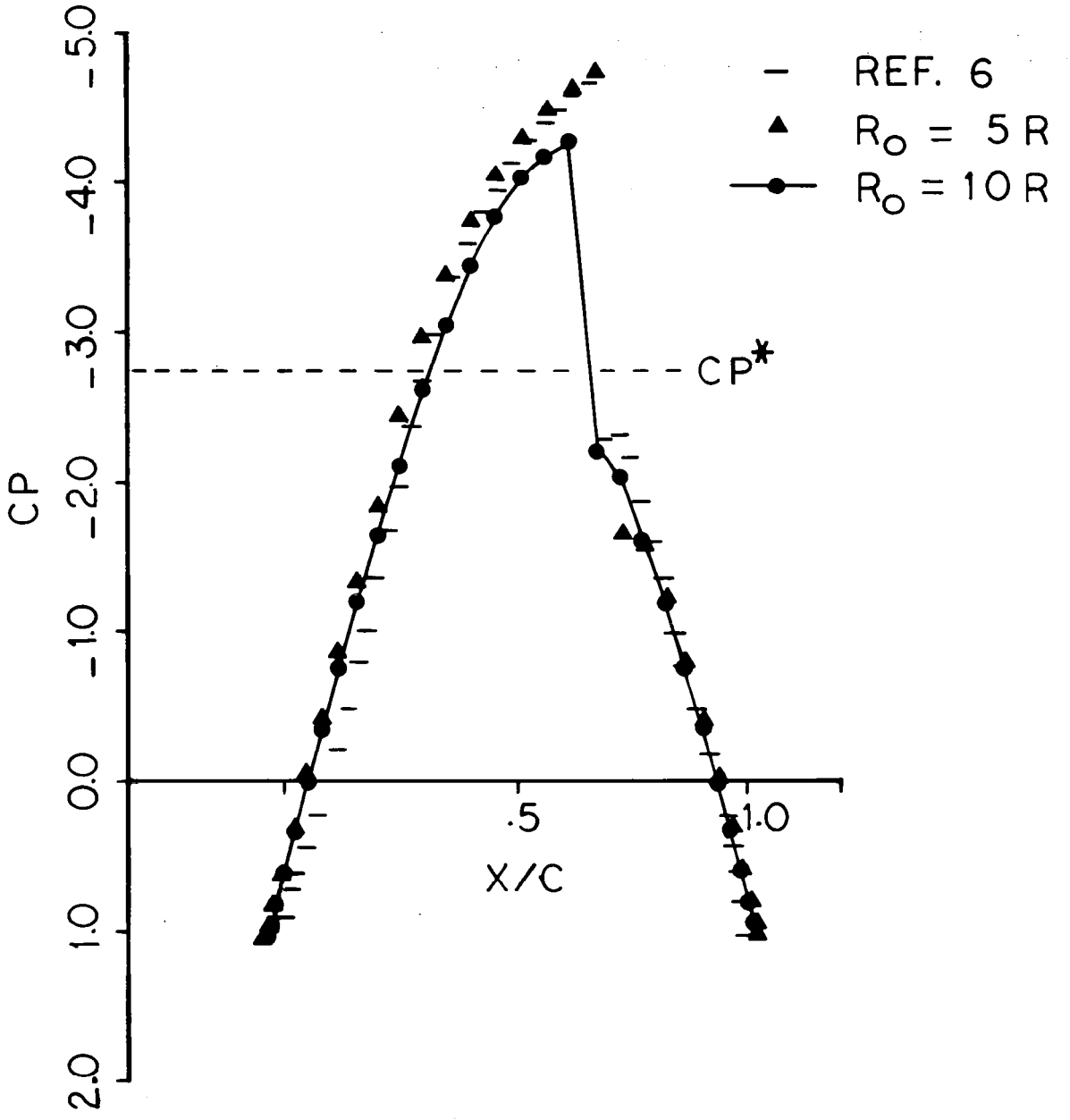

Figure 37. Comparison of final results (M_∞ = 0.45, flux specified)

Test Case II
45^{o} Staggered Low Solidity NACA 0012 Cascade

A cascade of NACA 0012 airfoils with a 45^{o} stagger angle and h/C = 3.6 is analyzed for the following inlet flow conditions:

Case IIa: $M_{in} = 0.8$, $\beta_{in} = 1^{o}$

Case IIb: $M_{in} = 0.8$, $\beta_{in} = 0^{o}$

Case IIc: $M_{in} = 0.8$, $\beta_{in} = -1^{o}$

Kutta condition was applied at the trailing edge for the above cases.

The chordwise distribution of the pressure coefficients obtained for each case using the finite element grid shown in figure 4 on page 19 are respectively given in figures 38-40. There are only 20 elements over each surface of the airfoil in this grid. The plotted results are those computed at the centroid of each element. With the combined shock capturing and shock fitting scheme, convergent unique solutions were reached at μ_e = 1.25, 1.5 and 4.2 respectively for Cases IIa, IIb, and IIc. For these cases the maximum computed local Mach numbers were respectively M_e = 1.25, 1.16 and 1.07 over the upper surface, and M_e = 1.11, 1.26 and 1.39 over the lower surface of the airfoil.

The need for large artificial viscosity in Case IIc is attributed to the size of the supersonic pocket, as has been implied by the von Neumann convergence analysis. The greater the size of the supersonic pocket, the higher the amount of artificial viscosity required for uniform convergence. This general trend is evident in all three cases analyzed herein.

The development of sharp shock fronts with almost no smearing and the satisfaction of the trailing edge Kutta conditions are apparent in all cases. In addition, figures 38-40 show that, with the above set of artificial viscosity multipliers, μ_e, more smearing is produced along the upper surface of the airfoil regardless of the local Mach number. This may be attributed to the slight misalignment of the grid with the local flow direction.

Iso-Mach line plots of the above three cases are presented in figures 41-43. On these figures sonic lines are denoted as darkened contours. The size of the supersonic pocket and the extension of the shock beyond the mid-channel of the cascade in Case IIc are of interest. In this case, with the higher values of artificial viscosity, convergent solutions were obtained initially with the shock placed close to the mid-chord of the airfoil. As the artificial viscosity was reduced, the shock moved downstream and the size of the supersonic pocket was increased. Each time the artificial viscosity was reduced, shock fitting was applied to the convergent shock

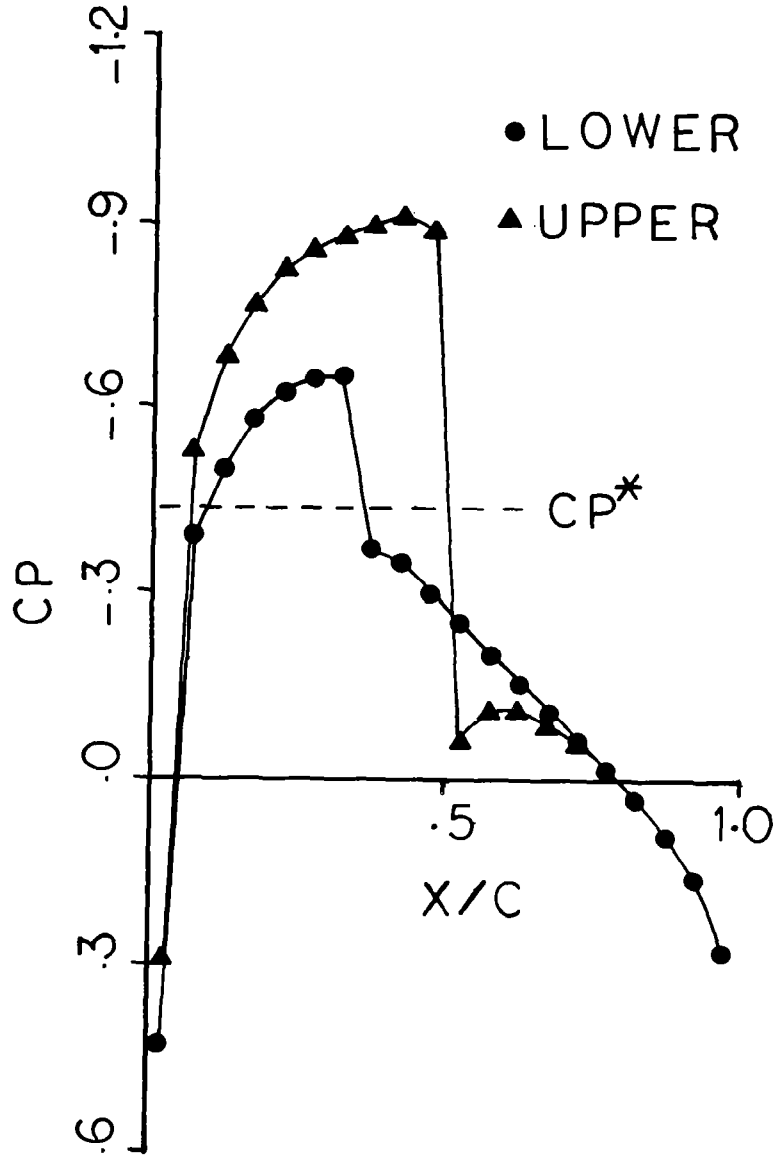

Figure 38. Variation of pressure coefficients over the airfoil for Case IIa ($M_{in} = 0.8$, $\beta_{in} = 1^{o}$, $M_{upper\ max} = 1.25$, $M_{lower\ max} = 1.15$)

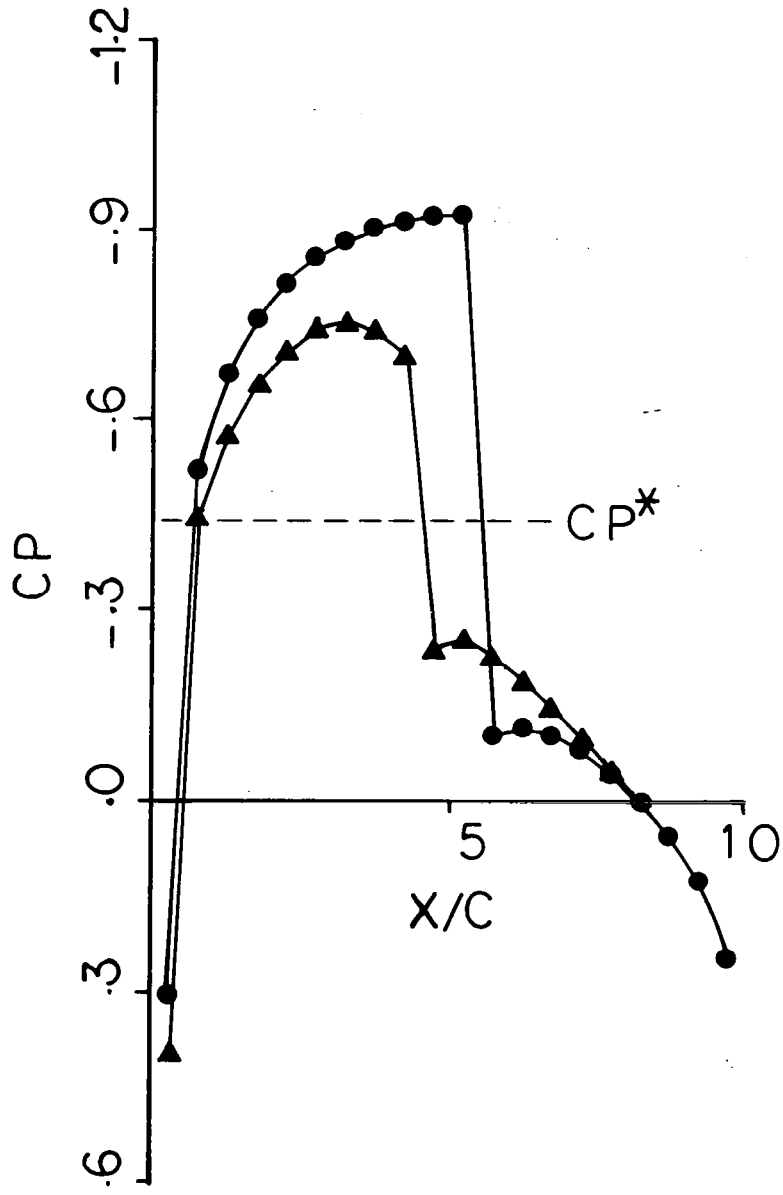

Figure 39. Variation of pressure coefficients over the airfoil for Case IIb (M_{in} = 0.8, $\beta_{in} = 0^{o}$, $M_{upper\ max}$ = 1.16, $M_{lower\ max}$ = 1.26)

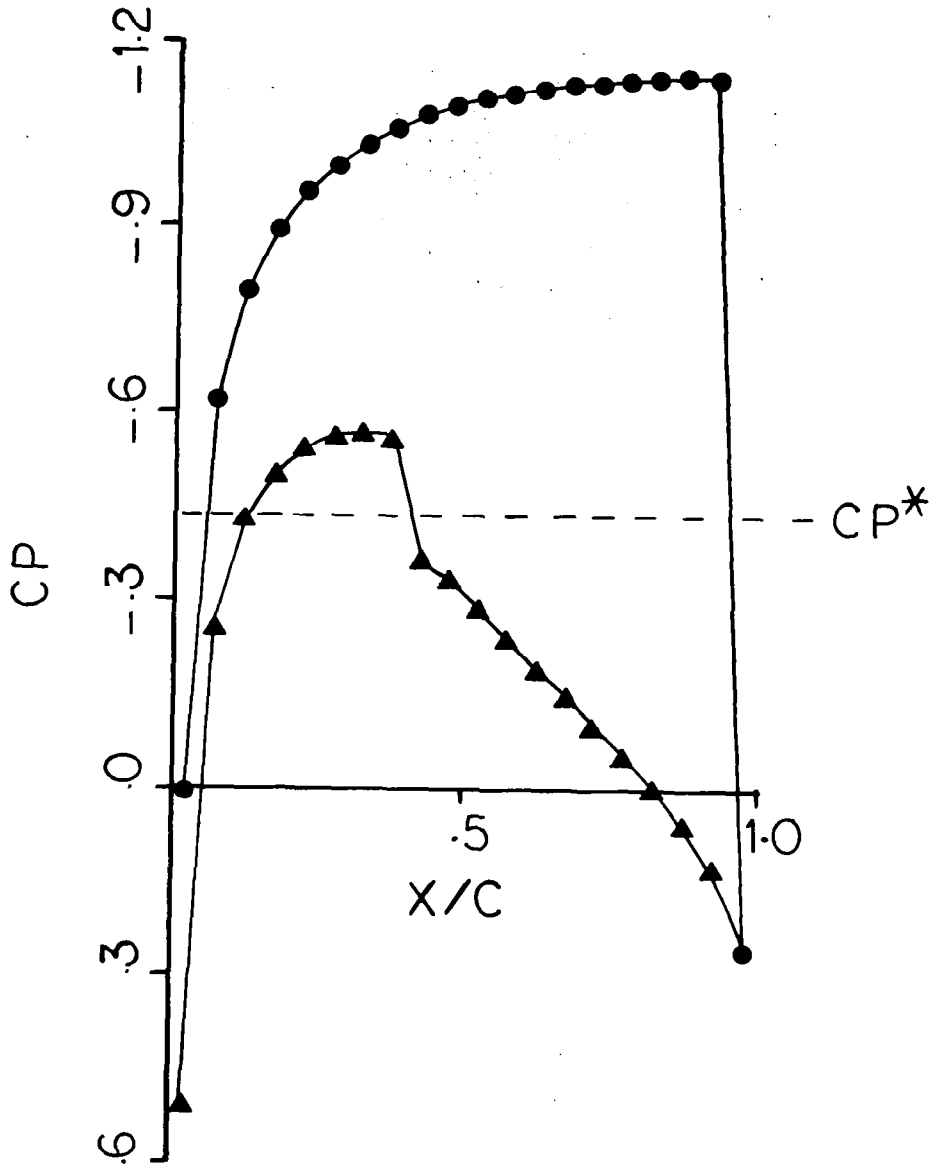

Figure 40. Variation of pressure coefficients over the airfoil for Case IIc ($M_{in} = 0.8$, $\beta_{in} = -1^{o}$, $M_{upper\ max} = 1.07$, $M_{lower\ max} = 1.39$)

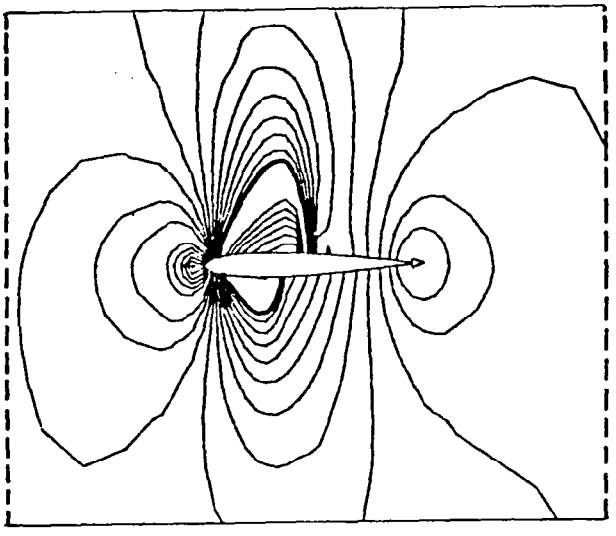

Figure 41. Iso-Mach lines for Case IIa (M_{in} = 0.8, β_{in} = 1^{o})

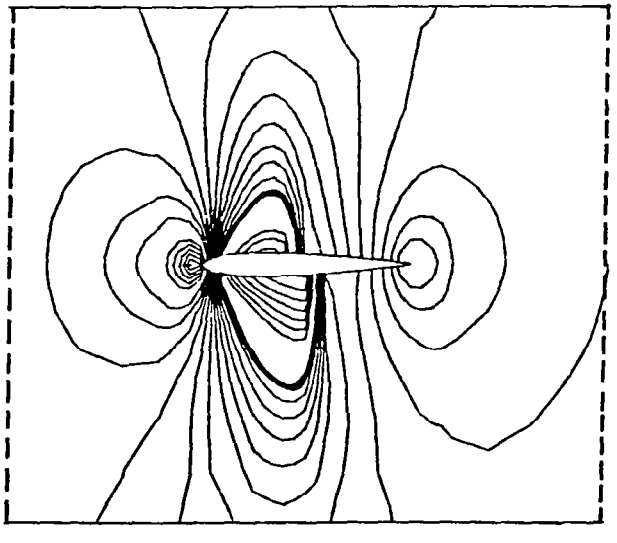

Figure 42. Iso-Mach lines for Case IIb (M_{in} = 0.8, β_{in} = 0^{o})

Figure 43. Iso-Mach lines for Case IIc (M_{in} = 0.8, β_{in} = -1^{o})

capturing solution. This was repeated until the shock moved downstream far enough to satisfy the shock jump conditions; in which case both the shock fitting and the shock capturing yielded the same solution.

Finally, the chordwise pressure distributions obtained for an additional test case are presented for upper and lower surface of the airfoil respectively in figures 44 and 45. Here the inlet flow conditions of Case IIb were used, but instead of determining the exit flow angle from the trailing edge Kutta condition, a value of $\beta_{ex} = 0^{o}$ was specified along the exit stations. Both the grid shown in figure 4 (20 elements over the airfoil) and a fine grid shown in figure 46 (30 elements over the airfoil) were employed for this analysis. The differences in the pressure distributions obtained from these grids are too small to show in figures 44 and 45. Also shown in the same figures, are the results of a finite difference- artificial compressibility scheme employed by Farrell and Adamczyk (ref. 16). The results obtained by both methods are within modeling accuracy.

Test Case III
45^{o} Staggered High Solidity NACA 0012 Cascade

A high solidity cascade of NACA 0012 airfoils with a stagger angle of 45^{o} and h/C = 1, is considered in this case. The computational grid employed in the analysis is given in figure 47.

The flow through this cascade is analyzed for the following inlet Mach numbers and angles of attack:

Case IIIa: $M_{in} = 0.80$, $\beta_{in} = 0^{o}$, $\beta_{ex} = 4.01^{o}$ (Computed)

Case IIIb: $M_{in} = 0.85$, $\beta_{in} = 0^{o}$, $\beta_{ex} = 4.70^{o}$ (Computed)

Case IIIc: $M_{in} = 0.85$, $\beta_{in} = 1^{o}$, $\beta_{ex} = 4.60^{o}$ (Computed)

Case IIId: $M_{in} = 0.87$, $\beta_{in} = 0^{o}$, $\beta_{ex} = 4.87^{o}$ (Computed)

The obtained numerical results for the pressure coefficients and iso-Mach lines are presented in figures 48 and 49 respectively. Mach contours in figure 49 are plotted with increments of $\Delta M = 0.05$ and the sonic lines on these figures are denoted by darkened lines.

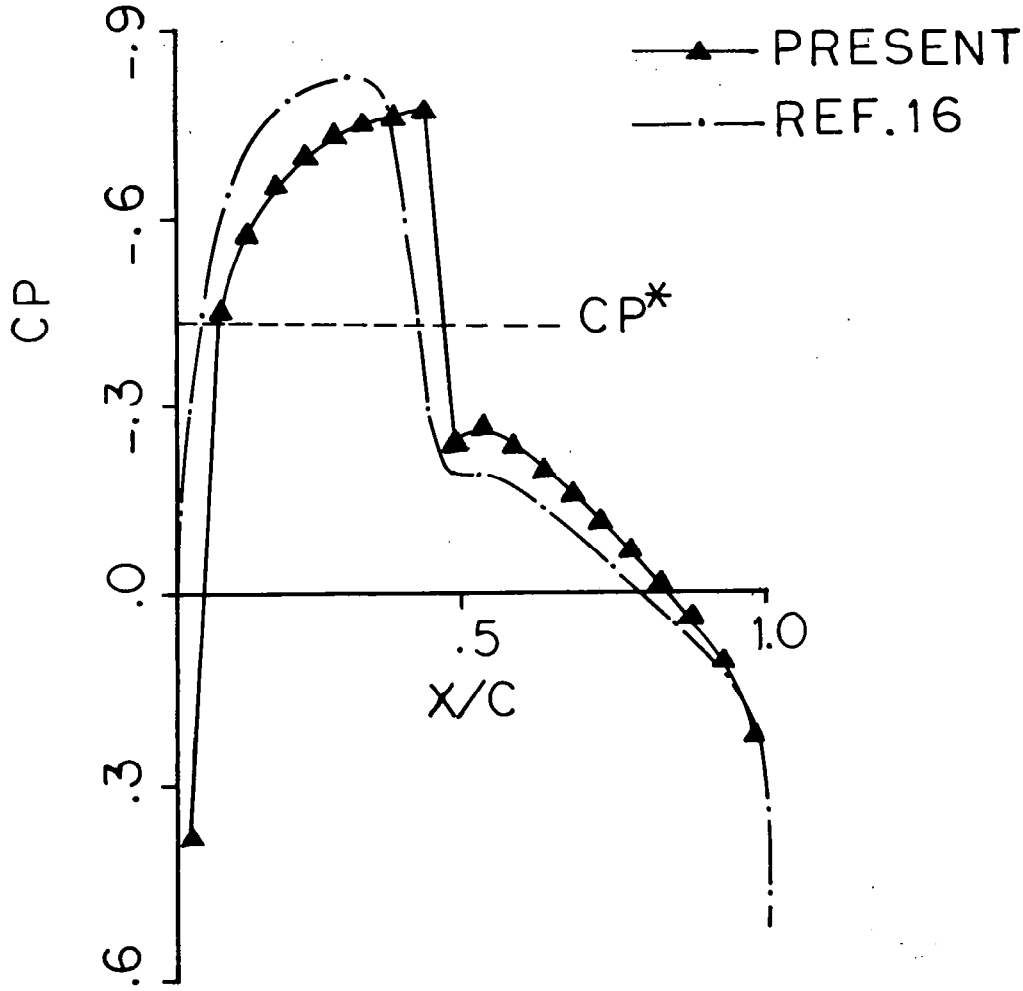

Figure 44. Variation of pressure coefficients over the upper surface of the airfoil for a specified exit angle ($M_{in} = 0.8$, $\beta_{in} = \beta_{ex} = 0^{o}$)

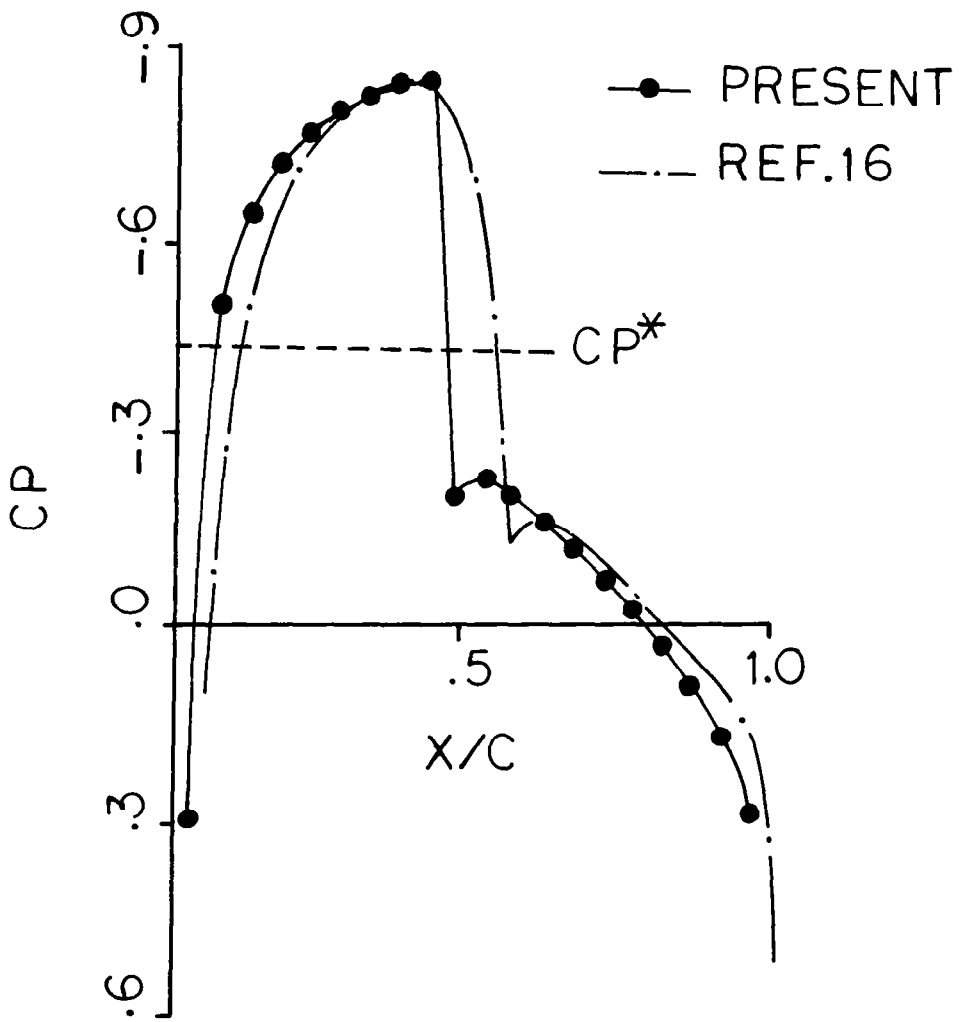

Figure 45. Variation of pressure coefficients over the lower surface on the airfoil for a specified exit angle ($M_{in} = 0.8$, $\beta_{in} = \beta_{ex} = 0^{o}$)

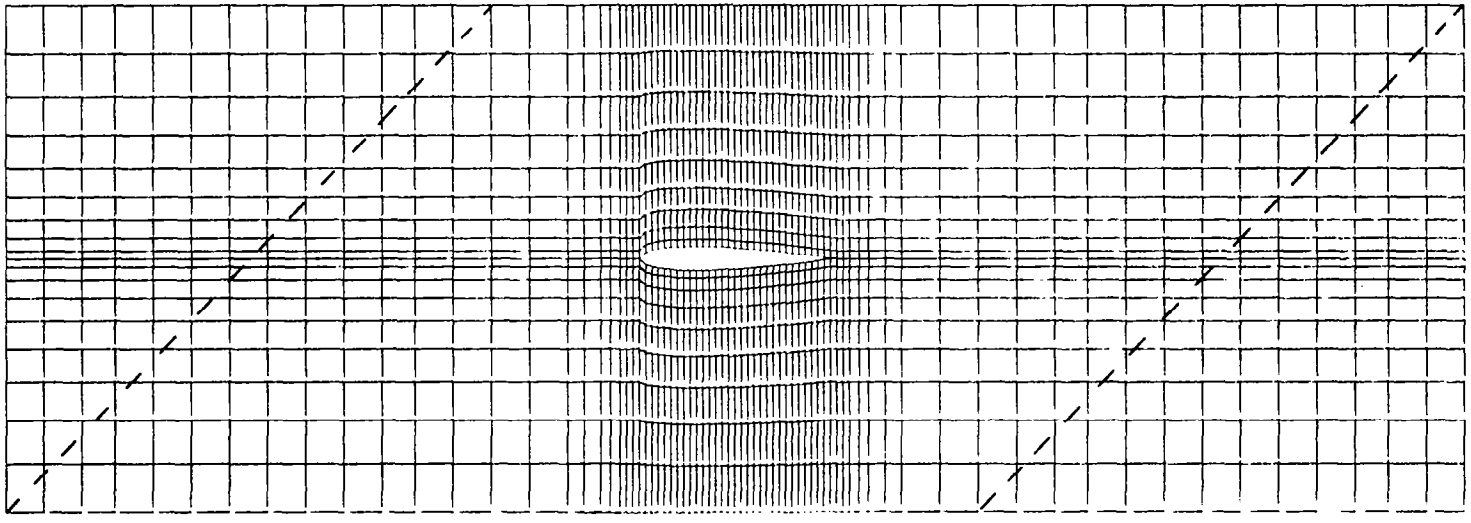

Figure 46. Refined grid employed for Case II with a specified exit angle ($M_{in} = 0.8$, $\beta_{in} = \beta_{ex} = 0^{o}$)

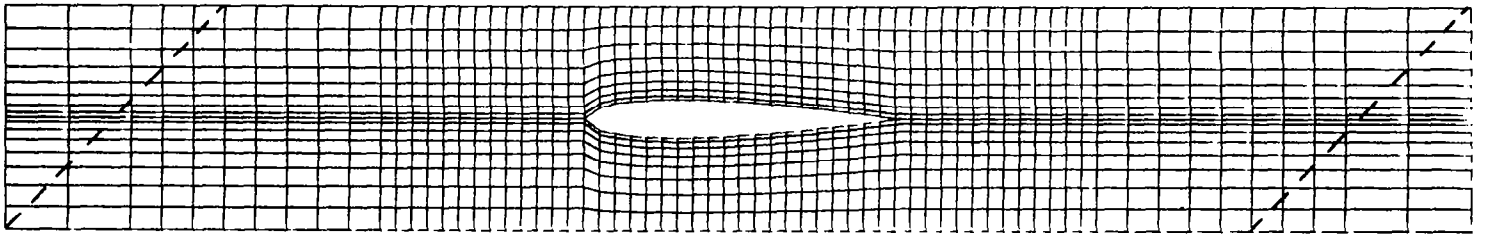

Figure 47. Finite element grid for 45^{o} staggered, high solidity cascade of NACA 0012

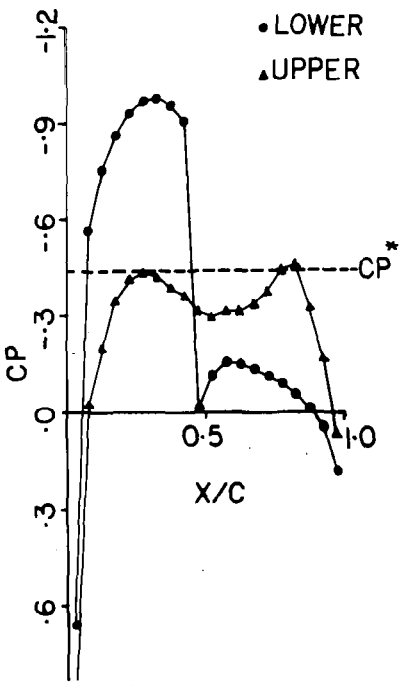

a) Case IIIa (M_{in} = 0.80, β_{in} = 0°)

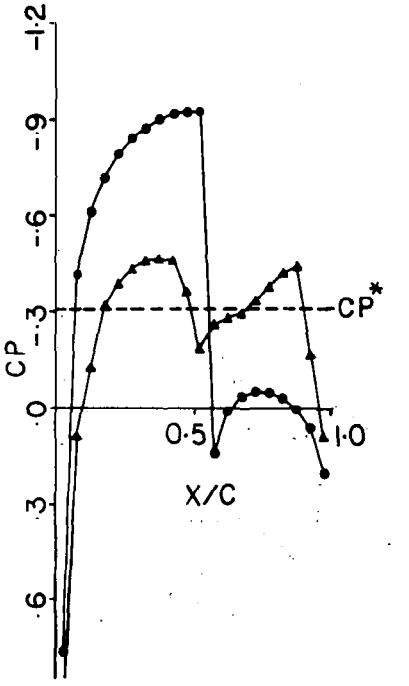

b) Case IIIb (M_{in} = 0.85, β_{in} = 0°)

Figure 48. Pressure coefficients over the airfoil surfaces for Case III

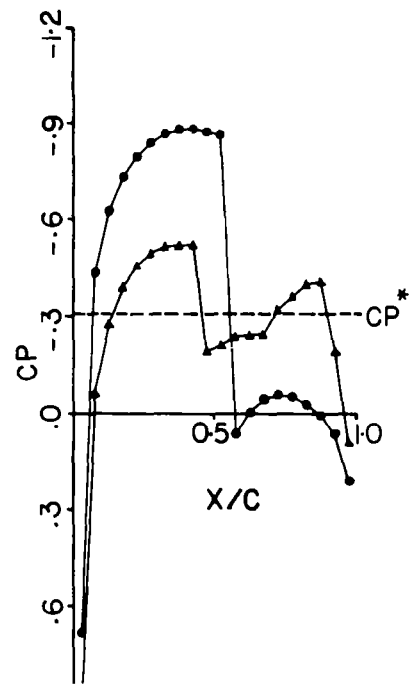

c) Case IIIc (M_{in} = 0.85, β_{in} = 1°)

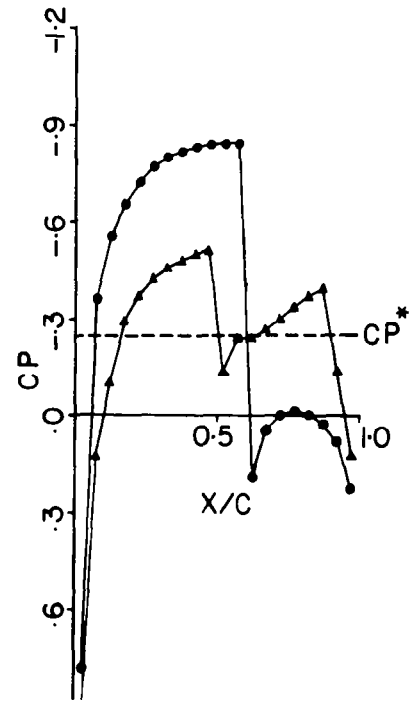

d) Case IIId (M_{in} = 0.87, β_{in} = 0°)

Figure 48. Pressure coefficient over the airfoil surfaces for Case III (Continued)

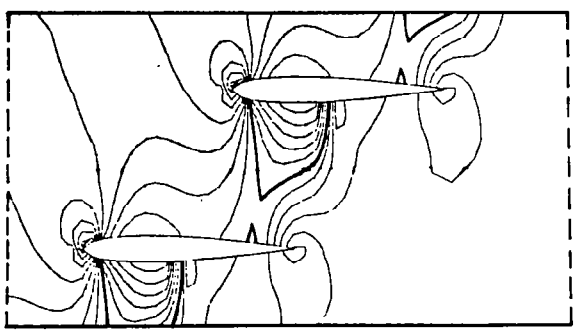

a) Case IIIa (M_{in} = 0.80, β_{in} = 0°)

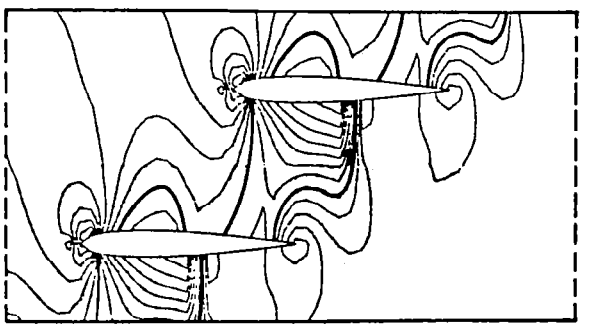

b) Case IIIb (M_{in} = 0.85, β_{in} = 0°)
-Choked flow

Figure 49. Iso-Mach lines for Case III (ΔM = 0.5)

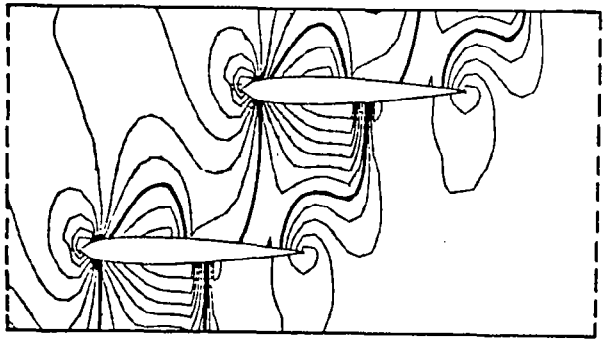

a) Case IIIc (M_{in} = 0.85, β_{in} = 1°)
-Choked flow

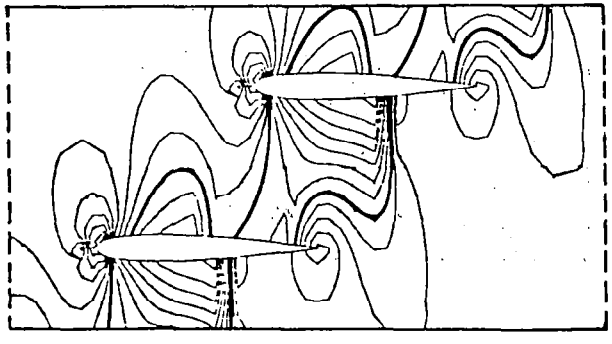

b) Case IIId (M_{in} = 0.87, β_{in} = 0°)
-Choked flow

Figure 49. Iso-Mach lines for Case III (Continued)

For Case IIIa, the solution consists of embedded shocks, one on each surface of the airfoil, the lower shock being much stronger. As the inlet Mach number is increased to 0.85 in Case IIIb, the strength and the size of both shocks grow considerably. Meanwhile, a new supersonic pocket develops on the upper surface. At this point, a subsonic to supersonic sonic line crosses the entire channel and the flow is choked. It is interesting to note the increased turning effect of the Kutta condition at the trailing edge as seen in figure 49b.

When the inlet Mach number is further increased to 0.87, a new set of stable solutions are obtained. As can be observed from figures 49b, 49d, and 50, the position of the sonic line crossing the channel does not change. In fact, the flow field past the sonic line in the channel, remains virtually the same except in the vicinity of the shocks. Since, the outlet mass flow is increased for $M_{ex} = 0.87$, the flow turns to produce an oblique shock to satisfy the exit flow conditions. The change in circulation, in turn, affects the flow configuration around the trailing edge. The sensitivity of flow conditions around the trailing edge will further be discussed.

In the above test cases, no additional difficulties were encountered due to the developed complex shock patterns. The obtained results illustrate the generality of the computational method. Multiple shocks, supersonic pockets with irregular geometries, interaction of the trailing edge conditions with the shocks, and the effect of large stagger angles can all be accounted for. In all cases, the accuracy of the shock capturing solutions were tested by comparing each with the shock fitting results (ref. 15) and found to be satisfactory. Furthermore, it should be noted that the Mach contour patterns obtained for the choked flow cases are in close agreement with those reported by Kozel, et.al. (ref. 27). Their results include both finite difference solutions of small disturbance equations and experimental measurements for a cascade of 8%, symmetric, circular-arc airfoils with $\alpha_s = 45^o$ and $h/C = 1$.

Test Case IV - 8% Circular-Arc Cascade

Using the grid shown in figure 51, the 45^o staggered cascade of 8% circular-arc airfoil of Kozel, et.al. (ref. 27) is also analyzed here for the inlet flow conditions $M_{in} = 0.876$ and $\beta_{in} = 0.5^o$. Shown in figure 52 are the experimental and numerical results reported in reference 27, as well as the finite element results of the same problem. The agreement of the numerically determined iso-Mach lines with that of the experimentally obtained iso-density lines is excellent. The calculated pressure distribution over the airfoil surface is shown in figure 53. The exit flow angle for this case was computed to be 2.88^o.

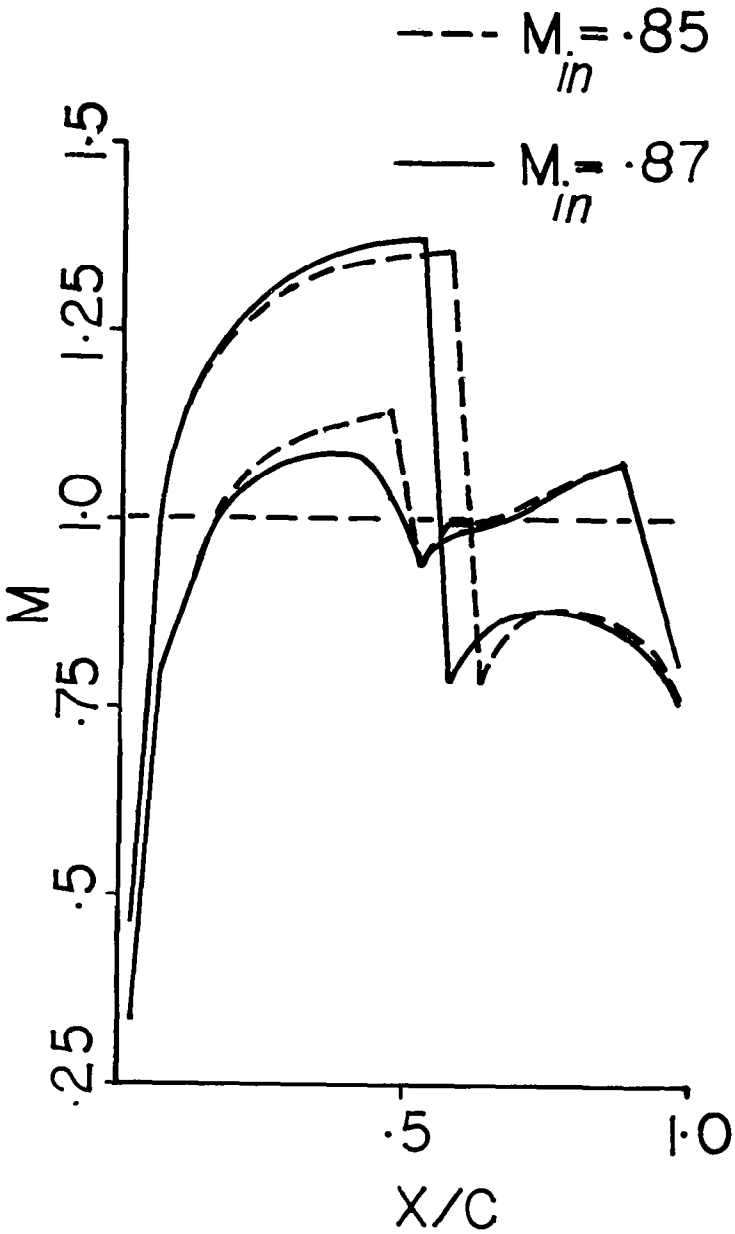

Figure 50. Airfoil surface velocity distributions for choked flows

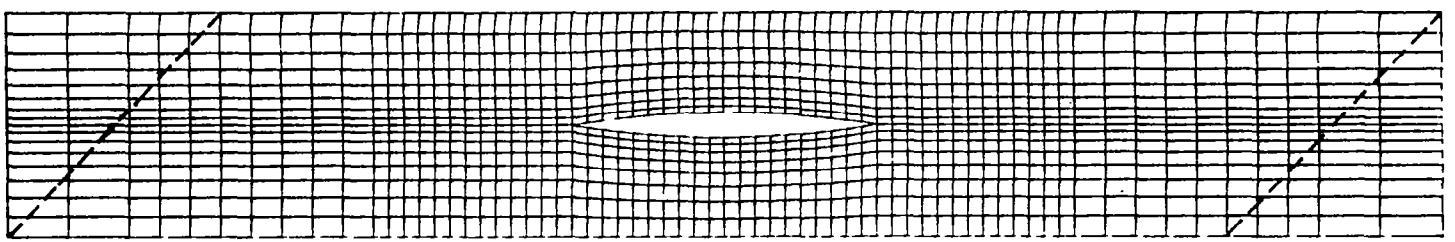

Figure 51. Finite element grid for 45^{o} cascade of 8% circular-arc airfoil

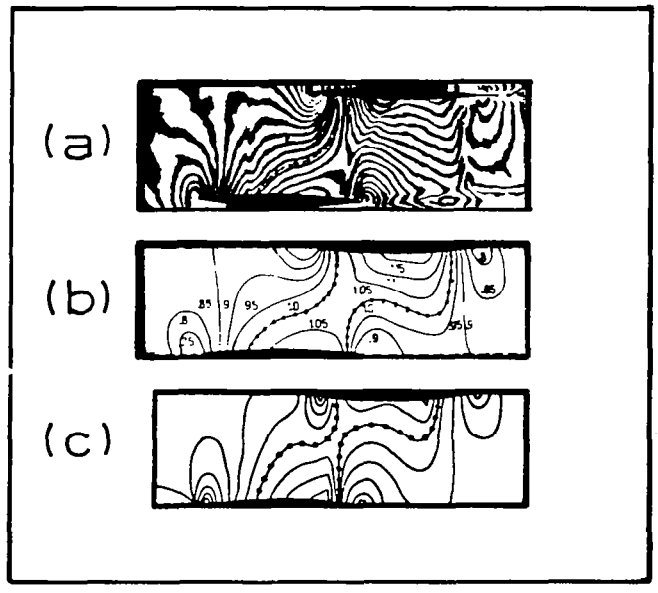

Figure 52. Iso-Mach and iso-density lines for 8% circular-arc airfoil

a) experimental (ref. 27),

b) finite difference solution of small perturbation equation (ref. 27),

c) finite element solution ($\Delta M = 0.5$)

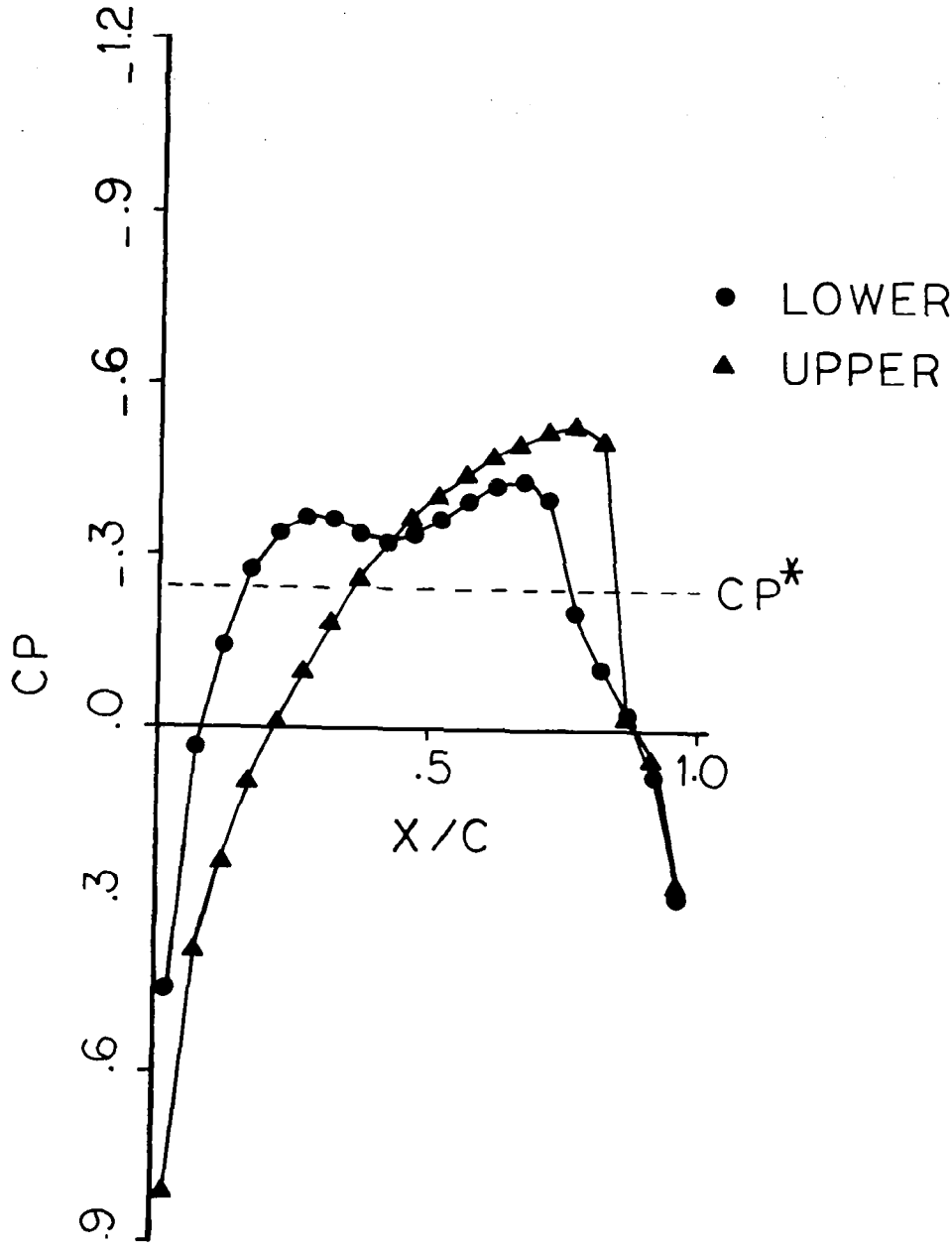

Figure 53. Pressure distribution over the 8% circular-arc airfoil of 45^{o} staggered cascade ($M_{in} = 0.876$, $\beta_{in} = 0.5^{o}$, $\beta_{ex} = 2.88^{o}$)

Test Case V - Supercritical Cascade

Shown in figure 54 is the computational grid used for a cascade of shock-free supercritical blades designed by Sanz (ref. 30) from the hodograph solution. The cascade was analyzed using the following shock-free design conditions:

$$M_{in} = 0.711$$

$$\beta_{in} = 30.81^{o}$$

$$\beta_{ex} = -0.35^{o}$$

$$\alpha_{s} = 9.33^{o}$$

$$h/C = 1.034 \quad .$$

The same cascade was also analyzed by Steger, et.al., (ref. 32) using an implicit finite difference code for full-Euler equations.

Mach number distributions obtained from the three methods are presented in figure 55 for comparison, showing the present solution to be in excellent agreement with the hodograph solution. The Mach number contours of the flow, determined by the present finite element method, are displayed in figure 56 using $\Delta M = 0.05$ increments.

No particular difficulty was encountered in obtaining steady state solutions to this problem. A small "wiggle" appears in the finite element solution of the pressure distribution at the upper surface of the blade which does not exist in the hodograph solution. This is attributed to the sensitivity of the shock-free solution to the accurate definition of the geometry at this point of high curvature. A refinement of the grid at this region seems necessary for better accuracy.

Efficiency of the Developed Computational Procedure

The solution of the transonic flow problem in a cascade by using the developed procedure involves the following basic steps:

- generate a finite element grid,
- start with a high artificial viscosity parameter, iterate until a steady state solution is obtained,
- reduce the artificial viscosity and repeat the procedure,

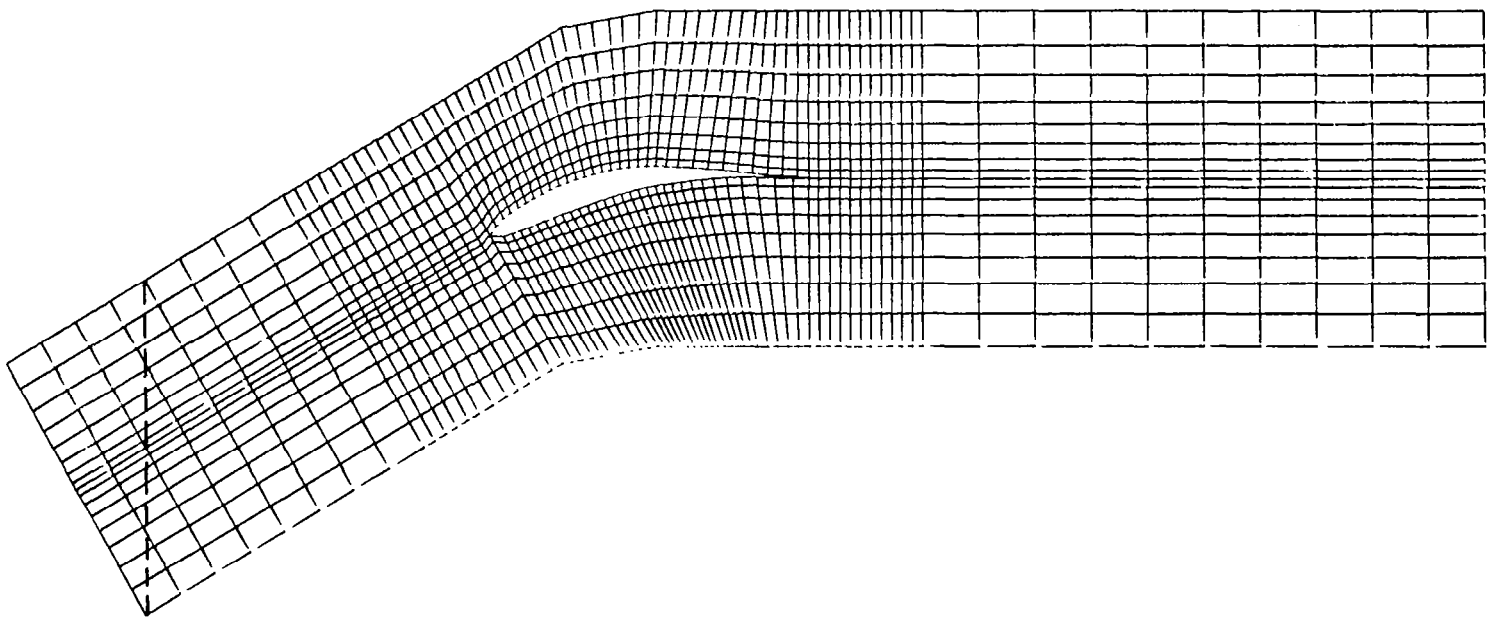

Figure 54. Computational grid used for a cascade of shock-free blade of Sanz

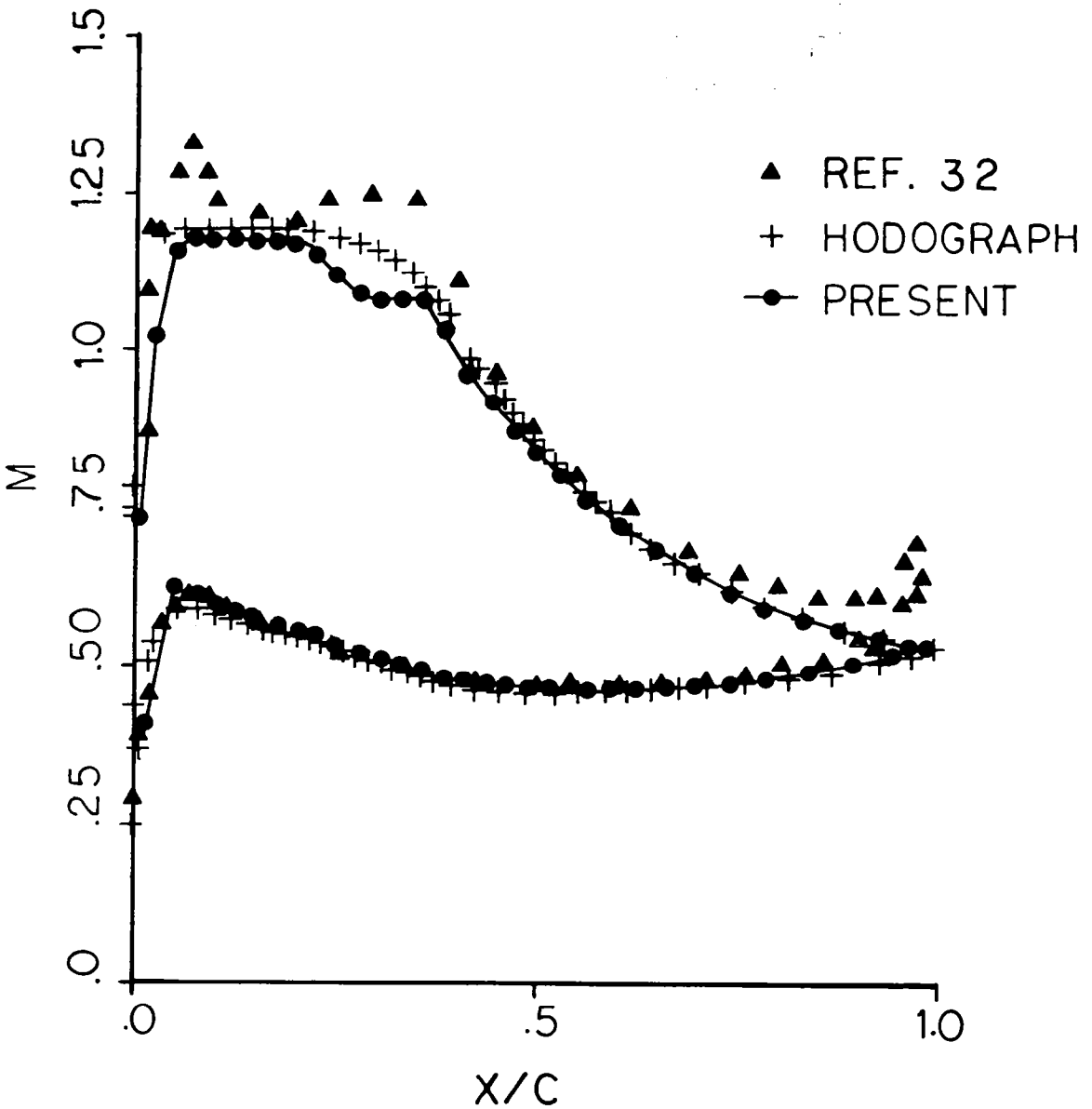

Figure 55. Comparison of velocity distribution over shock-free Sanz blade

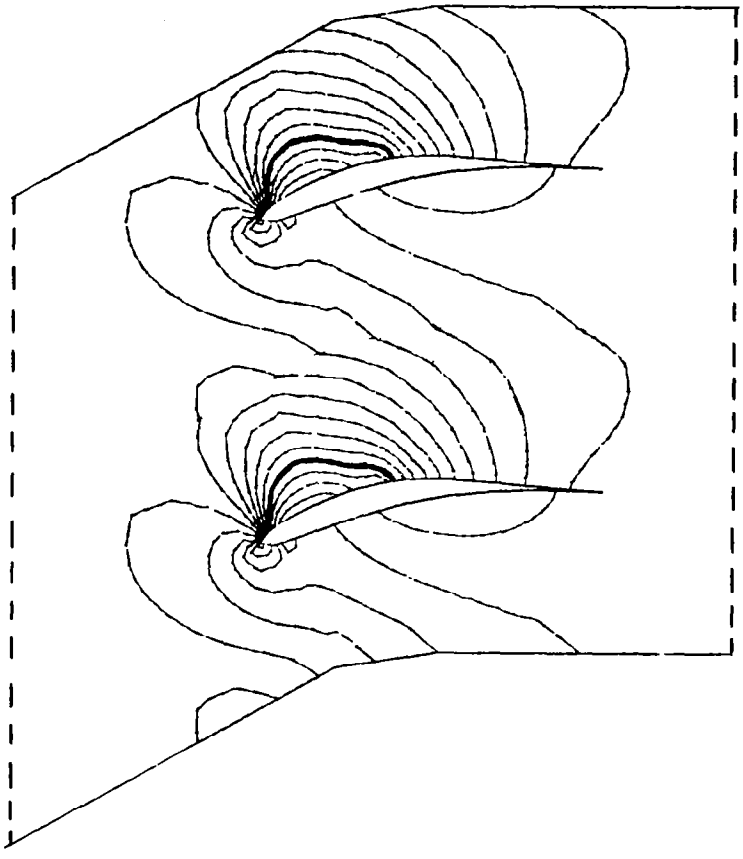

Figure 56. Iso-Mach lines for cascade of shock-free blade of Sanz ($\Delta M = 0.5$)

- perform shock fitting when "wiggles" occur at the shock region,

- repeat the procedure with a more refined grid to check the accuracy of the obtained solution if necessary.

The computational efficiency for each of the above steps are based on performing the following tasks:

- the generation of a finite element grid requires the definition of nodal coordinates for each node and nodal connectivities for each element. In the applications summarized in this report, the grid was prepared by coding a simple special purpose mesh generation program for each case. In practice, this can be achieved interactively by using general purpose finite element mesh generation programs and computer graphics terminals, e.g., (ref. 34),

- iterative solution of the equations by using the constant coefficient scheme described in page 13 requires decomposition of a symetric matrix only once at the beginning of the iterations. This matrix is banded for which a wave-front solver is employed. After the first time step, back-substitution procedure is performed on this system of equations,

- the computer cost is proportional to the number of nodal points and elements on the computational grid, and the number of iterations required for final convergence. These depend on the complexity of the problem and the users knowledge of the problem. For example when one solves a problem for 0^{o} angle of attack for a cascade, the solution of 1^{o} angle of attack case can be obtained by choosing better initial conditions and a more efficient variation of artificial viscosity and relaxation factor during the time steps.

The computer program named TRANS4 which has evolved during this research has been coded and tested for both CDC 6600 and IBM 4341 machines. The central and auxillary memory requirements of the program, in number of words, for CDC 6600 can be determined by using the expressions:

$$CM = \text{Max}\ \{8*NODES,\ 6*NODES + WF*(WF-1)/2 + 10\} + 5*NUMEL + 35{,}500$$

$$MS = 53*(NUMEL + NODES)$$

where

NODES = total number of nodal points,

NUMEL = total number of elements,

WF = maximum wave-front of equations,

CM = central memory requirement,

MS = information to be stored on auxillary memory devices.

In order to give a detailed description of the computer cost, computer requirements of four sample cases are presented in Table 1. The total CPU times are quoted based on the assumption that uniform flow conditions are used as initial solutions in each case and that no additional flow information is available.

Table 1 - Computer time and auxillary memory requirements of TRANS4 computer program on CDC 6600 of Indiana University

Problem	Number of elements	Number of nodes	Length of maximum wave-front	CPU time for first step (seconds)	CPU time for each remaining steps (seconds)	Total number of steps	Total CPU time (minutes)	Total central memory (words)	Total auxillary storage (words)
NACA 0012 Cascade 0^{o} Stagger Low Solidity	320	369	11	1.6	1.2	250	5.0	40,052	36,517
NACA 0012 Cascade 45^{o} Stagger Low Solidity (Refined Grid)	1332	1500	35	10.7	3.7	400	24.8	54,160	150,096
NACA 0012 Cascade 45^{o} Stagger High Solidity	1056	1206	34	7.8	3.0	900	45.1	50,428	119,886
Sanz Cascade of Supercritical Blade	1152	1314	31	7.6	3.2	400	21.4	51,772	130,698

CONCLUSIONS

Application of the finite element method to the solution of transonic flow problem in cascades is presented and the importance of the computational grid for obtaining accurate and efficient solutions is illustrated. The following basic conclusions, which were reached through this study, summarize the importance considerations in the solution of transonic flow problems in cascades:

- The most critical regions in the modeling of transonic flows are the supersonic pocket and the shock. The accuracy and convergence on the solution in this region primarily depend on the artificial viscosity distribution. The artificial viscosity distribution must be chosen in terms of the local Mach number, the local grid size, and the number of elements in the supersonic pocket.

- The shock is a critical region since errors in the supersonic pocket are magnified as they are convected in the direction of the flow till they reach the shock. The solution is most sensitive to the artificial viscosity distribution at this region. A combined usage of shock fitting and shock capturing techniques is very useful for the solution of the problem. Finite element method is very efficient in applying these techniques.

- The leading edge of the airfoil requires a refined grid for better accuracy. However, if the flow is subsonic, the smearing of the solution in this region with a coarse grid remains local and does not generally affect the overall flow configuration, since the equations are elliptic in this region.

- Application of the Kutta condition illustrates the sensitivity of the flow around the trailing edge region and the importance of proper exit conditions. The need for accurate modeling on the trailing edge is apparent in the sample cases in which interaction with the supersonic pocket develops.

- Development of a finite element grid for the problem requires consideration of several different flow structures. If one uniformly refines the grid for accuracy, the efficiency suffers considerably, since the convergence requirements at the supersonic pocket become more stringent with the increasing number of elements. Since the pressure gradients are generally low, one should stay with a reasonable number of elements in this region to obtain accurate yet efficient results. Leading and trailing edges are local regions of high pressure gradients and require local refinements in the grid. The modeling of the

shock requires a grid fitting rather than a grid refinement. This suggests a modification on the grid rather than a refinement.

The obtained numerical results demonstrate that the finite element method can be employed quite effectively for the analysis of rather complex transonic flow problems in cascades. Simple grids that will provide accurate results as well as fast convergence can be generated quite efficiently. The above discussion also describes the basic advantage of a finite element method for the solution of transonic flow problems. In addition to the computational grids which fit the boundaries of the overall flow domain, one should also be able to generate grids which are capably of accurately describing the irregular geometries of different flow regions. The grid generation should be interactive to allow modifications at critical regions, such as around the shock or at the leading and trailing edges. The current finite element mesh generation techniques provide such capabilities resulting with considerable computational efficiencies in the solution of transonic flow problems in cascades, e.g., (ref. 34).

Finally, for the designer of a new cascade, the following analysis procedure can be recommended:

- Start with a coarse grid and calculate a basic solution to the problem.

- Check the accuracy of the solution by refining the grid at critical regions and comparing the results.

Once an efficient grid is defined for a particular set of problems, the designer can approach the problem with more confidence. In terms of practical efficiency in the solution of transonic flow problems, i.e., in terms of the number of man-hours and amount of computer time required to obtain an accurate solution to the problem, the above approach is practical.

REFERENCES

1. Akay, H. U., Ecer, A., and Utku, M., "Finite Element Analysis of Compressible Flow", Proc. Symp. on Appl. Comp. Meth. in Engng., Los Angeles, California, August 1977, pp. 799-809.

2. Akay, H. U., and Ecer, A., "Treatment of Shocks in the Computation of Transonic Flows Using Finite Elements", Proc. 3rd Int. Symp. on Finite Elements in Flow Problems, Banff, Canada, June 1980.

3. Akay, H. U., and Ecer, A., "Finite Element Analysis of Transonic Flows in Highly Staggered Cascades", AIAA, paper 81-0210, 19th Aerospace Sciences Meeting, St. Louis, Missouri, January 1981.

4. Akay, H. U., and Ecer, A., "Transonic Flow Computations in Cascades Using Finite Element Method", ASME 26th International Gas Turbine Conference, Houston, Texas, March 1981 (also to be published in ASME Journal of Engineering for Power, 1981).

5. Brandt, A., "Multi-Level Adaptive Solution to Boundary Value Problems", Math. Comp. Vol. 31, 1977, pp. 333-391.

6. Bristeau, M. O., Glowinski, R., Periaux, J., Perrier, P., Pironneau, O., and Poirier, G., "Application of Optimal Control and Finite Element Methods to the Calculation of Transonic Flows and Incompressible Viscous Flows", IRA Laboria, Report No. 294, April 1978.

7. Chan, S. T. K., and Brashear, M. R., "Finite Element Analysis of Unsteady Transonic Flow", AIAA paper 75-875, 8th Fluid and Plasma Dynamics Conference, Hartford, Connecticut, 1975.

8. Caughey, D. A., and Jameson, A., "Numerical Calculation of Transonic Potential Flow About Wing-Body Combinations", AIAA Journal, Vol. 17, No. 2, February 1979, pp. 175-214.

9. Deconinck, H., and Hirsch, Ch., "Subsonic and Transonic Computation of Cascade Flows", Proc. IV Int. Symp. on Computing Methods in Applied Sciences and Engineering, IRIA, Paris, France, December 1979.

10. Dulikravich, D. S., and Caughey, D. A., "Finite Volume Calculation of Transonic Potential Flow Through Rotors and Fans", Cornell University, Fluid Dynamics and Aerodynamics Program, Report FDA-80-03, Ithaca, New York, March 1980.

11. Dulikravich, D. S., "Private Communications", Lewis Research Center, NASA, 1980.

12. Eberle, A., "Eine Methode Finiter Elemente Zur Berechnung der Transsonischen Potentialstromung um Profile", Messerschmitt-Bolkow-Blohm-UFE, 1352, (0), 1977.

13. Ecer, A., and Akay, H.U., "Application of Finite Element Method for the Solution of Transonic Flow", Proc. 2nd Int. Symp. on Finite Element Methods in Flow Problems, S. Margherita, Italy, June 1976, pp. 191-201.

14. Ecer, A., and Akay, H.U., "On the Finite Element Formulation of Mixed Elliptic-Hyperbolic Problems in Fluid Dynamics", Proc. Int. Conf. on Num. Meth. for Engng., GAMNI, Paris, 1978, pp. 315-322.

15. Ecer, A., and Akay, H.U., "Investigation of Transonic Flow in a Cascade Using an Adaptive Mesh", AIAA, paper 80-1430, 13th Fluid and Plasma Dynamics Conference, Snowmass, Colorado, July 1980 (also to be published in AIAA Journal, 1981).

16. Farrell, C., and Adamczyk, J.J., "Solution of the Transonic Quasi-3D Flow Through a Cascade Using Artificial Compressibility", ASME 26th International Gas Turbine Conference, Houston, Texas, March 1981.

17. Glowinski, R., Periaux, J., and Peronneau, O., "Transonic Flow Simulation by the Finite Element Method via Optimal Control", Proc. 2nd Int. Symp. on Finite Element Methods in Flow Problems, S. Margherita, Italy, June 1976, pp. 249-259.

18. Gostelow, J.P., "Potential Flow Through Cascades - A Comparison Between Exact and Approximate Solutions", A.R.C.C.P. No. 807, 1965.

19. Hafez, M., South, J., and Murman, E., "Artificial Compressibility Methods for Numerical Solutions of Transonic Full Potential Equation", AIAA Journal, Vol. 17, No. 8, August 1979, pp. 838-844.

20. Holst, T.L., and Ballhaus, W.F., "Fast Conservative Schemes for the Full Potential Equation Applied to Transonic Flows", AIAA Journal, Vol. 17, No. 2, February 1979, pp. 145-152.

21. Holst, T.L., "Implicit Algorithm for the Conservative Transonic Full Potential Equation Using an Arbitrary Mesh", AIAA Journal, Vol. 17, No. 10, October 1979, pp. 1038-1045.

22. Irons, B.M., "A Frontal Solution Program for Finite Element Anaylsis", Int. J. Num. Meth. Engng., 2, No. 1, pp. 5-32, 1970.

23. Ives, D.C., and Liutermoza, J.F., "Second-Order-Accurate Calculation of Transonic Flow Over Turbomachinery Cascades", AIAA Journal, Vol. 17, No. 8, August 1979, pp. 870-876.

24. Jameson, A., "Iterative Solution of Transonic Flows Over Airfoils and Wings", Comm. Pure and Appl. Math., Vol. 2, 1974, pp. 283-309.

25. Jameson, A., "Transonic Potential Flow Calculation Using Conservation Form", Proc. AIAA Second Conference on Computational Fluid Dynamics, Hartford, Connecticut, June 1975, pp. 148-161.

26. Jameson, A., "Acceleration of Transonic Potential Flow Calculations on Arbitrary Meshes by the Multiple Grid Method", Proceedings of AIAA Computational Fluid Dynamics Conference, Williamsburg, Virginia, July 1979, pp. 122-146.

27. Kozel, K., Polasek, J., Vavrincova, M., "Numerical Solution of Transonic Flow Through a Cascade with Slender Profiles", Sixth Int. Conf. on Numerical Methods in Fluid Dynamics, Tbilisi, USSR, June 1978.

28. Murman, E.M., and Cole, J.D., "Calculation of Plane Steady Transonic Flow", AIAA Journal, Vol. 9, No. 1, January 1971, pp. 114-121.

29. Murman, E.M., "Analysis of Embedded Shock Waves Calculated by Relaxation Methods", AIAA Journal, Vol. 12, No. 5, May 1973, pp. 626-633.

30. Sanz, J., "Private Communications", Lewis Research Center, NASA, 1980.

31. South, J.C., and Brandt, A., "Application of a Multi-Level Grid Method to Transonic Flow Calculations", Transonic Flow Problems in Turbomachinery (Edited by T.C. Adamson and M.F. Platzer), Hemisphere Publishing, 1977, pp. 180-207.

32. Steger, J.L., Pulliam, T.H., and Chima, R.V., "An Implicit Finite Difference Code for Inviscid and Viscous Cascade Flow", AIAA paper 80-1427, 13th Fluid and Plasma Dynamics Conference, Snowmass, Colorado, July 1980.

33. Strang, G., and Fix, G.J., An Analysis of the Finite Element Method, Prentice-Hall, Englewood Cliffs, 1973.

34. SUPERTAB - "Interactive Finite Element Model Generation System", SDRC - Structural Dynamics Research Corporation, Milford, Ohio, 1980.

35. Zienkiewicz, O.C., The Finite Element Method, 3rd Edition, McGraw-Hill, London, 1977.

1. Report No.	2. Government Accession No.	3. Recipient's Catalog No.
NASA CR-3446		

4. Title and Subtitle	5. Report Date
FINITE ELEMENT ANALYSIS OF TRANSONIC FLOWS IN CASCADES - IMPORTANCE OF COMPUTATIONAL GRIDS IN IMPROVING ACCURACY AND CONVERGENCE	July 1981
	6. Performing Organization Code

7. Author(s)	8. Performing Organization Report No.
Akin Ecer and Hasan U. Akay	None
	10. Work Unit No.

9. Performing Organization Name and Address	11. Contract or Grant No.
Purdue University at Indianapolis 1201 E. 38th Street Indianapolis, Indiana 46205	NSG-3294
	13. Type of Report and Period Covered
12. Sponsoring Agency Name and Address	Contractor Report
National Aeronautics and Space Administration Washington, D.C. 20546	14. Sponsoring Agency Code 505-32-52

15. Supplementary Notes

Final report. Project Manager, Rodrick V. Chima, Fluid Mechanics and Acoustics Division, NASA Lewis Research Center, Cleveland, Ohio 44135.

16. Abstract

The finite element method is applied for the solution of transonic potential flows through a cascade of airfoils. Convergence characteristics of the solution scheme are discussed. Accuracy of the numerical solutions is investigated for various flow regions in the transonic flow configuration. The design of an efficient finite element computational grid is discussed for improving accuracy and convergence.

17. Key Words (Suggested by Author(s))		18. Distribution Statement
Transonic flows	Cascades	Unclassified - unlimited
Finite element method	Potential flows	STAR Category 02
Computational grids		

19. Security Classif. (of this report)	20. Security Classif. (of this page)	21. No. of Pages	22. Price*
Unclassified	Unclassified	108	A06

* For sale by the National Technical Information Service, Springfield, Virginia 22161

NASA-Langley, 1981